PREPARATION AND CHARACTERIZATION OF NANOCOMPOSITES FOR BIOMEDICAL APPLICATIONS

A thesis submitted

by

NISHA SHANKHWAR

to

Indian Institute of Technology Guwahati

in

partial fulfillment of the requirement for the award of the degree of

Doctor of Philosophy in Physics

Department of Physics
Indian Institute of Technology Guwahati
Guwahati – 781039, Assam, India

November 2015

Statement

The work contained in the thesis entitled “Preparation and characterization of nanocomposites for biomedical applications” has been carried out by me under the supervision of Prof. A. Srinivasan at Department of Physics, Indian Institute of Technology Guwahati. This work has not been submitted elsewhere for the award of any degree.

Nisha

November 27, 2015

(Nisha Shankhwar)
Roll No: 10612107
Department of Physics
Indian Institute of Technology Guwahati
Guwahati - 781039
Assam
India

Certificate

This is to certify that the work contained in the thesis entitled “Preparation and characterization of nanocomposites for biomedical applications” submitted by Ms. Nisha Shankhwar in partial fulfillment of the requirement for the award of the degree of Doctor of Philosophy in Department of Physics, Indian Institute of Technology Guwahati, is a record of the candidate’s own work carried out by her under my supervision and guidance. The matter embodied in this report has not been submitted in part or full to any other university or institute for the award of any degree.

November 27, 2015

(Dr. A. Srinivasan)
Professor
Department of Physics
Indian Institute of Technology Guwahati
Guwahati - 781039
Assam
India

TH-1620_10612107

Dedicated

to

my family

TH-1620_10612107

Acknowledgements

In the last few years, I had the privilege of knowing and working with many exceptional and talented people who directly or indirectly contributed to the accomplishment of the work described in this thesis.

My first acknowledgment is made to my supervisor Prof. Ananthakrishnan Srinivasan, who gave me the privilege of being a part of his group some years ago. His accomplishments, professionalism and leadership are a motivation and make me feel privileged for working under his supervision. I equally acknowledge Rajalakshmi Ma′am for making my stay here homely.

I am thankful to my doctoral committee (DC) members, Prof. A. Perumal (Chairman, DC), Prof. P.K. Giri (Department member, DC) and Prof. B.G. Jaganathan (External department member, DC), for their knowledgeable and careful supervision and important suggestions on my work from time to time that resulted in the improvement of my work.

I express my sincere gratitude to former and present heads, Department of Physics for providing necessary facilities. I extend many thanks to all the faculty and staff members of the institute for their professional support. A special thanks to Dr. Sidananda for technical help during the first learning stages and his family for constant encouragement. I really enjoyed all our scientific discussions.

High end instrument support received from Central Instruments Facility, IITG and financial support through a PhD grant by Ministry of Human Resource is gratefully acknowledged. I am grateful to Department of Atomic Energy (2010/34/54/BRNS), Government of India, for financially supporting this work.

During the development of this thesis, I had the fortune to make friends who supported me with their intelligence, professionalism and personal experiences. To Asha, Indrajeet, Mukesh, Himanshu bhaiya, Gyan, Rajkumar, Sunil, Buddhadeb, Arun, Ayushmaan, Urmimala, Gautam, Ankam Lakshman, Prahlad, I express my deep gratitude. I acknowledge Bhargab specially, for helping me with his expertise in computer skills.

The present thesis could not have been completed without assistance and support of many collaborators inside and outside the campus. Very special thanks to distinguished Prof. G. P. Kothiyal for providing me a new exposure to write a book chapter which gave me a wonderful experience. I am indebted to my collaborators and co-authors, Prof. P. S. Robi, Dr. Rajendra K. Singh, Dr. B.B. Mandal and his lab group, Dr. Kuldeep Sharma, Dr. Pawan Kumar, Manishekhar and Kibrom, for their keen interest, insightful discussions and support.

I wish to give my sincere thanks to my friend Mr. Sachitananad Malewar (Director, NEX Robotics) who despite being distant has always been a good supporter and great motivator.

Additionally, I would like to use this opportunity to thank Dr. Maya Ray for her great motivation and support throughout. I cannot forget and express particular gratitude to Pawan Kishor, (SSE, NRF railway), who despite being indulged in his work, took his valuable time for me and given constant support and encouragement. I am a lucky person to have you around.

I have been blessed with a very loving and supportive family. My grandfather, Late Mr. Badalu Prasad, for His Grace, benevolence and for giving me the determination to overcome many trying moments to pursue my dreams. He has always stressed the importance of education. I am eternally indebted to my grandmother, my father Mr. Virendra Prasad; cutest most mother Mrs. Sushma, my loving sister Mrs. Reena and her husband Mr. Bhanu for their unconditional love and care. Special mention to my brother Mr. Raghvendra, who always provided a valuable assistance for solving problems with my laptop and technology related matters. I am grateful to my younger brother Mr. Ajay, who always made my day by playing soulful music on guitar. Beyond this, my most enthusiastic cheerleader Ishanavi, my toddler niece, contributed sunny optimism with her bright little smile to this dissertation. I need to thank my little angel for being such a bundle of joy and laughter. My heartfelt appreciation goes Dr. Onkar Verma (Asst. Prof., NIT Raipur) for his love, support and encouragement throughout my research period. He has shared this entire amazing journey with me and seen me through the ups and downs of the entire process. From him, I learned to work hard, to stand up for myself, and to be self-depend. I am grateful to him for being wonderful role model to me. My family represents the good port that I can reach in the good and bad moments. I could have never reached this stage without their unconditional support.

My final words of acknowledgment go out to my dearest Papa for his love, patience, dedication and for letting me be part of his life. He is the light and inspiration that makes my life better. To Him, I dedicate this thesis.

Nisha Shankhwar

TH-1620_10612107

PREFACE

Advances in physics, materials science, biology and biomedical materials now make it possible to grow living constructs outside the body and to use them as engineered tissues for the repair or replacement of diseased or damaged tissues. One of the objectives of this thesis work is to extend the approach to develop nanostructured and porous materials for some new potential biomedical applications such as hyperthermia therapy of cancer, bone replacement, controlled drug release and interactive wound dressings. This thesis focuses on the development of non-magnetic and magnetic bioactive glasses, magnetic bioactive glass ceramics, nanofibrous polymer-blends and nanofibrous polymer-bioactive glass composites for specific biomedical applications mentioned above.

Surprisingly, after 40 years of research on bioactive glasses by numerous research groups, no other bioactive glass composition has been found to have better biological properties than the original Bioglass 45S5® composition. Though sol-gel derived glasses shows better properties compared to their melt quenched counterpart, obtaining completely amorphous 4SS5 glass composition by sol-gel route is still elusive. Also, it is indeed very rare to find reports of oxide glasses containing small amounts of iron oxide which exhibit strong magnetic behaviour and there are no reports in the literature of fully amorphous bioglass compositions containing iron oxide exhibiting significant magnetic behaviour. Magnetic bioglass-ceramics which are bioactive as well as magnetic, serve a variety of biomedical applications such as thermos-seeds for hyperthermia, contrast agent in magnetic resonance imaging, targeted drug delivery etc. A thorough understanding of the crystallization behaviour and the associated magnetic and bio-response are required to develop efficient thermos-seeds. Considering the large number of surgeries and injury treatment being performed every day, the demand for low-cost interactive wound dressings is ever increasing. Scaffolds for bone regeneration are another synthetic biocomposite which is highly in demand. This thesis addresses the above demands by attempting to develop biomaterials which hold promise for these applications.

The thesis work is presented in six chapters. **Chapter 1** provides a brief introduction to topics of relevance to the content of the thesis. A review of the literature related to the materials of interest to the thesis work is also included in this chapter. **Chapter 2** is dedicated to experimental techniques used in the investigations, including sample preparation and methodologies adopted. The principle and theory behind the experiments performed, the experimental set-up used and the measurement methodology followed are also discussed here.

Chapter 3 is devoted to studies on bulk bioactive glasses with compositions of $41CaO.44SiO_2.4P_2O_5.8Fe_2O_3.3Na_2O$ and $15(ZnO,Fe_2O_3).50SiO_2.20(CaO,P_2O_5).15Na_2O$ (mole %) heat treated at different temperatures and times. This chapter is divided into two sections. The first section contains investigation of $41CaO.44SiO_2.4P_2O_5.8Fe_2O_3.3Na_2O$ glass ceramics and other section describes the studies on $15(ZnO,Fe_2O_3).50SiO_2.20(CaO,P_2O_5).15Na_2O$ glass ceramics. Their potential application in magnetic hyperthermia, general lack of systematic study and the rich scope for unraveling the physics of these materials motivated the work presented in this chapter. A systematic study of crystallographic, magnetic and *in vitro* bioactivity of heat treated glasses provide an insight on the nature and application potential of these materials.

Chapter 4 describes the possibility of obtaining sol-gel derived bioactive glass and glass-ceramics. The reason for this study is to explore an alternate methodology to prepare bioglass with superior bioactivity. This chapter has two sections. The first section is devoted to optimization and control of sol-gel reactions by varying the phosphate precursor in optimized pH conditions to obtain a completely amorphous 45S5 bioglass gel powder and characterizing its properties. The second section provides details of the synthesis of magnetic bioglass and glass ceramic gel powders.

Chapter 5 describes the preparation and characterization of nanofibrous polymer blends and polymer-bioactive glass composites for wound care and bone tissue scaffolding and wound care application. This chapter is sectioned into two. In first section, electrospinning of nanofibrous membranes of water soluble polyvinyl alcohol (PVA) and polyvinyl pyrrolidone (PVP) blends are discussed. These membranes are then tested for interactive wound dressing applications. In second section, an attempt has been made to prepare polymer-bioglass composite scaffolds by combining sol-gel and electrospinning processes. The findings indicate the potential and viability of nanofibrous membranes of both PVA-magnetic bioglass ($43SiO_2.24.5Na_2O.24.5CaO.6P_2O_5.2Fe_2O_3$) (wt %) and PVA-bioglass ($45SiO_2.24.5Na_2O.24.5CaO.6P_2O_5$) (wt %) for use as osteoconductive scaffolds for bone regeneration.

Chapter 6 provides a summary of the results obtained in the thesis and a brief mention of scope for further work in these topics. The references cited in the thesis are listed in the end of the thesis.

Contents

1. Introduction

2. Experimental Techniques

3. Investigations on bulk magnetic bioglass-ceramics

4. Investigations on nanoporous bioglass/glass-ceramics and magnetic bioglass/glass-ceramics

5. Investigations on electrospun fibrous membranes

Chapter 1

Introduction

Progress of the human race has always depended on the ability of man to adopt and develop materials for various purposes. Though the initial demand was for materials that can be used as weapons, cooking and storage utensils, clothing and shelter, health care materials required to cure diseases, heal injuries, and replace or repair broken body parts have always received due attention. History tells us that Romans, Chinese and Aztecs used gold in dentistry more than 2000 years ago. Similarly, use of glass eye and wooden teeth is also recorded in the history of mankind. However, the use of biomaterials did not become practical until the advent of an aseptic surgical technique developed by J. Lister in the 1860s. Thus, the history of what we now call as a biomaterial, which can be defined as *a synthetic material used to replace part of a living system or to function in intimate contact with living tissue*, is relatively short. In 1986, the consensus conference of the European society for biomaterials defined a biomaterial as *a nonviable material used in a medical device, intended to interact with biological system* [WILLI86a]. Biomaterials comprise an exciting field that has been significantly and steadily developed over the last sixty years and encompasses aspects of medicine, biology, chemistry and materials science. Biomaterials are used for a wide variety of applications such as joint replacements, bone plates, bone cement, artificial ligaments and tendons, dental implants for tooth fixation, blood vessel prostheses, heart valves, artificial tissue, contact lenses, and breast implants [NAIR06a]. Many of these applications are related to human bone as depicted in Fig. 1.1.

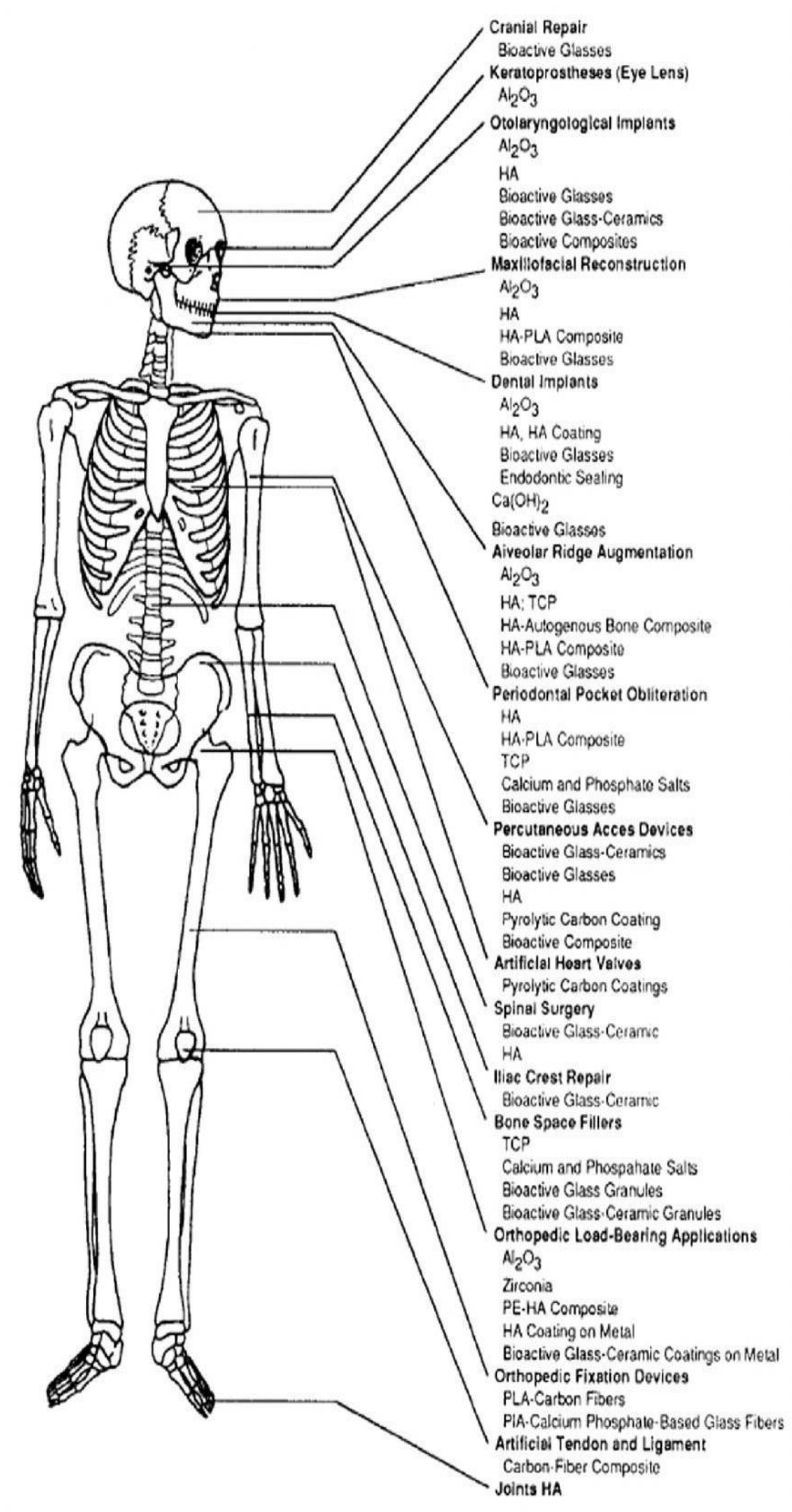

Fig. 1.1: Clinical uses of biomaterials [MART06a].

Bone is a unique tissue which can heal itself without scarring by a process called regeneration. Bone injuries and defects can arise from a variety of causes including fracture nonunion [BUCH02a, EINH99a], dental and orthopedic implant fixation, trauma or tumor resection [DAVI07a], and musculoskeletal disorders such as rheumatoid arthritis [WOOL03a]. Bone is a natural composite material, which by weight contains about 60 % mineral, 30 % matrix and 10 % water. Bone is also a living tissue with cellular content contributing to nearly 15 % of its weight [CLAR08a]. The bone matrix is mainly composed of the highly aligned Type I collagen which gives it a very anisotropic structure (*cf.* Fig. 1.2). This organic component of bone is predominantly responsible for its tensile strength [KUHN98a]. The mineral component of bone is a form of calcium phosphate known as hydroxyapatite (HA). Stoichiometric HA has the chemical formula of $Ca_{10}(PO_4)(OH)_2$. This compound crystallizes in a hexagonal geometry with unit cell dimensions of 9.42 Å along *a* and *b* axes and 6.88 Å along *c*-axis. However, bone mineral is rarely stoichiometric and usually contains many substituents such as magnesium, sodium, potassium, fluorine, chlorine and carbonate ions [CLAR08a].

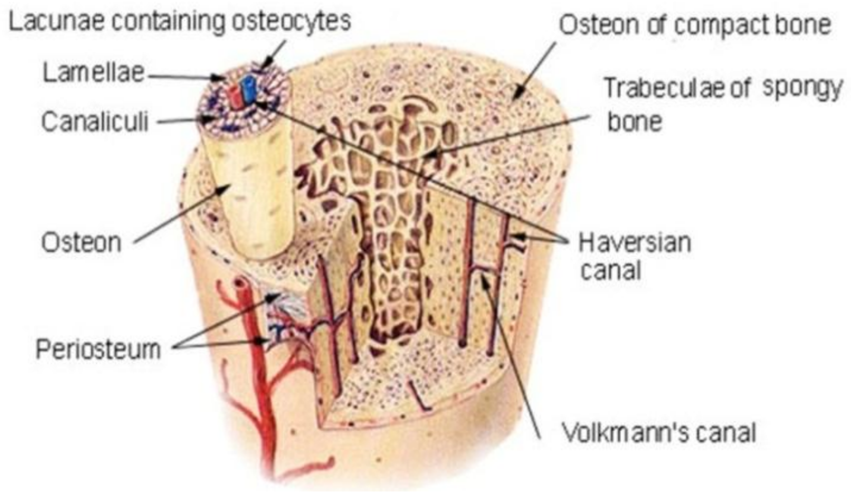

Fig.1.2: Microscopic organization of human bone (adapted from [WEB_SEER]).

1.1 Classification of Biomaterials

Metals, polymers, and ceramics constitute the most common classes of materials used in biomedical applications. These materials are used singly or in combination as composites to form most of the implantation devices available today. These biomaterials can be further divided into four distinct groups according to their biocompatibility or physiological response. The different implant-tissue responses listed in Table 1.1 [HENC82a, HENC98a] also define the four types of biomaterials, *viz.*, inert, porous, bioactive and resorbable. Though metals are extensively used in orthopedic applications for many years, they get corroded after long term interaction with physiological environment. It is critical that an implant material does not evoke a toxic response that can kill cells in the surrounding tissues. In this regard, bioactive materials such as bioactive glass and bioactive glass-ceramics are attractive since they are not toxic and offer good resistance to corrosion. In 1969, L.L. Hench *et al.* [HENC72a] developed the first bioactive material known as bioactive glass or simply bioglass.

Table 1.1: Types of tissue attachment of biomaterials

Type of implant	Type of attachment	Example
Nearly inert	Mechanical interlock (morphological fixation)	Metals, alumina, zirconia, and polyethylene
Porous	In-growth of tissues into pores (biological fixation)	HA and HA coated porous metals
Bioactive	Interfacial bonding with tissues (bioactive fixation)	Bioactive glasses, bioactive glass-ceramics and HA
Resorbable	Replacement with tissues (bioabsorbable fixation)	Tricalcium phosphate and polylactic acid

A bioactive material is one that elicits a specific biological response at the interface of the material which results in the formation of a bond between the tissues and the material. Porous materials provide biological fixation by allowing in-growth of tissue in the pores. Thus, a bioactive material with a porous structure would be a good candidate for bone regeneration. Resorbable biomaterial gets converted into the tissue after interacting with it. Bioactive glass, bioactive glass-ceramics and polymeric composites are the biomaterials of interest to this thesis work.

1.2 Glass, bioglass and bioglass-ceramics

1.2.1 Glass and glass-ceramics

Glass is an amorphous (or vitreous) material, which is commonly referred to as a super-cooled liquid. In 1945, the American Society for Testing and Materials defined glass as an inorganic product of fusion, which has cooled to a rigid condition without crystallizing. If one takes into account that glasses are not restricted to inorganic materials, a more general definition would be '*an amorphous solid completely lacking in long range, periodic atomic structure and exhibiting a region of glass transformation behaviour*' [SHEL97a]. When a molten liquid is slowly cooled below its melting point, it undergoes a discontinuous volume change and solidifies into its crystalline (solid) state by liberating heat, as depicted by the red line in Fig. 1.3(a).

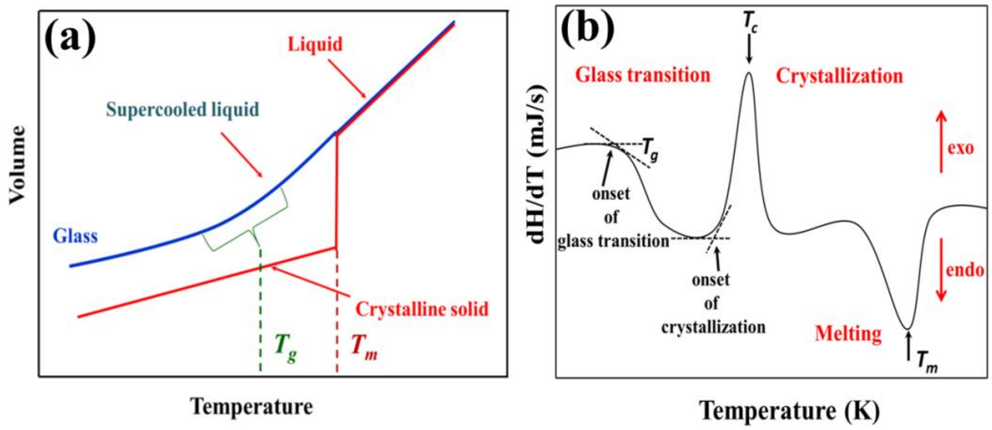

Fig. 1.3: (a) Volume change exhibited by a crystal (red line) and glass (blue line) forming molten liquid during cooling. (b) Typical DSC curve of a glass exhibiting its characteristic behaviour under a constant heating rate.

However, when a glass forming melt is cooled below its melting point (blue line in Fig. 1. 3 (a)), no discontinuous volume change is observed and there is no exothermic effect associated with the change of the liquid to solid state. Instead, the viscosity of the melt increases gradually as the temperature is decreased until it attains a value typical (~10^{13} Poise) of a solid. Fig. 1.3(b) shows a typical plot of heat flow (dH/dt) as a function of temperature when a glass is heated at a constant heating rate. The heat flow exhibits an endothermic base line shift at the glass transition temperature (T_g), followed by an exothermic crystallization peak at T_c. Further heating results in the melting of the crystal at T_m, which is an endothermic transformation. Multicomponent glasses show one or more exothermic peaks corresponding to devitrification of various crystalline phases. Such glasses may sometimes show multiple melting endotherms as well. So, when a glass is heated beyond its glass transition temperature, it forms glass-ceramics. Depending upon the heat treatment conditions, different types and percentages of crystalline phases can be dispersed in the glass matrix. Glass-ceramics have better mechanical strength due to the reinforcement provided to the brittle glassy matrix by the crystalline precipitates [SHEL97a].

1.2.2 Bioglass and bioglass-ceramics

In 1969, Prof. L.L. Hench from University of Florida invented bioglass (BG) with the composition, $45SiO_2.24.5Na_2O.24.5CaO.6P_2O_5$ (where the numerals denote wt.%) which is popularly known as the '45S5 bioglass®' [HENC82a, HENC82b]. Since then, enormous progress has been made in formulating new bioactive glasses and refining existing bioactive glass compositions / microstructure for obtaining better performance in biomedical applications. A review by Prof. Hench summarizes the story of bioglass and its technological adaptation [HENC06a]. A feature common to these bioactive materials is that they bond to bone with no fibrous tissue at the interface. The mechanism of *in vitro* bioactivity of bioactive ceramics is briefly discussed below.

1.2.3 Mechanism of bioactive bonding

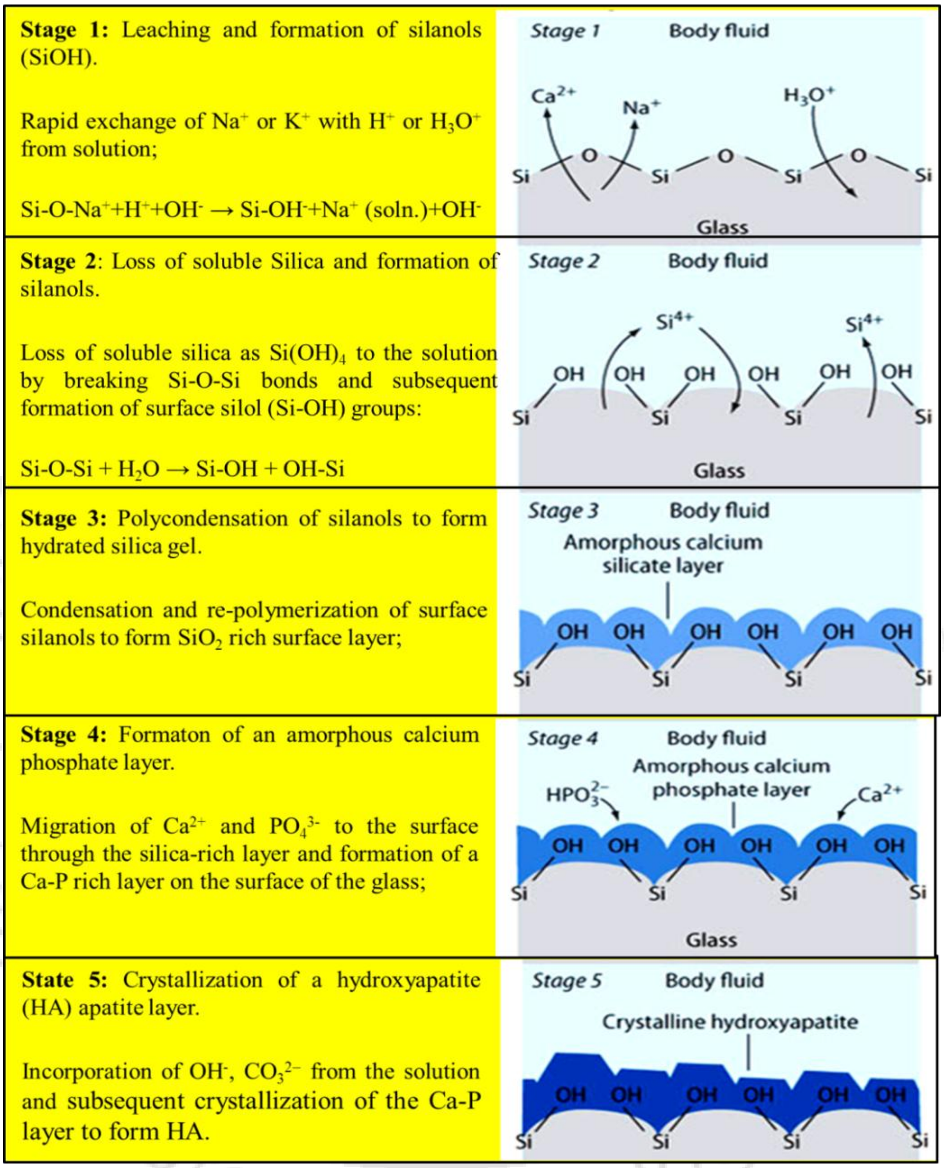

Stage 1: Leaching and formation of silanols (SiOH).

Rapid exchange of Na^+ or K^+ with H^+ or H_3O^+ from solution;

$Si\text{-}O\text{-}Na^+ + H^+ + OH^- \rightarrow Si\text{-}OH^+ + Na^+ (soln.) + OH^-$

Stage 2: Loss of soluble Silica and formation of silanols.

Loss of soluble silica as $Si(OH)_4$ to the solution by breaking Si-O-Si bonds and subsequent formation of surface silol (Si-OH) groups:

$Si\text{-}O\text{-}Si + H_2O \rightarrow Si\text{-}OH + OH\text{-}Si$

Stage 3: Polycondensation of silanols to form hydrated silica gel.

Condensation and re-polymerization of surface silanols to form SiO_2 rich surface layer;

Stage 4: Formaton of an amorphous calcium phosphate layer.

Migration of Ca^{2+} and PO_4^{3-} to the surface through the silica-rich layer and formation of a Ca-P rich layer on the surface of the glass;

State 5: Crystallization of a hydroxyapatite (HA) apatite layer.

Incorporation of OH^-, CO_3^{2-} from the solution and subsequent crystallization of the Ca-P layer to form HA.

Fig. 1.4: The five stage bioactive fixation mechanism of a bioglass.

When a bioactive material is implanted in the body, a series of biophysical and biochemical reactions occur at the implant-tissue interface. These reactions eventually result in a mechanically strong chemical bonding at the interface [HENC82b, HENC82a]. Such attachment is referred to as ‘bioactive fixation’. Hench *et al.* [HENC82b] found that certain compositions of silicate glasses can form such bioactive fixation with bone tissue. The bone bonding property of bioactive glasses can be attributed to the chemical reactivity of the glass in body fluid which results in the formation of a hydroxycarbonate apatite (HCA) layer to which bone can bond. This bonding occurs because of a sequence of chemical reactions induced by ion exchanges between the body fluid and the bioactive glass. The reactions leading to bioactive fixation of bioactive glass occurs in five stages as explained in Fig. 1.4.

1.2.4 Methods of synthesis

Glasses are traditionally formed by rapidly cooling (or quenching) the molten liquid through its melting point or liquidus temperature. The melt-quenching method is designed to take the glass forming liquid through the blue line path in the V-T plot shown in Fig. 1.3(a). Usually, constituent compounds in the form of oxides or carbonates are taken in a platinum crucible and calcined between 600 °C to 800 °C in an electric furnace. After proper calcination, the charge is melted at temperatures ranging between 1400 °C to 1600 °C. The homogenized molten liquid is then quenched by pouring between two copper plates at room temperature to form glass. The brittle nature of bioglasses has posed serious limitations on their use in load bearing applications [HENC05a, HENC98b, HENC91a, OSCA12a, KOKU91a]. To overcome this hurdle, bioactive glass-ceramics (BGC) have been derived from appropriate BG compositions by controlled heat treatment. Controlled heat treatment of glass is based on the knowledge of the crystallization temperature of various phases which is usually obtained from a DSC curve such as the one illustrated in Fig. 1.3 (b). This information is used to program the controlled crystallization of BG in an electric furnace to form BGC with desired crystalline phases. Since the BG composition is optimized to mimic bone and its bioactivity, one or more bone mineral phases such as hydroxyapatite (HA, $Ca_5(PO_4)_3(OH)$), wollastonite (W, $CaSiO_3$), calcium sodium phosphate (CNP,

$NaCaPO_4$) or sodium calcium silicate (SCS, $Na_2Ca_2Si_3O_9$) generally crystallize during their heat treatment. Thus, BGCs are multiphase materials, which exhibit better mechanical and thermal properties than their parent BG.

The sol–gel route has become a popular alternative to melt-quenching technique. It is a chemistry-based synthesis route where a solution containing the compositional precursors undergoes hydrolysis and condensation reactions at room temperature to form a gel. The gel is a wet inorganic network of covalently bonded silica. It can then be dried and thermally stabilized at low temperatures (~100 °C) to become a porous glass with large surface area and porosity. Synthesis of silica-based bioactive glass by sol-gel route using metal alkoxides, *e.g.* tetra ethyl ortho silicate as the precursor for silica was first demonstrated in 1991 [RWJO89a]. The sol-gel process involves the following steps:

1) Hydrolysis of an appropriate metal alkoxide under acidic or basic environment.
2) Addition of network modifiers and other additives to the solution to obtain the desired product composition.
3) Gelation of the solution (ageing is also required to ensure complete gelation).
4) Freeze drying of the gel to obtain a dry powder.
5) Calcination of the powder to remove extra-gaseous substances.

Choice of precursors and control of the hydrolysis and condensation reactions are important to obtain a fully amorphous glassy structure using this method. It has been observed that inability to control the above reactions leads to the formation of BGC rather than BG in multicomponent systems.

The following methods have also been successfully used to prepare bioglasses:

Micro-emulsion is a thermodynamically stable, transparent and isotropic dispersion of two immiscible liquids such as water and oil stabilized by surfactant molecules at the water–oil interface. In this method, the precursor particles of hydroxide(s) or oxalate(s) are first formed in a micro-emulsion system. After drying and calcination of the precursor powder, the desired oxide system is obtained. SiO_2-CaO-P_2O_5 bioglass nanoparticles have been synthesized by the micro-emulsion method [MZHU12a].

Solvent casting involves dissolving a polymer in an organic solvent, mixing it with bioactive ceramic or glass granules and casting the mixture in a predefined 3-D mold. The solvent is subsequently allowed to evaporate. 45S5 bioglass-poly(D,L-lactide) composite has been prepared by solvent casting [LAUR02a].

Gas phase (or flame spray) synthesis uses metal–organic precursor compounds to produce nanoparticles at temperatures above 1000 °C. The basic principle of all gas phase synthesis methods is the formation of molecular nuclei followed by condensation and coalescence of the nuclei, thereby leading to the growth of nanoparticles at high temperatures. Flame spray synthesis is used to produce megatons of silica and titania nanoparticles per year [BRUN06a].

Hydrothermal synthesis includes the crystallization of materials from high-temperature aqueous solutions at high pressures. Different forms of ceramics can be prepared with hydrothermal synthesis such as powders, fibers, single crystals, monolithic ceramic bodies, and coatings on metals, polymers, and ceramics. The process utilizes single or heterogeneous phase reactions in aqueous media at elevated temperature ($T > 25$ °C) and pressure ($P > 100$ kPa) to crystallize ceramic materials directly from a solution. The synthesis depends on the solubility of materials in hot water at high pressures and the crystal growth takes place in an autoclave [SUCH06a].

1.2.5 Review of literature on bioglass and bioglass-ceramics

1.2.5.1 Melt derived glass and glass-ceramics

The pioneering work of Hench and his co-workers mentioned in section 1.2.2

resulted in a wide variety of BGs with different constituents. The following review will briefly capture the contributions made by other researchers to improve the bioactivity and mechanical strength of BG and BGC. Ebisawa *et al.* [YEBI90a] found that P_2O_5 free CaO-SiO_2 glass could bond to living bone. They also observed that addition of Na_2O improved but addition of MgO, B_2O_3, CaF_2, and Fe_2O_3 deteriorated the bioactivity of the glass. Large substitution of Y_2O_3 for CaO in 2.5CaO.2SiO_2 glass had a negative influence on its bioactivity [COST97a]. Apatite forming ability of CaO-P_2O_5-SiO_2-MgO(-Al_2O_3) glasses and glass-ceramics immersed in a pseudo-extracellular fluid decreased when MgO content was more than 8 wt.% [HOLA85a]. Ceravital glasses and glass-ceramics are the first biomaterials containing MgO. Ohtsuki *et al.* [OHTS91a, OHTS92a] obtained KG Cera (2.9 wt.% MgO) and Mina (5 wt. % MgO) from a base ceravital glass composition of (40-50)SiO_2(10-15)P_2O_5(5-10)Na_2O(0.5-3.0)K_2O(2.5-5)MgO (in wt. %). Kokubo *et al.* developed the apatite-wollastonite (A-W) glass with a composition of 4.6MgO.44.7CaO.34SiO_2. 16.2P_2O_5.0.5CaF_2.They also prepared A-W glass-ceramic and A-W tricalcium phosphate glass-ceramic which had high mechanical strength. Other bioactive glass compositions developed over the years contain no sodium or have additional elements incorporated in the silicate network such as fluorine [VITA08a], strontium [GENT10a, DONN10a], iron [HSIC07a], silver [BALA08a, BELL02a], boron [LIUX09a, GORR09a], or zinc [AINA09a, HAIMI09a]. Recently, certain borate and phosphate glasses were successful in healing chronic wounds such as diabetic ulcers which would not heal under conventional treatment [JUNG11a, ABOU09a]. There are large number of reviews in the literature describing various properties and applications of different glass and glass ceramics. Research groups of Kim and Knowles have extensively worked on phosphate based glasses with high dissolution kinetics [JONA03a, KIMH06a, LAKH13a]. The remarkable soft tissue response to these glasses is due to their rapid dissolution characteristics. Boccaccini *et.al* have reviewed the literature on bioglass / glass ceramics for bone regeneration [LUTZ10a, ALEX11a, CHEN06a] and drug delivery [HUMJ12a] applications. Reviews on PLGA/Bioglass® composite for tissue engineering applications [BOCC05a] and nanoscale bioactive glasses for medical applications [GORU10a, EROL13a] discuss the recent advances in these topics. A recent review [JULI13a] discusses the developments in the field of bioactive glass starting from Hench's Bioglass 45S5 to new hybrid materials. Chronology of science and clinical product development of 45S5 bioglass has been recently reviewed by Hench [HENC13a].

1.2.5.2 Magnetic bioglass and bioglass-ceramics

Biocompatible magnetic materials have gained considerable interest due to their biomedical applications such as hyperthermia treatment of cancer [IAVE15a, AJAY07a, QIUH15a, YOLA15a], targeted drug delivery [SERE15a, ACJA13a], contrast agent in magnetic resonance imaging [QIUH15a, ETIN07a, SHAH15a], *etc*. Bretcanu *et al.* [BRET06a, BRET06b, BRET05a] have investigated the processing of SiO_2-Na_2O-CaO-P_2O_5-FeO-Fe_2O_3 glass-ceramics to produce ferrimagnetic bioactive glass-ceramics samples suited for hyperthermia application. These glass-ceramics contain magnetite and hematite crystals in a glassy matrix. The magnetic hysteresis parameters, which are critical for this application, are strongly influenced by the microstructure. Kawasita *et al.* [KAWA05a, KAWA04a, KAWA08a] reported the preparation of pure Fe_3O_4 microspheres, γ-Fe_2O_3 microspherers and zinc ferrite ($Zn_xFe_{3-x}O_4$) in a CaO-SiO_2 based glass matrix for hyperthermia application. One cannot go forward without quoting two excellent patents on this topic, *viz*., U.S. Patent 4323056 entitled “Radio frequency induced hyperthermia for tumor therapy” filed by N.F. Borrelli, A.A. Luderer, G.R.Mansfield, J.N. Panzarino in 1982 and U. S. Patent 6167313 entitled “Targeted Hysteresis hyperthermia as a method for treating diseased tissue filed by B. N. Gray and S. K. Jones in 2000. The highest specific power loss is obtained for samples melted at 1550 °C (29 W/g), which presents the highest hysteresis loop area. Since these applications require magnetic materials which are also biocompatible, several strategies have been used to develop these materials. The most popular method is to have a core-shell structure with the magnetic material forming the core and a biocompatible material such a HA, biocompatible polymers, *etc*., forming the (outer cover) shell. Core-shell nanoparticles with iron or iron oxide core have been extensively studied for this application [QIUH15a, ETIN07a, AJAY07a]. The other approach is to precipitate a magnetic phase in a biocompatible glassy matrix. The advantage of the latter strategy is the relative ease of adapting it for hyperthermia or drug delivery or bone scaffolding application. In this regard, various bioactive glass-ceramic systems containing iron oxide have been investigated [YEBI97a, OHUR04a, HSIC07a, RKSI08b]. Singh and Bahadur [SING99a] have investigated the structural and magnetic properties SiO_2-Na_2O-CaO-P_2O_5-B_2O_3-Fe_3O_4 glass-ceramics. A systematic study has been carried out by Singh *et al.* [RKSI09a] on $(52-x)SiO_2.41CaO.4P_2O_5.3Na_2O.xFe_2O_3$, ($x$ = 0, 2, 4, 6, 8 and 10 mole %) and $34SiO_2.(45-x)CaO.16P_2O_5.4.5MgO.\ 0.5CaF_2.\ xFe_2O_3$ (x = 0, 5, 10, 15 and 20 wt. %) glasses. The glasses which were non-magnetic became glass-ceramics containing bone mineral and ferrimagnetic magnetite (Fe_3O_4) upon heat treatment at temperatures well above their T_g. The magnetic properties of these magnetic glass-ceramics depended on the nature and amount of magnetic content in the glassy matrix. Fe_2O_3 in the glass, reduced to form Fe_3O_4 during the heat treatment in a closed electric furnace. Singh *et al.* showed that it is possible to precipitate a zinc ferrite phase in $(65-x)SiO_2.20(CaO,P_2O_5).15Na_2O.x(ZnO,Fe_2O_3)$ (x = 6, 9, 12, 15, 18 and 21 mole %) glass to obtain ferrimagnetic zinc ferrite with higher magnetization. Their proposal would validated by the work presented in chapter 3 of this thesis.

1.2.5.3 Sol-gel derived glass and glass ceramics

Bioactive glasses and glass ceramics discussed above were in bulk form and were prepared by conventional melt quenching route. Though melt quenching technique has been very successful in the synthesis of bulk glass, it puts restriction on process temperature, porosity, homogeneity, structure and purity of products which are highly desirable parameters for biomedical applications. In early 1990s, sol-gel processing was introduced for the synthesis of bioactive glasses [RWJO89a]. A detailed discussion on the process steps involved in the sol-gel route is presented in chapter 2. The raw materials are high purity liquids, so that the initial purity and homogeneity is usually much greater than that of solid batch components. Considerable porosity could be obtained by removal of liquid traces from the gel. These bioactive glasses have higher bioactivity and resorbability *in vitro*, which make them well suited for bone grafting. Various research groups have employed sol-gel route for preparing bioactive glasses / glass ceramics in binary (SiO_2-CaO), ternary (SiO_2-CaO-P_2O_5) and quaternary (SiO_2-CaO-P_2O_5-Na_2O) systems for biomedical applications. A variety of metal ions such as zinc [AOKI04a], magnesium [FOOL13a], zirconium [RAHP13a], titanium [LENZ02a], boron [YANG12a] and silver [NEZA12a] have been added to bioactive glasses for enhancing the glass functionality and bioactivity. Table 1.2 provides details of sol-gel bioglass and bioglass-ceramic compositions reported in the literature.

Table 1.2: Details of SiO_2-Na_2O-CaO-P_2O_5 based sol-gel bioglasses and glass-ceramics synthesized.

Name	**SiO_2 [mol%]**	**Na_2O [mol%]**	**CaO [mol%]**	**P_2O_5 [mol%]**	**Final product**	**Ref.**
76S, 76SA	76	0	23	1	Glass	RAMI02a
Bio1(1)_TEP_Na	49.15	23.33	25.80	1.72	Glass	SIQU11a
52S4	52.3	13.7	32.3	1.7	Glass	LUCA11a
Bio1(1)_TEP	70	0	26	4	Glass	SIQU13a
Si47P5Q	47	21.5	26.5	5	Glass-ceramic	CATT13a
No name	50	25	21	4	Glass-ceramic	ADAM13a
No Name	45	24.5	24.5	6	Glass-ceramic	POUR14a
S70C30	70	0	30	0	Glass-ceramic	CHEN10a
70S26C4P	70	0	26	4	Glass-ceramic	PADI05a

However, a survey of the literature also shows that fully amorphous bioactive glass is extremely difficult to synthesize by sol-gel route because of spontaneous precipitation of various precursors during polymerization and gelation steps, which are very difficult to control. Several [CATT13a, ESSI13a, HAMI13a, POUR14a] attempts have been made to prepare sol-gel glass with compositions close to bioglass 45S5, but the end products invariably contained crystalline inclusions. Vallet-Regí, *et. al* [RAMI02a] pointed out that the challenge lies in the optimization and control of nitrates and phosphate precursors used in the sol-gel synthesis of bioglass. Attempts to prepare several quaternary bioglass compositions by Padilla *et. al* [PADI05a] and Siqueira *et. al* [SIQU13a] by varying the phosphate precursors resulted in semi-amorphous end products. Though SiO_2-CaO-P_2O_5 compositions containing lower Na_2O content have been obtained by Lucas *et al.* in completely amorphous structure [LUCA11a], fully amorphous sol-gel derived 45S5 glass composition has been elusive so far. Surprisingly, after 40 years of research on bioactive glasses by numerous research groups, no other bioactive glass composition has been found to have better biological properties than the original Bioglass 45S5 composition. Before going forward, it is worth understanding why an amorphous bioactive composition is required. Being amorphous in structure, bioactive glasses form bond to bone much quicker than crystalline bioceramics. Also, dissolution of a random network begins much earlier than that of crystalline network, which leads to rapid HA formation on the surface [HENC05a]. It is indeed very rare to find reports of oxide glasses containing small amounts of iron oxide which exhibit strong magnetic behaviour and there are no reports in the literature on fully amorphous bioglass compositions containing iron oxide exhibiting significant magnetic behaviour. Thus, one of goals thesis is to understand why the Bioglass 45S5 is so difficult to synthesize by sol-gel technique and to optimize potential precursors and processing conditions to obtain fully amorphous 45S5 glass composition by this route.

1.3 Polymeric biomaterials

Artificial biomaterials are limited in the functions they can perform and transplants are limited by availability of organs and problem associated with immune compatibility. Hence, there is keen interest in the regeneration of diseased or damaged tissue guided by the structure of a substrate made of a synthetic material called scaffold. In this regard, polymers have the remarkable ability to support the mechanical needs of a wide variety of biomedical applications [LEND11a]. Investigators have mainly concentrated on synthetic biodegradable polymers approved by the United States Food and Drug Administration (FDA) as suture materials for developing scaffold substrates. Various types of natural polymers (collagen, hyaluronic acid, chitosan and alginate, *etc.)* and synthetic polymers polyvinyl alcohol (PVA), polyvinyl pyrrolidone (PVP), polyethylene glycol (PEG), polylactic acid, polycaprolcatone (PCL), polyethylene oxide (PEO), poly 3-hydroxybutyrate and polyglycolic acid have been investigated for various biomedical applications such as wound dressing, bone regeneration, tissue scaffoldings [LEND11a, KAMO14a]. However, these polymers are not osteoconductive and do not directly bond to bone. Despite this, their close resemblance to natural polymeric tissue components such as collagen, polymeric materials has led to their use in implants. Polymers have the advantage that they can be easily fabricated into many forms such as fibers, films, membranes and viscous liquid. Polymeric composites containing osteoconductive component(s) can overcome the above mentioned limitations with polymers. These polymeric composites in fibrous form are the potential candidates in various biomedical applications such as bone scaffold, tissue engineering, and wound care applications. Following section showcases some popular techniques for preparing fibrous polymeric biomaterials.

1.3.1 Synthesis of fibrous polymeric biomaterials

Ever expanding demand for nanofibers stems from the fact that this form of polymeric nanocomposites mimics the natural extra-cellular matrix (ECM) [SEEM08a]. To prepare these biomaterials and their composites, various techniques and combination of techniques are being adopted. Through electrospinning technique, biocompatible polymer composites can be spun into a mesh of nanofibers. This nanomesh has high surface area which can mimic the structure and function of ECM. It also acts as scaffold allowing cells to adhere, proliferate, differentiate and develop into functional tissue [RAMA05a, BHAR10a, SEEM08a]. Dressings based on electrospinning technique are expected to heal the wound faster by encouraging cell-to-cell interactions, cell migration and cell morphogenesis within body environment. The electrospinning apparatus mainly consists of a high voltage power supply, a needle or spinneret and a grounded collector plate. A syringe feeds a polymer solution at a controlled rate through a metallic needle, which is connected to the positive terminal of a high voltage power supply. The conductive plate or drum serving as the cathode completes the electrical circuit by creating a strong electric field between the needle and the plate.

Electrostatic and surface tension forces at the tip of the needle generate nanojets of polymer solution which condense as a nanofibrous mesh on the cathode plate. This simple and laboratory scale technique is employed in this thesis. A brief account of other contemporary fiber fabrication techniques is given below.

Large quantities of nanofibers can be produced using laser spinning technique with specific and controllable chemical compositions without the necessity of any chemical additives or post-preparative heat treatments. The laser spinning technique essentially involves quick heating and melting of a small volume of the precursor material using a high power laser. A supersonic gas jet injected into the melt volume quickly stretches and cools the molten material. Long glass fibers with high aspect ratios have been produced by the elongation of the viscous molten material. The final product is usually in amorphous form because of the high cooling speed. 45S5 and 52S4.6 bioglass nanofibers have been prepared by this method [QUIN09a].

Centrifugal spinning and infusion gyration are promising techniques for producing fibers in meso- to nano-scale from polymeric solutions. Centrifugal spinning (or pressurized gyration process) relies on application of centrifugal force and dynamic fluid flow in a sealed cylindrical vessel containing polymer solution to jet out fibers [SUNT13a]. Zhang *et al.* [SIQI15a] have recently proposed an infusion gyration method which is actually a centrifugal spinning with controlled infusion rate.

1.3.2 Review of literature on polymeric biomaterials

Polymeric biomaterials and their composites have been extensively explored for tissue engineering, wound care, drug delivery, organ replacement and bone related applications [DANI08a, LAKS32a, SEAL01a, MICH07a, HUAN03a, KAMO14a]. Water solubility, hydrophilicity, biodegradability and biocompatible nature make polymeric biomaterials potential candidates for biomedical applications. Most commonly utilized biodegradable polymers are the polyvinyl alcohol (PVA), polyvinyl pyrrolidone (PVP), polyethylene glycol (PEG), polylactic acid (PLA), polycaprolcatone (PCL), polyethylene oxide (PEO), poly 3-hydroxybutyrate (PHB) and polyglycolic acid (PGA) [LEND11a, LAUR02a, DANI08a, LAKS32a, SEAL01a, MICH07a, KAMO14a, HUAN03a, RASI14a]. Hydrocolloids, hydrogels, alginates, collagen, thermoplastic polyurethane, biodegradable polymer scaffolds, medical foams and medical fabrics are some examples of wound care products that have been prepared by gel formation, compression molding, die-cutting, gamma radiation and fiber fabrication techniques. A variety of nanofibrous membranes have been obtained by electrospinning technique [RAMA05a, HUAN03a, SEEM08a, BSUN14a]. Since water soluble polymers have distinct advantages such as ease of preparation, better water uptake profile and degradation behaviour in aqueous body fluid environment, the present focus will be on them. Hybrid polymer wound dressing materials have been reported by combining PVA and PVP [NRAJE13a, AYTI14a, UMAS14a]. Aytimur and Uslu [AYTI14a] have proposed electrospun PVA-Polyacrylic acid polymer containing chitosan, and PVP + PVP-iodine complex for wound healing application. Maheshwari *et al.* [UMAS14a] have reported the effects of applied electric field and polymer concentration on the morphology of electrospun PVA-PVP nanofibers and their biocompatibility with mouse cells (NIH 3T3 fibroblast). However, the main focus of the earlier studies has been limited to fabrication and optimization of PVA-PVP blends for obtaining composite nanofibers. Wound closure characteristics such as cell viability of native skin cell types and antibacterial properties of PVA-PVP blend nanofibers have not been explored so far. In chapter 5, interactive wound closure characteristics of electrospun PVA-PVP nanofibrous membranes have been explored. By combining biodegradability, bioactivity and mechanical competence, hybrid and nanocomposite materials offer an exceptional opportunity to produce scaffolds with desired biological and physical properties. Since natural bone matrix is a composite of biological ceramic (hydroxyapatite) and polymer (collagen), it is not surprising that nanofibrous composite scaffolds containing synthetic or natural biomaterials have been explored for bone tissue engineering application [JAYA10a, THEI09a, THEI08a, HUTM00a, BOCC05a]. Kim *et. al* [ROMA13a, KIMH06a] have extensively explored the application of nanofibrous composite biomaterials for tissue regeneration. One of the main objectives of current research is to develop biodegradable and bioactive hybrid fibrous scaffolds by a combination of sol-gel and electrospinning processes and study the effect of hybridization process on physicochemical, mechanical and biological properties of the resultant hybrid scaffolds. Bioglass/HA based nanocomposites fibers have been obtained by using a surfactant that mediates the interface of the hydrophilic nanocrystals and the hydrophobic solution [SRIN12a, REZW06a]. Subsequently, biodegradable synthetic polymer solutions containing bioactive inorganic nanoparticles such as HA and silica xerogels have been fabricated [SRIN12a, PRAB09a, NAND10a, EJLE10a]. Li *et al.* [LING12a] reported a bioactive PCL/HA nanofibrous scaffold for bone regeneration. Prabhakaran *et al.* [PRAB09a] fabricated nanocomposite PLLA/collagen/HA nanofibrous scaffold which promise enhanced bone regeneration.

1.4 Selected biomedical applications

Applications of biomaterials in health care are extensive and it would be difficult to elaborate on all of them. Here, some selected biomedical applications that are closely related to the biomaterials synthesized in this thesis work are reviewed. Investigations reported in this thesis have been carried out with these applications in mind.

1.4.1 Tissue engineering

Tissue engineering allows organs to be grown from synthetic implants. Bioactive materials seeded with living cells serve as scaffold for living cells to adhere with it. When the cells proliferate, they fill up the scaffold and grow into 3-D tissue. Subsequently, blood vessels attach themselves to the new tissue. Hence, a scaffold possessing a suitable surface chemistry is required to promote cell attachment, proliferation and differentiation [CAPL99a, BREK98a]. Mechanical properties of the scaffold should be compatible with the host tissue and the degradation product should be non-toxic and easy to excrete. So, with time, the scaffold dissolves and the newly grown tissue eventually blends with its surroundings. For bone tissue engineering, scaffold architecture should mimic that of cancellous bone, which is characterized by a random pore structure [BURG00a, SALG04a]. From the biological perspective, bone growth requires cells, ECM, intracellular communications, cell-matrix interactions and growth factors [YANG01a]. Despite the availability of materials with appropriate biological and structural properties, improvement are needed to satisfy all the requirements for bone regeneration. Biocompatible nanofibrous polymer scaffolds containing porous bioglass as filler can serve as effective bone regeneration scaffolds.

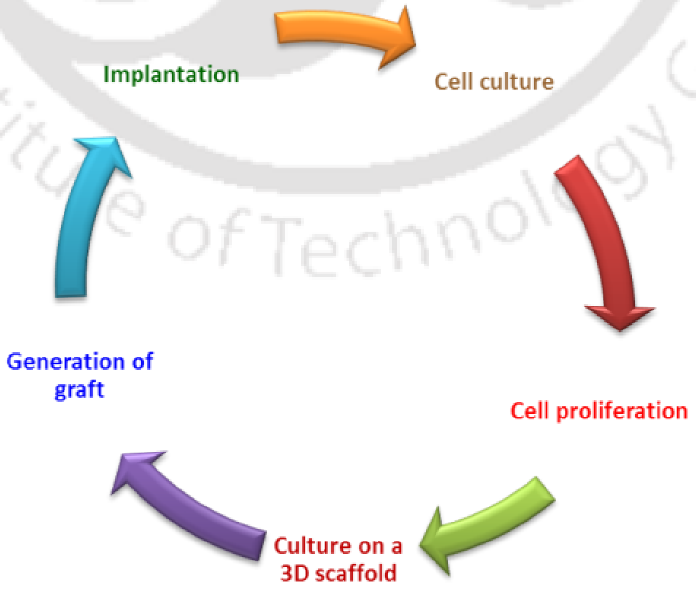

Fig. 1.7: Steps involved in tissue engineering using a porous biomaterial.

1.4.2 Hyperthermia treatment of cancer

Hyperthermia treatment of cancer is based on the experimental finding that cancerous cells die when heated above 42 °C, whereas healthy tissue cells can withstand temperatures more than 46 °C [MNRA11a, OHUR04a, YEBI97a]. In magnetic hyperthermia, a thermo-seed which is a biocompatible magnetic material that is implanted near a cancerous tissue is subjected to an alternating magnetic field. The magnetic field provides the energy necessary to reorient the magnetic particle's magnetic moments. This magnetic energy, when dissipated, is converted into thermal energy which raises the local temperature. When the local temperature rises above 42 °C, cancerous cells in the vicinity are selectively killed [BERT02a]. Heat above 41 °C also pushes cancer cells toward acidosis (decreased cellular pH) which decreases the cell viability and transplant ability [BERT02a]. Bioactive glass-ceramics containing magnetic phase(s) can serve as fillers for cavities created by removal of cancerous tumor. These implants can also serve as thermos-seeds for preventing proliferation of residual cancerous cells by an externally applied alternating magnetic field.

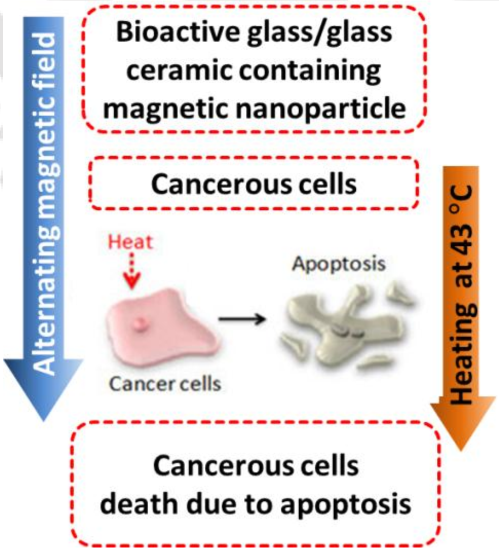

Fig. 1.8: Cancerous cell death due to apoptosis by means of magnetic hyperthermia.

1.4.3. Wound care dressings

Wound dressing can be classified into three categories, *viz.*, passive, active or interactive dressing. Passive dressings merely protect wounds, whereas active dressings create a moist environment and promote healing. The term interactive refers to activities of dressings with cellular environment during the wound healing process. So, a dressing which (a) absorbs excess exudate and prevent the wound from desiccation, (b) provides a barrier to bacteria and minimize the contamination of the wound, and (c) is free of toxic particulate components, qualifies to be an interactive wound dressing [SUJA12a]. Wound healing is the complex pathway of biological process and cellular events which concerns replacing damaged tissue and restoration of tissue integrity. Interactive dressings mimic the ECM and facilitate biochemical reactions and cell responses favourable to wound healing. Epidermal cells which spread and cover the wound surface from the edges required a regular supply of blood and nutrients. Dry crusted wounds reduced this supply and thereby slow down the rates of epithelialization. [ENNI12a]. Interactive wound dressings maintain a moist environment and thereby decrease cell dehydration and improve wound healing.

Indian Institute of Technology Guwahati

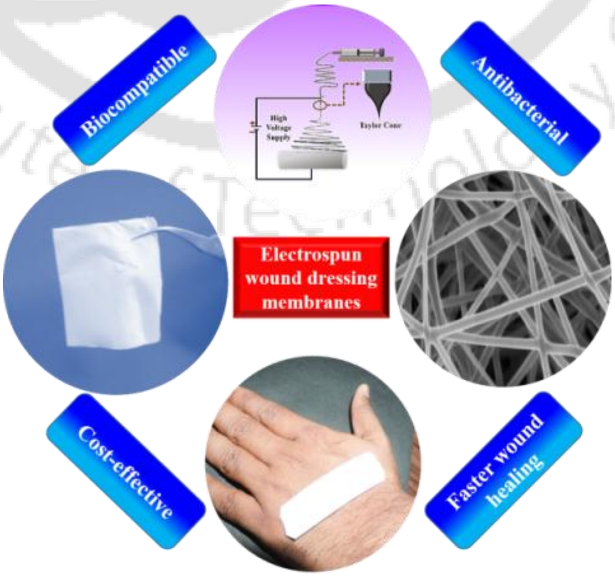

Fig. 1.9: Electrospun polymeric membranes in wound care.

1.5 Motivation and scope of the thesis

This thesis work attempts to develop biomaterials which can address some of the critical issues associated with materials for some specific biomedical applications apart from pursuing some problems on purely scientific quest.

The first pursuit is concerned with the development of efficient thermos-seeds from bioactive glasses containing magnetic entities. Fe_2O_3 has not only been the most favoured, but also seems to be the main additive used to derive bioglass-ceramics containing ferrimagnetic magnetite. An earlier study showed that Fe_2O_3 can be introduced in the place of silica in the best known bioactive glass *i.e.*, the Hench's 45S5 to yield ferrimagnetic bioglass-ceramics by heat treatment [RKSI09a, RKSI08a, RKSI08b, RKSI08c]. Attempts improve the magnetic properties of this glass-ceramic by heat treatment beyond 1000 °C ended up in deteriorating its magnetic properties. Hence, a systematic investigation of the structure and magnetic properties of $41CaO.44SiO_2.4P_2O_5.8Fe_2O_3.3Na_2O$ (mol%) Ca/P molar ratio of 1.67 was taken up for study. In a quest to find bioactive glass-ceramics with better magnetic properties for making efficient thermos-seeds, $15(ZnO,Fe_2O_3).50SiO_2.20(CaO,P_2O_5).15Na_2O$ (in mol%) glass-ceramics with molar ratios Ca/P =1.67 and Fe/Zn = 6.5 was taken up for study. The motivation was to obtain bioglass-ceramics containing $Zn_{0.4}Fe_{2.6}O_4$ phase which has high (192 emu/g) saturation magnetization by appropriate heat treatment.

The second quest had dual motivations, *viz.*, to tackle the difficult problem of preparing a completely amorphous sol-gel based 45S5 bioglass and to attempt to introduce a magnetic entity in the sol-gel 45S5 bioglass. A survey of the literature on sol-gel based 45S5 bioglass will reveal that the attempts invariably yielded gel powders containing crystalline inclusions. The sol-gel procedure leading to the formation of 45S5 bioglass was carefully studied and the need to choose the right precursors and control the sol-gel reactions was realized. The recipe to obtain fully amorphous 45S5 bioglass gel powders and fully amorphous magnetic bioglass are described in chapter 4 of this thesis.

The third tryst was to develop polymeric nanocomposites which are in demand for bone scaffold application. While investigating the properties of electrospun PVA and PVP, their ability to blend became evident. Since both these polymers had different responses to the physiological environment, it was anticipated that the blends would have useful biomedical properties. Electrospun membranes of PVA-PVP blends turned out to be promising and low-cost interactive wound dressing materials. The investigations carried out on these membranes are presented in chapter 5. Having optimized both the sol-gel route for preparing 45S5 bioglass and magnetic bioglass, and the electrospinning process for obtaining nanofibrous mesh, the enthusiasm to prepare the composite nanofibers scaffolds was natural. Composite membranes exhibiting good mechanical strength, bioactivity and bone cell viability have been obtained. These are also described in chapter 5.

Indian Institute of Technology Guwahati

Chapter 2

Experimental Techniques

In this chapter, the experimental techniques used in the current investigations are discussed together with the relevant theory associated with these techniques and examples. Specific instruments used and the measurement methodology employed are also discussed. The experimental results presented in chapters 3, 4 and 5 are based on the experimental procedures outlined in this chapter.

2.1 Preparation of samples

2.1.1 Preparation of bulk glass and glass-ceramics

Bulk $41CaO.44SiO_2.4P_2O_5.8Fe_2O_3.3Na_2O$ and $15(ZnO,Fe_2O_3).50SiO_2.20(CaO,P_2O_5).15Na_2O$ glass-ceramics discussed in chapter 3 were prepared by melt quenching route. In the melt-quenching method, appropriately weighed quantities of the constituent compounds are thoroughly mixed in an agate pestle and mortar. In order to determine the correct mix of raw materials for preparing a glass with a specific composition, a batch calculation is needed [SHEL97a]. Batch calculation for $44SiO_2$-$41CaO$-$4P_2O_5$-$8Fe_2O_3$-$3Na_2O$ composition is illustrated below to serve as an example of the procedure followed:

Source compounds taken for CaO, P_2O_5, and Na_2O are $CaCO_3$, $(NH_4)_2HPO_4$ and $Na_2CO_3.H_2O$, respectively.

- Mol. wt. (MW) of glass (A) = [(MW of SiO_2 * 44) + (MW of CaO * 41) + (MW of P_2O_5 * 4) + [(MW of Fe_2O_3 * 8) + (MW of $N_{a2}O$ * 3)] / 100 = 69.741 g/mol.
- Wt. fraction of source compound (B) = (wt. % of source compound * MW of source compound/MW of glass (A) * 100.
- Gravimetric factor (C) = MW of each batch compound / MW of corresponding source component.
- Batch compounds for 1 g of $44SiO_241CaO4P_2O_58Fe_2O_33Na_2O$ glass = (B) * (C)

The thoroughly mixed charge was taken in a platinum crucible and calcined between 600 °C to 800 °C in an electric furnace to remove extra gaseous content. To ensure complete calcination, the above process was repeated after regrinding and mixing the charge again. After allowing for complete calcination, the temperature of the charge was increased to melt it completely. The molten liquid was held at this temperature for 1–2 h for homogenization. The melt was then poured on a copper plate at room temperature and pressed with another copper plate to quench the molten liquid and form glass samples with thickness of a few millimeters. The as-quenched glass was annealed just below their glass transition temperature (T_g) for an hour to remove residual stresses accumulated during the quenching process. The melt quenching process is schematically explained in Fig. 2.1.

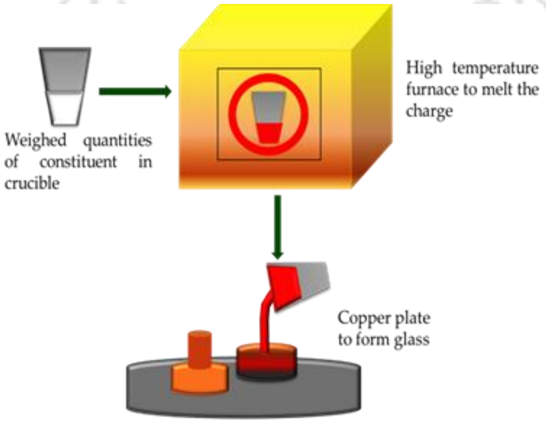

Fig. 2.1: Schematic diagram of the melt quenching route for preparing bulk glass.

As-quenched glass was then heat treated in air at different temperatures (T_A) above T_g for different annealing time (t_A) to induce crystallization of bone mineral and magnetic phases and form glass-ceramics. Controlled heat treatment of glass based on the glass transition and crystallization temperatures and kinetics could yield bioglass-ceramics with optimized amounts of desired crystalline phases.

2.2.2 Preparation of nanoporous glass and glass ceramics

Nanoporous glasses were prepared using a modified sol-gel methodology. The step-wise procedure followed for the preparation of sol-gel 45S5 bioglass is expressed in the form of a flow chart in Fig. 2.2(a). Tetraethyl orthosilicate (TEOS) was used as the precursor for the glass former, *viz.,* silica. Calcium nitrate tetrahydrate ($Ca(NO_3)_2.4H_2O$) and sodium nitrate ($NaNO_3$) were used as precursors for network modifiers CaO and Na_2O. Three phosphate precursors, *viz.*, phosphorous pentaoxide (P_2O_5), phosphoric acid (H_3PO_4) and di-ammonium hydrogen orthophosphate $(NH_4)_2HPO_4$ were independently used as the phosphate precursor.

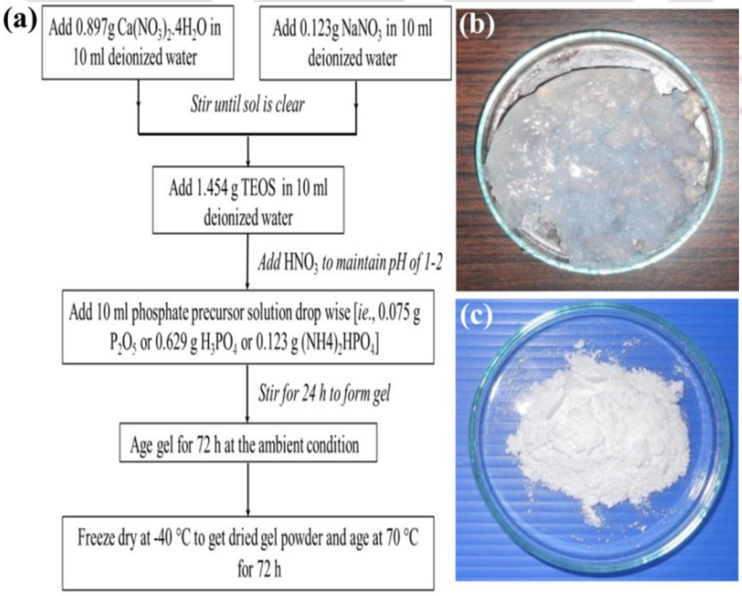

Fig. 2.2: (a) Flowchart describes the steps followed to prepare 45S5 bioglass by sol-gel route. Pictures show (b) as-prepared gel form and (c) the final product after thermal stabilization.

The reactants were taken in proportions required to obtain a final product with the 45S5 composition, *viz.*, 45 wt.% SiO_2, 24.5 wt.% Na_2O, 24.5 wt.% CaO, and 6 wt.% P_2O_5. Required amounts of precursors were calculated using the batch calculation described in section 2.2.1. Gel form of samples shown in Fig. 2.2 (b) was aged for 3 days at ambient conditions and freeze dried at -40 °C. As-dried powder was heat treated at 70 °C for 3 days to eliminate nitrates and other unreacted substances. The last step represents thermal stabilization of the powders in which residual nitrates and other unreacted substances are removed in gaseous form leaving behind a highly porous and gelatinous powder shown in Fig. 2.2 (c). The same procedure was adopted for preparing all the sol gel glasses discussed in chapter 4 and 5. In order to obtain glass-ceramics, the gel powders were further heat treated above their T_g at different temperature to induce crystallization in the glassy matrix.

2.2.3 Preparation of nanofibrous memebranes

Electrospinning (ES) technique was used for producing nanofibrous membranes from polymer solutions. The electrospinner (Nabond NEU), the experimental arrangement and the final product are depicted in Fig. 2.3. In ES, a charged polymer solution is ejected as nanojets from the tip of the metallic needle (anode). These continuous nanojets condense to form a nanofibrous mesh on the cathode.

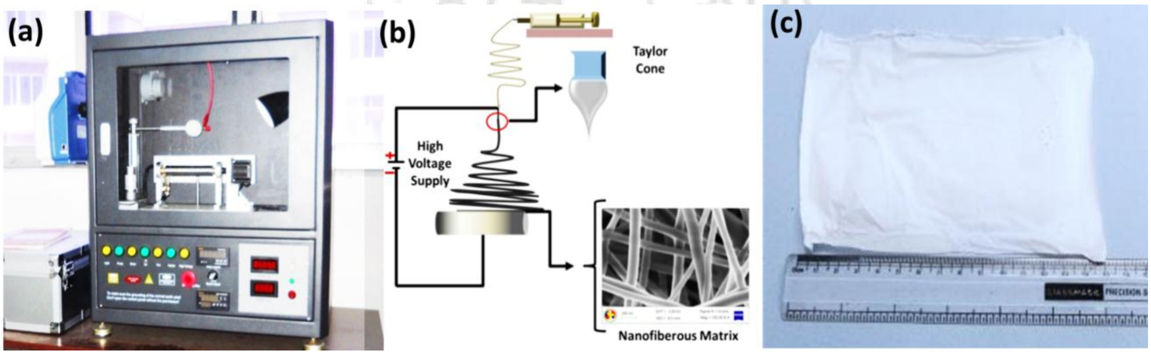

Fig. 2.3: (a) Photograph of electospinning setup, (b) schematic of experimental design and (c) photograph of an electrospun membrane.

Many parameters influence the ES process, which also have a direct bearing on the morphology of the resultant fibers. Among these, the following solution, processing and ambient parameters are the most important ones [RAMA05a]:

- Solution parameters
    - Type of polymer and its molecular weight
    - Type of solvent
    - Concentration of the polymer
    - Viscosity, conductivity and surface tension of the solution
- Processing parameters
    - Electric field strength
    - Distance between nozzle (metallic needle, anode) and collector (cathode)
    - Solution flow rate
    - Shape and movement of the collector
- Ambient parameters
    - Temperature
    - Humidity

Processing parameters were optimized for ES of PVA and PVA-PVP solutions as the first step in this thesis work. Viscosity and electrical conductivity of the polymer and polymer bioglass composites solutions were measured using a viscometer (FungiLab, ViscoBasic Plus) and conductivity meter (TESTRONIX 15), respectively. Measured viscosity and conductivity of polymer blend and polymer composite solutions are tabulated in respective chapters of the thesis. A drum shaped collector (cylinder), rotating about its axis at ~300 rpm was used as the collector of the nanofibrous membranes. A constant solution feed rate of ~2 ml/h was used in all experiments. All solutions were electrospun under applied electrical potential difference of 12~20 kV with a nozzle to collector distance of ~15 cm. All the experiments were performed at ambient conditions. The need to optimize these parameters is demonstrated below. FESEM images displayed in Fig. 2.4 (a, b) show electrospun PVA nanofibers exhibiting beads and irregular morphology. Fig. 2.4(c) exhibits continuous nanofibers with smooth morphology and narrow size distribution, indicating that the ES process is optimized for this polymer solution. The table given below the micrographs in Fig, 2.4 gives the values of the critical ES parameters (others such as nozzle-collector distance, movement of collector, etc. were kept fixed). It is evident that solution concentration is the major factor which determined the quality of the PVA fibers in this case study. In order to obtain the viscosity (η) range between 230 – 260 cP, the concentration of PVP in the aqueous solution should be ~8 w/v%. It is obvious that electrical conductivity of PVA does not change much in the 5-20 w/v% range. Hence, Fig. 2.4 (a) shows bead formation and fiber discontinuity due to low PVA concentration, whereas Fig. 2.4(b) shows ribbon like flat fibers and large size variations due to high concentration of PVA in the ES solution.

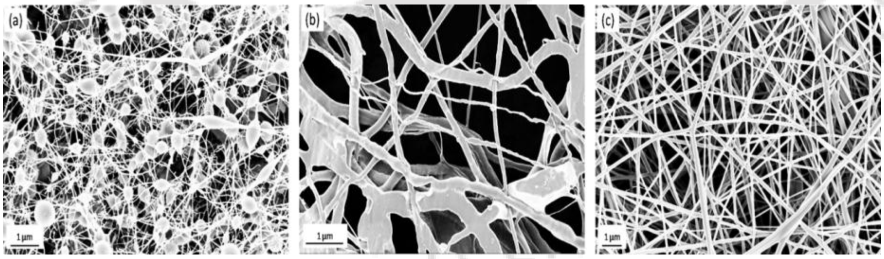

η (cP)	117	367	249 (230-260)
σ (μS)	176	180	189
Conc. w/v %	5	20	8
E (kV)	12~20	12~20	12~20
dV/dt (ml/h)	2	2	2

Fig. 2.4: FESEM images of PVA fiber mats electrospun with aqueous solutions of (a) 5, (b) 20, and (c) 8 w/v % PVA. Table lists the values of critical ES parameters in each case.

2.2 Characterization techniques

Techniques employed for determining structural, thermal, magnetic, mechanical, bioactive and surface properties of the biomaterials prepared in this thesis work are discussed in the following subsections.

2.2.1 Morphological and structural characterization

2.2.1.1 Powder X-ray diffraction

X-ray diffraction (XRD) is the primary structural probe used for verifying the amorphous nature of glasses and to study the phase purity and crystal structure of glass-ceramics. Characteristic X-rays emitted by Cu, Mo, *etc.* have wavelengths of the order of interatomic distances in solids. A periodic arrangement of atoms as in crystals can diffract these X-rays whenever the Bragg condition for constructive interference of X-rays reflected from consecutive layers of a plane is satisfied [BDCU01a]. The condition for diffraction of a collimated beam of X-rays with wavelength λ (≈ 0.5 – 2.0 Å) incident on a crystalline sample is given by the Bragg's law,

$$2\, d_{hkl} \sin\theta = n\lambda \qquad (2.1)$$

where d_{hkl} is the spacing between atomic planes with Miller indices *hkl* in the crystalline sample, θ is the angle of incidence of the X-rays beam with the atomic plane, *n* represents the order of diffraction (we consider only the first order diffraction, and $n = 1$, because higher order peaks are too weak to detect experimentally). The intensity of the diffracted X-rays is measured as a function of the diffraction angle 2θ. The position and intensity of the diffraction peaks are characteristic of the crystallographic structure and atomic composition of the material. XRD patterns provide information on crystal phases, lattice parameters, crystallite size and strain in the material. Unlike single crystal X-ray diffractometers, powder diffractometers can provide information on polycrystalline and multiphase solids available in finely powdered form.

X–ray diffraction patterns of the synthesized nanostructured samples were obtained using a commercial rotating anode based powder X-ray diffractormeter (TTRAX III, Rigaku 2500) using Cu K_α (λ = 1.5406 Å) X-rays. A photograph of the diffractometer is shown in Fig. 2.5(a). All measurements were carried out at an acceleration voltage of 50 kV and tube current of 200 mA. The scanning step size was 0.02 - 0.03°.

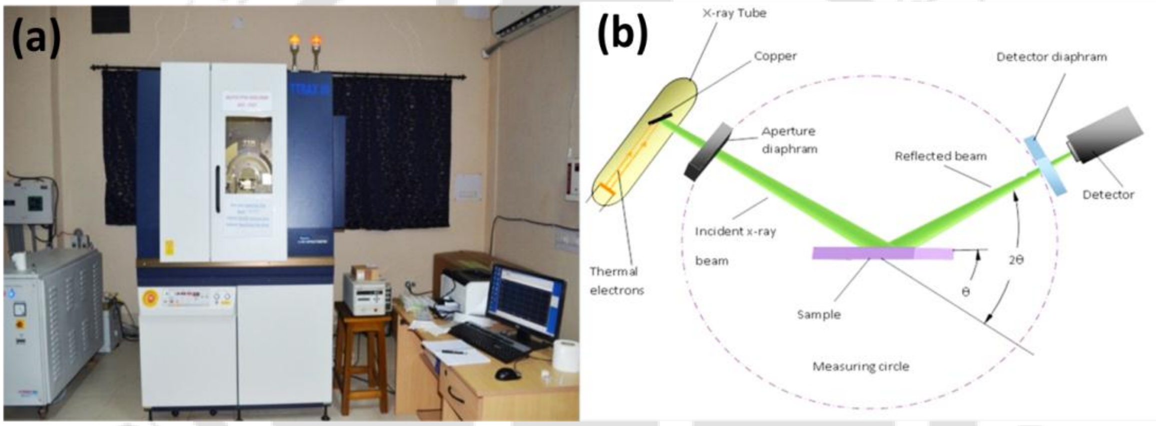

Fig. 2.5: (a) Photograph of Rigaku TTRAX III, 2500 powder X-Ray diffractometer, and (b) schematic diagram of the Bragg-Brentano geometry used for measurement.

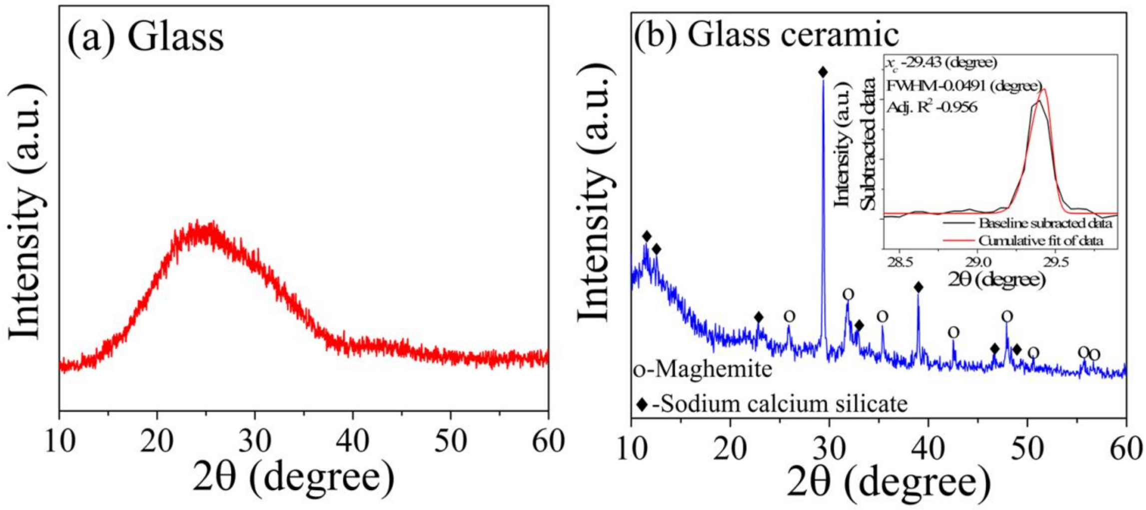

Fig. 2.6: Typical XRD patterns of (a) glass and (b) glass-ceramic samples. Inset in figure shows the Gaussian profile fit to the primary peak after baseline subtraction.

Typical XRD patterns obtained for a glass and a partially crystalline (glass-ceramic) sample are depicted in Fig. 2.6. Broad hump like features with no Bragg-like peaks observed in Fig. 2.6(a) is the signature of a completely amorphous glass. Fig. 2.6(b) shows the typical XRD pattern of a glass-ceramic containing multiple crystalline peaks. Crystalline phase analysis of the sample from such a pattern with broadened an overlapping peaks is difficult using standard procedures like Rietveld refinement [WEB_INGa]. Realizing this difficulty, a simple quantitative analysis based on comparing the integrated intensity of the primary diffraction peaks of various phases was performed. For this, the peak intensities were normalized with respect to the intensity of the strongest peak in the pattern after background subtraction. Then the ratio of integrated intensity of the strongest (primary) peak of each phase was calculated to estimate the percentage of each phase present in the sample. The Gaussian profile fitting used in this process for one peak is depicted as inset in Fig. 2.6 (b).

The broadened Bragg peaks in Fig. 2.6(b) indicate that the precipitates are nanocrystalline in size with considerable amount of internal strain. The average size (d_{av}) of the fine crystallites and the microstrain (ε) can be estimated from the broadened peaks using Williamson–Hall relation [GKWI52a],

$$\beta \cos\theta = K \lambda / d_{av} + 4 \varepsilon \sin\theta \qquad (2.2)$$

where β is the full width at half maximum of the Bragg peak (in radians), θ is the diffraction angle at the peak maximum, and K is a constant which depends on the shape of the crystallite. Here, it is taken as 0.89 by assuming the shape of the crystallites to be spherical. The first term in Eqn. 2.2 is the Schërrer's relation which presumes that the peak broadening is entirely due to the small crystalline size of the sample, or

$$d_{av} = K \lambda / \beta \cos\theta \qquad (2.3)$$

This relation is used to estimate d_{av} of nanocrystallites from XRD patterns with very few peaks or in the case of samples with no internal strains. The instrumental broadening effect has been taken into account in the estimation procedure. The data base from the International Center for Diffraction Data (ICDD) was used for identifying various crystalline phases present in the glass-ceramics by search and match procedure with the XRD patterns of glass ceramics. Table 2.1 shows the ICDD PDF files used for phase analysis in this thesis work. New crystal phases whose XRD patterns are not available in ICDD have to be generated by simulating them using the unit cell. Commercial software (CaRIne Crystallography 3.1) was used for generating the unit cells and simulating the XRD patterns of new crystal phases in this thesis work.

Table 2.1: ICDD PDF files of bone mineral and magnetic phases of interest.

Phase	**Chemical formula**	**ICDD PDF #**
Hydroxyapatite (HA)	$Ca_5(PO_4)_3(OH)$	74-0566
Calcium sodium phosphate	$NaCaPO_4$	76-1456
Magnetite	Fe_3O_4	85-1436
Zinc ferrite	$ZnFe_2O_4$	82-1042
Hematite	α-Fe_2O_3	85-0599
Wollastonite	$CaSiO_3$	84-0655
Sodium calcium silicate	$Na_2Ca_2Si_3O_9$	78-0364
Calcium phosphate	$Ca_4P_6O_{19}$	15-0177

Grazing incidence (or glancing angle) X-ray diffraction (GI-XRD) is a commonly used method for structural evaluation of surface layers or thin films. In this method, the angle of incidence is kept very low (to a few degrees) so that the depth of penetration of the X-rays is small and limited to the thickness of the layer of interest. By varying the grazing incidence angle, structure of different layers in a multi-layered film stack can be probed. Unlike the Bragg-Brentano geometry shown in Fig. 2.5(b), a focusing circle is not maintained in GI-XRD geometry. GI-XRD is a non-focusing geometric arrangement which makes use of parallel, rather than divergent X-rays diffracted from suitably oriented crystallographic planes. A GI-XRD attachment (soller slit, in this case) placed between the diffracting planes and detector slit absorbs converging and diverging diffracted X-rays and allows only parallel X-rays to pass. The GI-XRD measurements were performed in the 2θ range of 20 – 50° using Cu K_α (λ = 1.5418 Å) radiation at a scan rate of 1°/minute and with 2° glancing angle against the incident beam on the specimen surface. All the XRD data were collected with 1.2 kW power (40 kV / 30 mA). This technique was used in *in vitro* bioactivity study of samples discussed in section 2.2.5.1.

2.2.1.2 Transmission Electron Microscopy

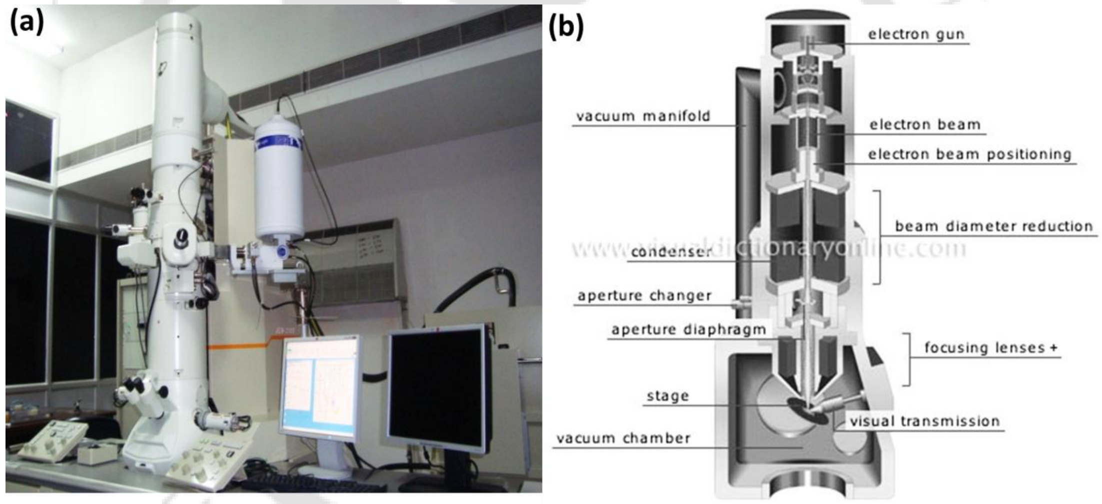

Fig. 2.7: (a) Photograph of the TEM used and (b) a schematic view of its components [WEB_SCIE].

TEM is a powerful structural tool which uses electron diffraction to provide high resolution imaging of structures close to the atomic level (0.2 nm). High resolution TEM (HRTEM) can give an image of the crystal lattice and line defects (or dislocations) present in a few nanometer scale. Crystallographic information about the nanomaterials such as crystal structure and degree of crystallinity (single crystalline, poly-crystalline or amorphous nature) can be deduced from selected area electron diffraction (SAED) patterns. Moreover, elemental and chemical composition analyses down to sub-nanometer scale can be done using energy dispersive X-ray (EDX) analysis when the TEM is equipped with an X-ray detector.

Fig. 2.7 shows the photograph and a schematic description of the parts of a TEM. TEM works on the principle of optical projection. Electrons emitted from an electron gun by thermionic emission are accelerated to high voltages (typically 100 to 400 kV) and made to impinge on the sample held at a positive potential. The electrons pass through a series of lenses to be focused and scanned across the sample. The sample is placed on a small copper grid a few mm (~3 mm) in diameter. The static electron beam has a diameter of a few microns. Relation between electron wavelength (in Å) and the acceleration voltage (in kV) is

$$\lambda = \frac{12.398}{\sqrt{V * (1022 + V)}} \qquad (2.4)$$

Eqn. 2.4 shows that for an acceleration potential of 200 kV, electron wavelength as low as 0.02508 Å can be obtained. The electron beam has to transmit through the sample without total extinction. This requires that the sample has to be sufficiently thin (a few tens a few hundred nm). This is the main drawback in this technique and many a time, inability to thin the sample sufficiently makes it unsuitable for TEM studies. The transmitted and forward scattered electrons form a diffraction pattern in the back focal plane and a magnified image in the image plane. With additional lenses, either the image or the diffraction pattern is projected onto a fluorescent screen for viewing and/or a digital camera for recording. Improved resolution of the lattice image can be obtained by processing the image using fast Fourier transformation (FFT) using image analysis software (Digital Micrograph, Gatan, USA). HRTEM images of glass and glass-ceramic particles are shown in Fig. 2.8 (a) and (b), respectively. Insets in the figures show the FFT images of a small region to show the atomic positions with high resolution. Total amorphous arrangement of atoms in the glass sample and the presence of lattice fringes in the glass-ceramic sample can be seen.

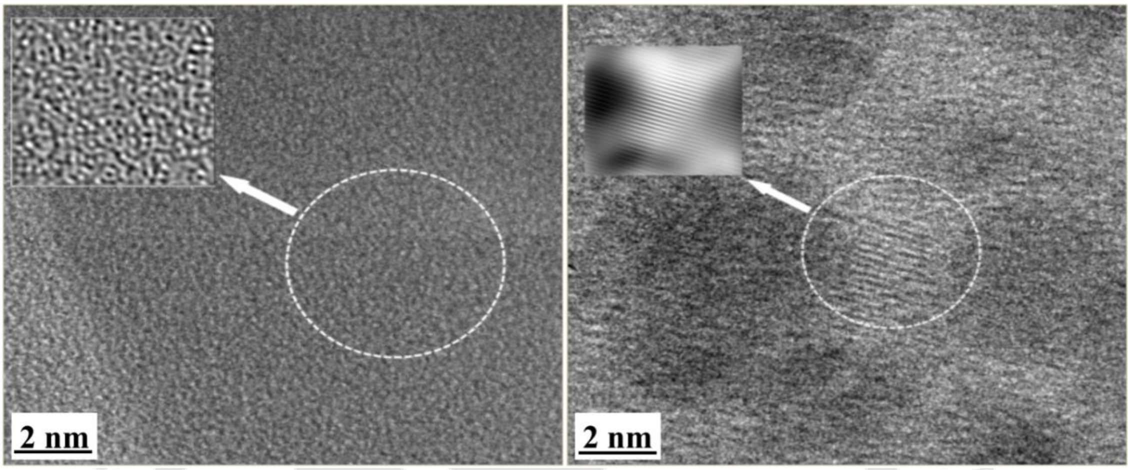

Fig. 2.8: HRTEM image of (a) a glass showing amorphous structure at atomic scale, and (b) glass-ceramic showing embedded crystallites. Insets show FFT images of selected areas.

2.2.1.3 Field emission scanning electron microscopy

FESEM uses a fine beam of electrons to image the surface morphology of materials with high resolution. A photograph of the FESEM (Sigma Zeiss, Germany) used in the present study is shown in Fig. 2.9 along with a schematic which describes its functional parts.

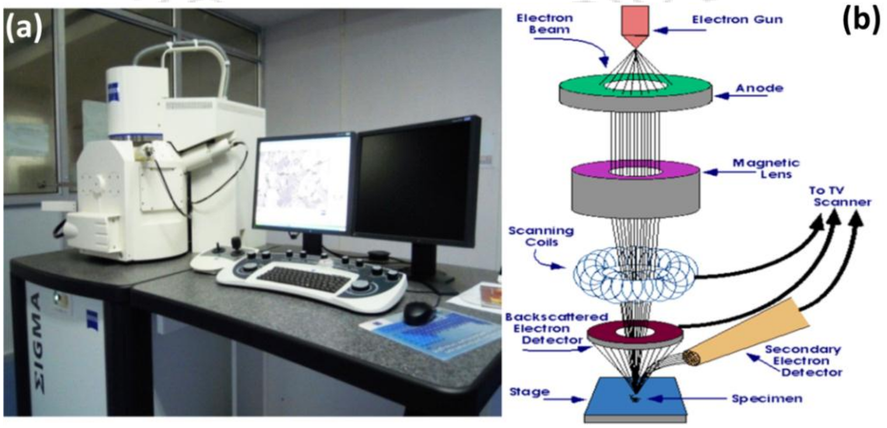

Fig. 2.9: (a) Photograph of the field emission scanning electron microscope (Sigma Zeiss, Germany) and (b) a schematic view of its parts [WEB_PURE].

Indian Institute of Technology Guwahati

In an FESEM, electrons are emitted from a field emission source under ultra-low vacuum. The field emission source is usually tungsten filament (cathode) with a sharp tip which is placed in a large electrical potential gradient. The significance of the extremely thin and sharp tip (~10 - 100 nm) is to concentrate the electric field to an extreme level so that the work function of the material is lowered and electrons can leave the cathode easily. After emission, the electrons are accelerated by an accelerating potential (0.5 - 50 kV) between the cathode and anode. This voltage combined with the beam diameter determines the resolution of the image. As the voltage increases, better point-to-point resolution can be obtained. Because of the smaller size of the electron source, the beam produced by this emitter is about 1000 times smaller than that in a standard scanning electron microscope (SEM), which markedly improves the image resolution. The beam is collimated by electromagnetic condenser lenses, focused by an objective lens and scanned across the surface of the sample by electromagnetic deflection coils. The primary imaging method is by collecting emitted secondary electrons that are released by the sample. A secondary electron detector is placed near to the specimen. By correlating the sample scan position with the resulting signal, an image is formed on the screen that is strikingly similar to what would be seen through an optical microscope. Carbon tape is used as adhesive to stick the sample and to provide it with an electrical conduction path.

Composition of the sample over regions as small as the beam diameter can be obtained by energy dispersive spectrometer (EDS) attachment in a SEM or FESEM. EDS analysis is based on the understanding that when high energy electrons collide with the specimen atom's own electrons, they knock some of them off. A position vacated by an ejected inner shell electron is eventually occupied by a higher-energy electron from an outer shell by emitting an X-ray. The amount of energy released by the transferring electron depends on which shell it is transferring from, as well as which shell it is transferring to. Furthermore, the atom of every element releases X-rays with unique amounts of energy during the transferring process. Thus, by measuring the amounts of energy present in the X-rays being released by a specimen during electron beam bombardment, the identity of the atom from which the X-ray was emitted can be established. The EDS spectrum is just a plot of how frequently an X-ray is received for each energy level. Fig. 2.10 shows a typical EDS spectrum which displays peaks corresponding to the energy levels at which the X-rays were received. Each of these peaks is unique to an atom, and therefore corresponds to a single element. The intensity of the peak is a measure of the concentration of a particular element in the specimen. As EDS analysis provides elementary composition of the system. Empirical formulation of the system can be obtained by taking atomic fraction (or weight fraction) of different elements.

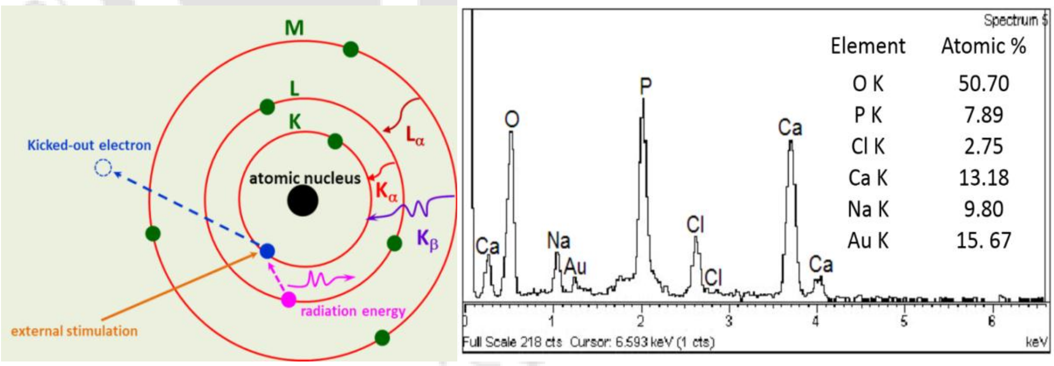

Fig. 2.10: (a) Schematic of X-ray emission by high energy electrons and (b) a typical EDS pattern of a sample with elemental composition map in atomic percentage.

2.2.1.4 Fourier transforms infrared spectroscopy

Infrared spectroscopy is an important technique which provides an easy way to identify the presence of certain functional groups in a molecule. One can also use the unique collection of absorption bands to confirm the identity of a pure compound or to detect the presence of specific impurities. The basic configuration of an FT-IR spectrometer is schematically shown in Fig. 2.11.

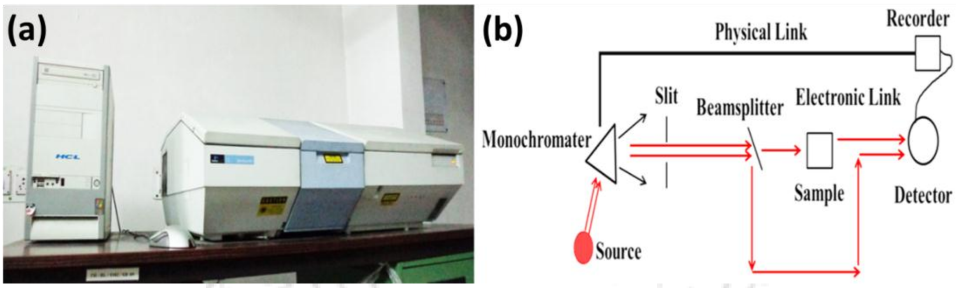

Fig. 2.11: (a) Photograph of PerkinElmer FT-IR spectrometer, and (b) schematic diagram of the instrument.

The essential component of this spectrometer is a Michelson interferometer that consists of a fixed mirror, a moving mirror, and a beam splitter. When the infrared beam coming from a source reaches the beam splitter, it is divided into two halves. Half of the beam is reflected in the beam splitter to the fixed mirror, while the remaining half passes through the beam splitter toward the moving mirror. These two beams are reflected in the fixed and moving mirrors, respectively, and come back to the beam splitter, where they recombine into a new beam that passes through the sample. The sample absorbs all the different wavelengths characteristic of its spectrum, and this subtracts specific wavelengths from the interferogram. The detector now reports variation in energy versus time for all wavelengths simultaneously. A laser beam is superimposed to provide a reference for the instrument operation. Fourier transform spectroscopy uses an infrared beam containing many frequencies and measures how much of that beam is absorbed by the sample. Next, the beam is modified to contain a different combination of frequencies, giving a second data point. This process is repeated many times. A computer takes all these data and works backwards to infer what the absorption is at each wavelength using an algorithm called fast Fourier transform. An FT-IR spectrum is shown below along with a table containing the assignments for the observed peaks in Fig. 2.12. The characteristic absorption peaks correspond to various functional groups present in the specimen.

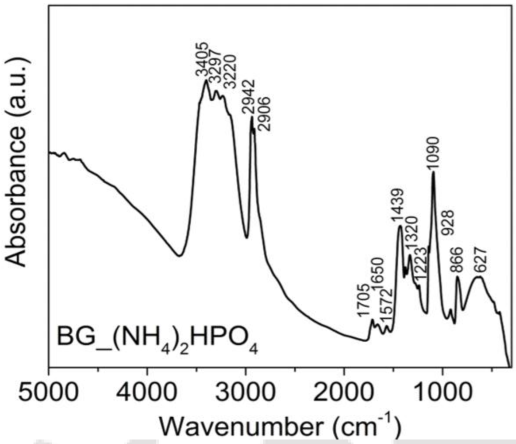

Wavenumber (cm^{-1})	Assignment
Silicate chains	
1090	Si-O-Si antsymmetric stretching (ν_3)
Phosphate chains	
1223, 1320	PO_2 asymmetric stretching
928	$(PO_4)^{3-}$
627	P-O-P symmetric stretching
Network modifiers	
1439	Carbonate group
866	C-O stretching (ν_2)
3405, 3297, 3220	SiOH (Silanol group)
2942, 2906	Hydrogen bonding
1705, 1650,1572	Molecular water

Fig. 2.12: An FT-IR spectrum of a glass along with a table containing the mode assignments for the observed peaks.

2.2.2. Thermal analysis

Thermal properties such as glass transition temperature (T_g), crystallization temperature (T_c) and melting temperature (T_m) can be determined using differential scanning calorimeter (DSC) and differential thermal analysis (DTA) techniques. Differential scanning calorimeter (DSC) is a thermal analysis technique with which the thermal behavior of a sample can be studied over a wide temperature range under isothermal as well as non-isothermal conditions. A commercial DSC (NETZSCH STA) shown in Fig. 2.13(a) was used in the present work. DSC curves were recorded at a constant heating rate of 20 Kminute^{-1} from ambient temperature to 900 °C after baseline correction. This technique was developed by O'Neill and Watson [ESWA64a]. In this technique, the sample and a reference material are maintained at the same temperature with respect to each other by proper application of electrical energy. The heat flow, *dH/dt* to the sample and a reference at the same temperature is recorded as a function of temperature. The reference is an inert material such as alumina or just an empty aluminum sample pan. In non-isothermal measurements, the temperature of the sample and reference are increased or decreased at a constant heating rate.

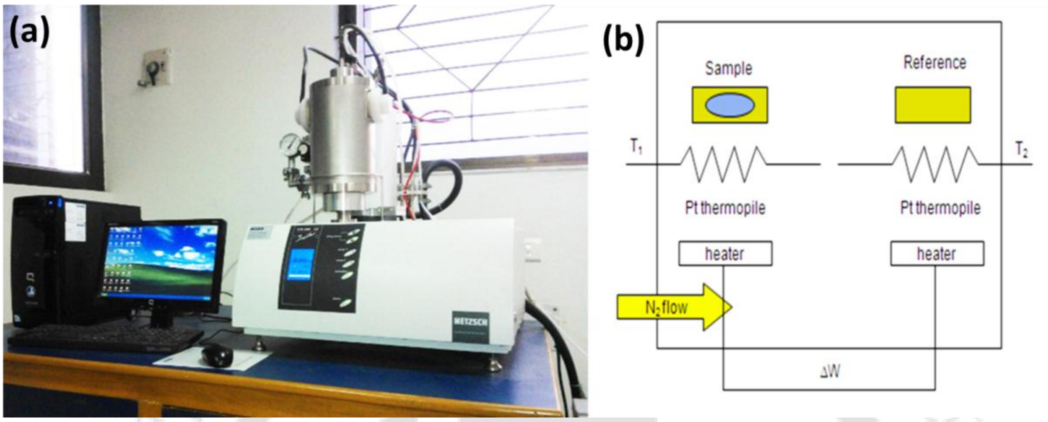

Fig. 2.13: (a) Photograph and (b) schematic diagram NETZSCH STA DSC.

DTA (DTA, Hitachi STA7200) described in Fig. 2.14 was also used in the present studies. The main difference between DTA and DSC is that the latter finds the difference in temperature between a sample and a reference while the heat flow is kept the same. The heat flow through the reference and the sample is maintained throughout the experiment and phase changes and changes in other thermal processes are recorded.

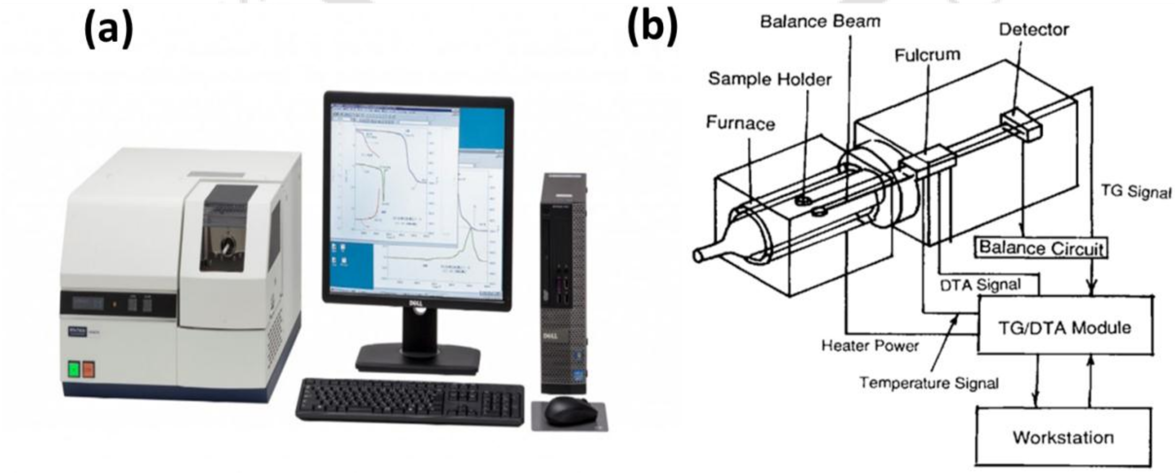

Fig. 2.14: (a) Photograph of DTA (Hitachi STA7200). (b) Schematic diagram of DTA with thermogravimetric (TG) module [WEB_RTIN].

A kinetically controlled reaction temperature such as T_g shifts with heating rate. Once the data on T_g at different heating rates are available, the activation energy, which is a measure of the inhibition to the reaction could be estimated using. Kissinger's equation [FRAC11a],

$$\frac{d\left[\ln \frac{\phi}{T_g^2}\right]}{d\left[\frac{1}{T_g}\right]} = -\frac{E_K}{R} \qquad (2.5)$$

where ϕ is the heating rate, E_K is the activation energy of the reaction and R is the universal gas constant. DTA curves recorded at 5, 10, 15 and 20 K minute^{-1} were used to estimate the activation energy associated with the glass transition using the above relation.

2.2.3 Magnetic characterization

2.2.3.1 Vibrating sample magnetometer

Vibrating Sample Magnetometer (VSM) invented in 1956 by Simon Foner [FONE59a] is widely used for determining the magnetic properties of a large variety of magnetic materials. It has a flexible design and combines high sensitivity with easy of sample mounting and exchange. Measurements of magnetic moments as small as 5 x 10^{-5} emu are possible in magnetic fields from zero to 3 Tesla in a VSM based on an electromagnet. Using a VSM, one can measure the DC magnetic moment as a function of temperature, magnetic field, angle and time. So, it allows performing susceptibility and magnetization studies. A photograph and a block diagram of the VSM are shown in Fig. 2.15. The VSM operates on the principle of Faraday's law of induction, which tells us that a changing magnetic field will produce an electric field [RDCU72a]. This electric field can be measured, which in turn can provide us information about the magnetic moment of the sample as magnetic field and temperature are varied. The VSM normally consists of a water cooled electromagnet and power supply, a vibration exciter and sample holder (with angular position indicator), sensing coils, a Hall probe, an amplifier, the control chassis, a lock-in amplifier, a Gauss meter, and a computer interface. In a VSM, the sample is mounted on the end of a rigid quartz or glass rod attached to a mechanical resonator which oscillates the sample (usually in a vertical direction) at a fixed frequency. Surrounding the sample is a set of sensing coils. As the sample moves, its magnetization alters the magnetic flux through the coils. This produces an AC voltage directly proportional to magnetization, which is amplified and detected using a lock-in amplifier. The external magnetizing field is usually provided by a horizontal electromagnet.

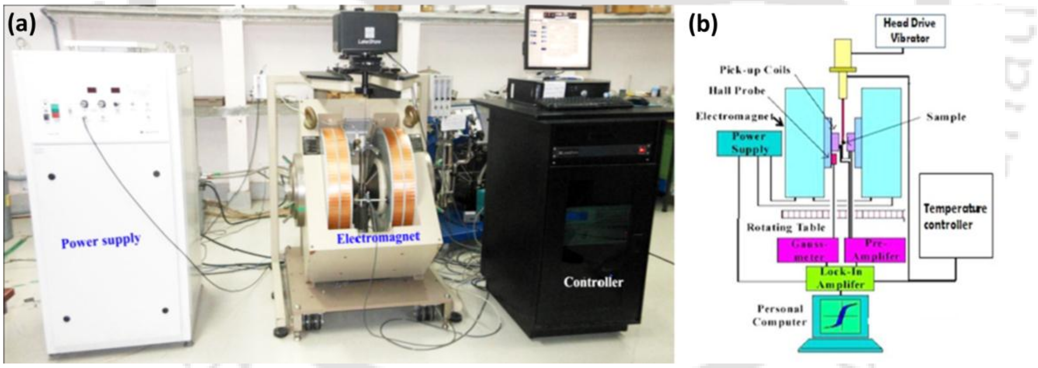

Fig. 2.15: (a) Photograph of Lakeshore VSM Model 7410 and (b) a block diagram of VSM.

The measurement sequence is then programmed using the software provided with the instrument. The vibration exciter is then activated and the signal received from the probe and the pick-up coils is converted into magnetic moment value of the sample. Normally, magnetic field is automatically increased in steps at a constant temperature (*M-H* measurement) by setting the program. VSM is calibrated using a standard reference (high purity nickel sphere), supplied with the instrument. Isothermal (M-H) and themo-magnetization (M-T) obtained using a high temperature sample holder are depicted in Fig. 2.17. Magnetic susceptibility is a useful parameter to characterize magnetic materials. Temperature dependence of the reciprocal of magnetic susceptibility (χ^{-1}) of magnetic materials show a Curie-Weiss type behavior in the paramagnetic regime, i.e.,

$$\chi^{-1} = (T - \theta_P)/C_M \qquad (2.6)$$

where χ is the magnetic susceptibility, C_M is the Curie constant and θ_P is the paramagnetic Curie temperature. θ_P takes positive and negative values for ferromagnetic and ferrimagnetic (and antiferromagnetic) materials, respectively.

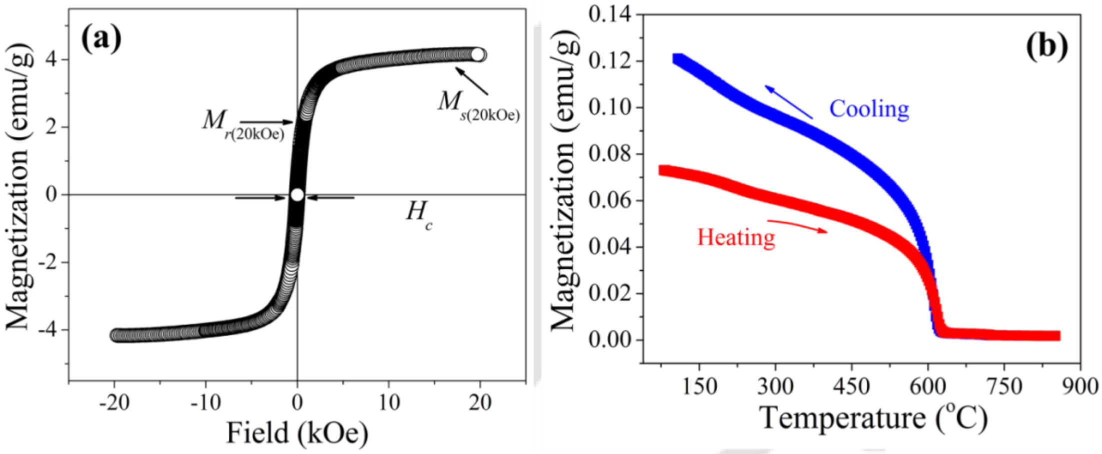

Fig. 2.16: Typical (a) isothermal (M-H) and (b) thermos-magnetization (M-T) curves obtained using a VSM.

A multicomponent magnetic glass-ceramic sample may contain different amounts of magnetic phases with different individual saturation magnetization (M_s) values, say, magnetite (Fe_3O_4, M_s = 92 emu/g) and maghemite (γ-Fe_2O_3, M_s = 74 emu/g) [RDCU72a]. Since the measured saturation magnetization (M_s) of the sample is related to the total amount of magnetic phase(s) present in the sample $M_{s(mph)}$ as,

$$M_{s(mph)} = 100 * [M_s / (x * 92 + y * 72)] \quad (2.7)$$

x and y can be estimated from the XRD data using the procedure described in Fig. 2.6(b).

2.2.3.2 Electron paramagnetic resonance

Room temperature EPR absorption measurements on glasses and glass-ceramics containing iron oxide reveal the nature of interactions between the iron ions apart from providing information on the valance state of iron ions. Every electron has a magnetic moment and spin quantum number $s = 1/2$, with magnetic components $m_s = \pm 1/2$. When an external magnetic field of strength B_0 is applied, the electron's magnetic moment aligns itself either parallel ($m_s = -1/2$) or antiparallel ($m_s = +1/2$) to the field. Parallel alignment corresponds to the lower energy state and separation between it and the upper state is $\Delta E = g_e \mu_B B_0$, where g_e is the electron's so-called g-factor and μ_B is the Bohr magneton. An unpaired electron can move between the two energy levels by either absorbing or emitting electromagnetic radiation of energy $\varepsilon = hv$ such that the resonance condition $\varepsilon = \Delta E$ is obeyed. This leads to the fundamental equation of EPR spectroscopy, *viz.*

$$hv = g_e \mu_B B_0 \quad (2.8)$$

Though this equation permits a large combination of frequency and magnetic field values, EPR measurements are mostly made with microwaves in 9–10 GHz region and magnetic fields up to ~0.8 T. EPR spectra can be generated by either varying the magnetic field while holding the incident microwave frequency fixed. A collection of paramagnetic centers, such as free radicals, is exposed to microwaves at a fixed frequency. By increasing an external magnetic field, the gap between the $m_S = +1/2$ and $m_S = -1/2$ energy states is widened until it matches the energy of the microwaves. At this point, the unpaired electrons can move between their two spin states. Since there are more electrons in the lower state due to the Maxwell-Boltzmann distribution, there is a net absorption of energy and it is this absorption which is monitored and converted into a spectrum. It has become a common practice to record and publish first derivative EPR absorption spectra rather than the raw spectra.

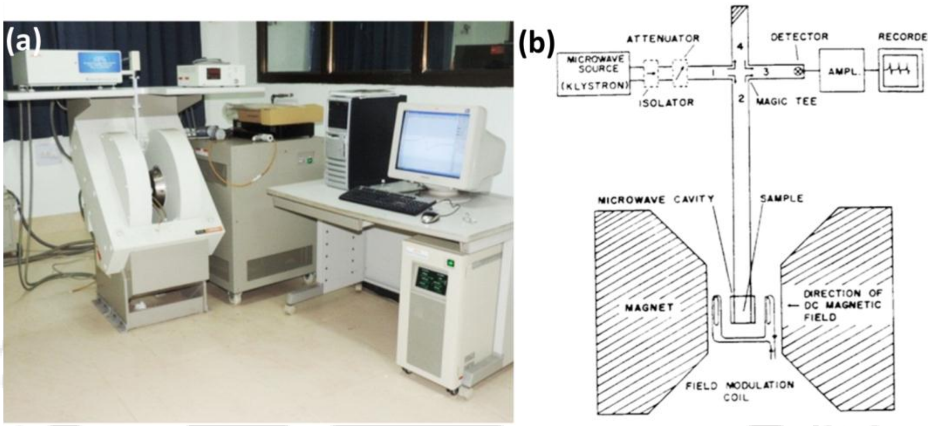

Fig. 2.17: (a) Photograph and (b) block diagram of EPR spectrometer (JEOL JES-FA200).

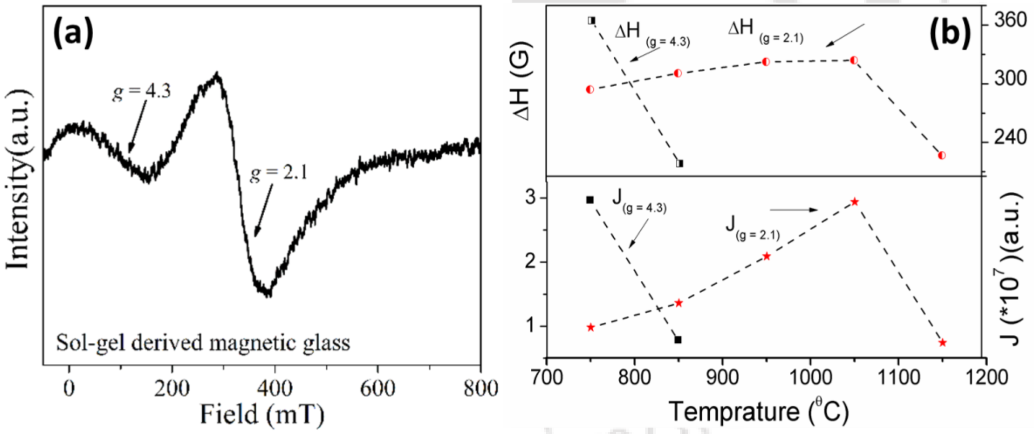

Fig. 2.18: (a) EPR spectrum exhibiting two resonances. (b) line intensity *J* and linewidth Δ*H* of g ≈ 4.3 and g ≈ 2.1 absorption lines of a glass heat treated at different temperatures.

EPR absorption spectra of glasses and glass-ceramics in powder form were obtained using a JEOL Spectrometer (model JES-FA200) operating at X-band frequency (ν = 9.4 GHz) with 100 kHz field modulation at room temperature (*cf*. Fig. 2.17). The EPR spectrometer was calibrated with in-built software which uses EPR spectrum of Mn^{2+} ions in MgO as standard reference. The magnetic field was scanned from 0 to 800 mT and microwave power was set at 1 mW. Powdered glass or glass-ceramics specimen weighing ~30 mg was taken in a quartz tube for the EPR measurements. EPR absorption in iron oxide glass system at $g \approx 4.3$ is characteristic of isolated Fe^{3+} ($3d^5$, $^6S_{5/2}$) ions predominantly situated in different sites and the one at $g \approx 2.1$ is attributed to those ions which interact by superexchange coupling. Fig. 2.18(a) shows the EPR spcctrum recorded for a glass sample containing iron oxide. Fe^{2+} ions are not involved in EPR absorption but their interaction with Fe^{3+} ions influences the characteristics of the absorption lines. EPR parameters, *viz.*, absorption line intensity (J) can be estimated from peak to peak height (I) and linewidth (ΔH) of the EPR absorption profiles of the specimens using the relation $J = I(\Delta H)^2$. Fig. 2.18(b) shows the variation of the EPR parameters corresponding to the two resonance absorption lines of a glass sample heat treated at different temperatures. The changes occurring in the local environment about the Fe^{3+} ions in the glass heat treated at different temperatures can be inferred from this plot.

2.2.4 Mechanical testing of electrospun membranes

Mechanical testing was performed to check the tensile properties of electrospun nanofibrous membranes. Electrospun fibrous membranes are mostly hyperelastic and they differ from linear elastic materials. The mechanical tests were performed using a microtensile testing machine (Deben Microtest) equipped with a calibrated 200 N load cell depicted in Fig. 2.19(a). The test samples were rectangular in shape with an area of cross section of 24×27 mm^2 and thickness ranging from 0.87 - 0.98 mm. The specimen was stretched and firmly clamped between the grips of the tensile testing machine. A gradually increasing tensile force (in N or lb) was applied on the material at a slow but constant speed until rupture occurs. The amount of deformation (extension) was then measured by an extensometer. The applied tensile force (stress) and the extension (strain) were simultaneously recorded during the experiment. Finally, a stress-strain curve similar to the one shown in Fig. 2.19(b) was plotted to evaluate the tensile properties. Tensile testing was conducted under the same conditions for various materials which provided a direct comparison of the tensile properties of different polymeric membranes.

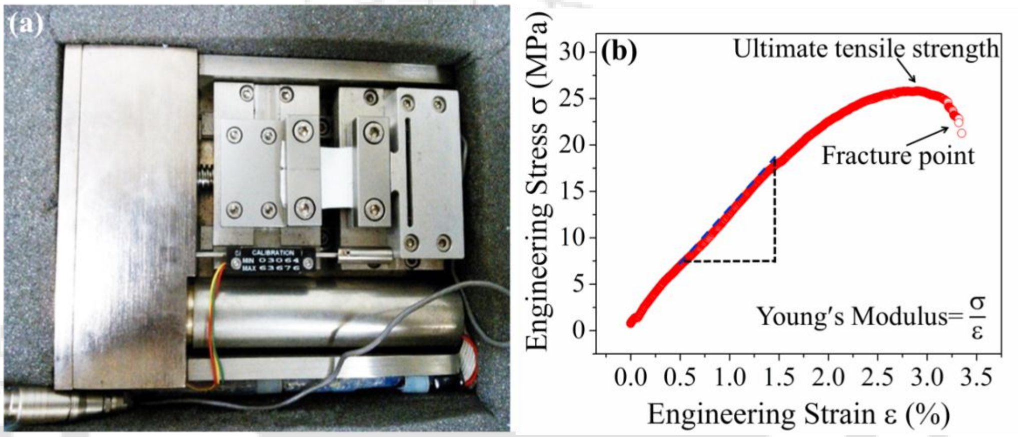

Fig. 2.19: (a) A photograph of Deben Microtest unit and (b) a typical stress-strain curve of polymer membrane showing various tensile parameters.

2.2.5 Bioactivity tests

A bioactive implant material is expected to evoke the same response as bone in physiological condition, *i.e.*, induce formation of a hydroxyapatite (HA) surface layer. Before testing the response of a bioactive material in an animal model, it is mandatory that *in vitro* tests qualify the material for *in vivo* tests. Kukubo and his colleagues [KOKU06a] developed a modified acellular simulated body fluid (SBF) which has inorganic ion concentrations similar to those of human blood plasma (HBP) (*cf.* Table 2.2). The ion concentrations of SBF are given on Table 2.3. Interestingly, it has been shown that *in vitro* tests performed using the modified SBF exactly mimic the *in vivo* results [HENC82a, KOKU06a]. Since SBF is supersaturated with respect to apatite, an inappropriate preparation method can lead to the precipitation of apatite in the solution.

Table. 2.2: Nominal ion concentrations of SBF in comparison with those in HBP.

Ion (mM)	Na^+	K^+	Mg^{2+}	Ca^{2+}	Cl^-	HCO^{3-}	HPO_4^{2-}	SO_4^{2-}
SBF	142	5	1.5	2.5	147.8	4.2	1	0.5
HBP	142	5	1.5	2.5	103	27	1	0.5

2.2.5.1 Preparation of SBF and *in vitro* test

In order to prepare 1000 ml of SBF, 700 ml of ion-exchanged and distilled water was taken in a 1000 ml plastic beaker. Water in the beaker was heated to 37 ± 0.5 °C under constant stirring. The reagent numbers 1 to 8 were dissolved in the solution at 37 ± 0.5 °C one by one in the order given in Table 2.3. The 9th (Tris) and 10th reagents were then added for pH adjustment in a careful and methodical manner to maintain a pH value of 7.40. Additional water was then added to make up the solution to 1000 ml. The prepared SBF was then preserved in dark coloured plastic bottles with a tightly placed lid and stored at 5−10 °C in a refrigerator. The SBF stock so preserved was used for a maximum period of 30 days.

Table 2.3: Order, amounts, weighing containers, purities and formula weights of reagents required for preparing 1000 ml of SBF.

Reagent	Amount	Container	Purity (%)	Formula weight
NaCl	8.035 g	Weighing paper	99.5	58.4430
$NaHCO_3$	0.355 g	Weighing paper	99.5	84.0068
KCl	0.225 g	Weighing bottle	99.5	74.5515
$K_2HPO_4.3H_2O$	0.231 g	Weighing bottle	99.0	228.2220
$MgCl_2.6H_2O$	0.311 g	Weighing bottle	98.0	203.3034
1.0M HCl	39 ml	Graduated cylinder	—	—
$CaCl_2$	0.292 g	Weighing bottle	95.0	110.9848

Indian Institute of Technology Guwahati

Na_2SO_4	0.072 g	Weighing bottle	99.0	142.0428
Tris buffer	6.118 g	Weighing paper	99.0	121.1356
1.0M HCl	0–5 ml	Syringe	—	—

Glass-ceramics pieces to be tested *in vitro* were polished with 2000 grit silicon carbide paper and shaped to dimensions of 10 × 10 × 2 mm^3. Polished specimens were cleaned with acetone in an ultrasonicator. *In vitro* bioactivity test was carried out by soaking the glass-ceramics pieces in 30 ml of SBF. The temperature of the solution was maintained at 37 °C. Specimens immersed in SBF were taken out after 1, 3, 5, 10 and 15 days, gently washed with acetone and dried in a sterile environment. The surface of SBF treated samples were examined using GI-XRD, FESEM, EDS and pH. Powders of sol-gel derived glass and glass-ceramic specimen were cold compacted into pellets of 10 mm diameter in a hydraulic press under a pressure of 6 Ton/cm^2 and the pellets were gently polished to yield a smooth surface before immersing in SBF.

pH variation of SBF solution plays a crucial role in deciding the bioactive nature of the specimen. Hence, pH variation during *in vitro* test was monitored with a calibrated pH meter (EUTECH pH Tutor). Electrodes of pH meter were gently dipped into 3-4 different zones of the beaker containing SBF solution without disturbing the surface of specimen. pH data was recorded with a precision ± 0.01 and the average value of pH was calculated.

2.2.5.2 Water uptake and degradation of electrospun membranes

Degree of swelling of a membrane placed in an aqueous medium could be described as moisture absorptivity of the membrane. SBF was chosen as the aqueous medium for this study since it mimics HBF in its acellular content. In order to provide an appropriate physiological environment, pH of SBF was adjusted to 7.40 and the test environment was maintained at 37 °C. 10 mm discs of electrospun membranes were weighed and placed in 24 well plates containing 2-3 ml of SBF at 37 °C for 3 days. Weight of swollen membranes was measured at specific time intervals (*viz.*, 12, 24, 36, 48, 60 and 72 h). Swollen fiber membranes were wiped with tissue paper and immediately weighted and percentage of swelling of the fiber membranes was determined using the relation,

$$\text{Degree of swelling (\%)} = (W_s - W_d) / W_d \times 100 \qquad (2.9)$$

where W_s and W_d are the weights of swollen and dried membranes, respectively.

In order to evaluate the degradation of these membranes *in vitro*, triplicate specimens of each membrane were cut into circles of 10 mm diameter and immersed in 24-well plates containing 2-3 ml of SBF maintained at 37 °C. SBF treated specimens were taken out from the medium at specified time intervals spread over 10 days and dried in a hot air oven maintained at 37 °C for 24 h to ensure complete drying. The weight loss was determined gravimetrically by comparing the dry weight remaining at a specific time with the initial weight. Percentage of degradation was determined from the weight loss using the relation,

$$\text{Weight loss (\%)} = ((W_i - W_d) / Wi) \times 100 \qquad (2.10)$$

where W_i is the initial dry weight of sample and W_d is the dry weight of sample immersed in SBF for a certain time period.

2.2.6 Cellular viability and antimicrobial analysis of membranes

2.2.6.1 Cell culture and alamarBlue cell proliferation assay

All cell culture procedures were performed to a standard that will prevent contamination from bacteria, fungi and cross contamination with other cell lines. Aseptic environment was ensured by

a) sanitizing the cabinet using 70% ethanol before commencing work,

b) sanitizing gloves by washing them in 70% ethanol and allowing to air dry for 30 seconds before commencing work, and

c) placing all materials and equipment inside the cabinet prior to starting work after sanitizing the exterior surfaces with 70% ethanol.

All media, supplements and reagents were sterilized to prevent microbial growth in the cell culture. Most cell lines were grown using Dulbecco's modified eagle medium (DMEM, Gibco, USA) culture media. L929 murine fibroblast cells were cultured in DMEM supplemented with 10 % fetal bovine serum (FBS, Gibco, USA) and antibiotics (penicillin and streptomycin). Similarly, HaCaT human keratinocyte cells were cultured in DMEM/F12 (Gibco, USA) supplemented with 10 % FBS and antibiotics. The cell lines were maintained at 37 ºC in an incubator with 5 % CO_2 and the media was replenished after every 3 days. For cell proliferation studies, membranes were pre-sterilized in a laminar hood with 70 % v/v ethanol for 3 h followed by thorough washing with sterile phosphated buffered saline (PBS, pH 7.4) to remove residual alcohol. All membranes were pre-conditioned overnight in complete DMEM. L929 fibroblasts and HaCaT human keratinocytes were seeded on sterilized membrane circles (diameter = 10 mm) at a density of 5×10^4 cells/membrane.

Cell proliferation study was performed with alamarBlue which is a non-toxic dye that does not affect the viability or proliferation of the cells. Proliferation rate was determined for the same batch of culture at different time points. AlamarBlue assay was carried out for 1, 4 and 7 days following manufacturer's protocol. Briefly, cells were incubated in medium supplemented with 10% (v/v) alamarBlue dye (Invitrogen, USA) for 3 h. After incubation, 100 µl of solution from each sample was read at 570/600 nm in a multi-plate reader (Tecan infinite M 200). Non-seeded wells containing only the membranes were supplemented with 10% alamarBlue dye and used as a negative control. AlamarBlue® is a cell viability assay reagent which contains the cell permeable, non-toxic and weakly fluorescent blue indicator dye called resazurin. Resazurin is used as an oxidation-reduction (REDOX) indicator that undergoes colorimetric change in response to cellular metabolic reduction (*cf*. Fig. 2.20 (a)). The reduced form of resorufin is pink and highly fluorescent, and the intensity of fluorescence produced is proportional to the number of living cells respiring (*cf*. Fig. 2.20 (b)). Through detecting the level of oxidation during respiration, alamarBlue® acts as a direct indicator to quantitatively measure cell viability and cytotoxicity. % Reduction of alamarBlue is calculated using the formula,

$$\%\ \text{Reduction of alamarBlue} = [(O_2{*}A_1)-(O_1{*}A_2)/((R_1{*}N_2)-(R_2{*}N_1)]{*}100 \tag{2.11}$$

where, O_1 = molar absorption coefficient (E) of oxidized alamarBlue (Blue) at 570 nm, O_2 = E of oxidized alamarBlue at 600 nm, R_1= E of reduced alamarBlue (Red) at 570 nm, R_2 = E of reduced alamarBlue at 600 nm, A_1 = absorbance of test wells at 570 nm, A_2 = absorbance of test wells at 600 nm, N_1 = absorbance of control well (media plus alamarBlue but no cells) at 570 nm and N_2 = absorbance of control well (media plus alamarBlue but no cells) at 600 nm.

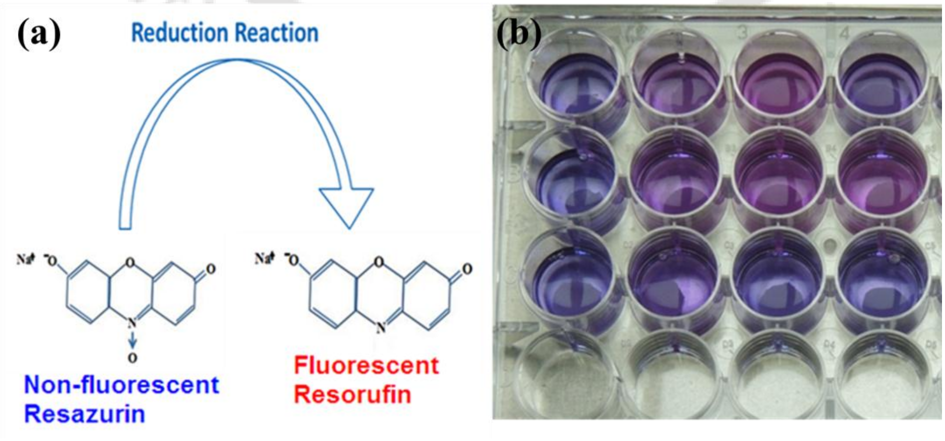

Fig. 2.20: (a) Resazurin to resorufin conversion reaction. (b) AlamarBlue assay showing cell proliferation activity on PVA/PVP e-spun scaffolds seeded with L929 cells.

Viability and adherence of the bone specific MG-63 osteosarcoma cells seeded on all the PVA-bioglasses composites membrane variants were investigated with fluorescent imaging after 7 days of culture. Cell-seeded membranes (10^4 cells/membrane) were rinsed with sterilized (Phosphate-buffered saline, PBS pH 7.40) and incubated in live/dead assay solution containing calcein AM (4 µM) and ethidium homodimer-1 (2 µM) (EthD-1, Sigma-Aldrich, USA). Membranes were incubated for 15-20 minutes in a humidified incubator. Excess dye was washed off incubated specimens using PBS (pH 7.40) and cells were observed under inverted fluorescence microscope (EVOS FL, Life Technologies, USA). Live cells were detected by green fluorescence of calcein and dead cells by red fluorescence produced by EthD-1.

2.2.6.2 Live/Dead assay for cellular viability

The viability and adherence of cells on all variants of membranes were tested by live/dead assay. Live and dead cells were stained with calcein AM (4 mM) and EthD-1 (2 mM), respectively. Briefly, cells seeded on membranes (5×10^4 cells/membrane) and cultured for 7 days were washed with PBS (pH =7.4) and incubated in live/dead solution for 20 minutes in a humidified incubator at 37 ºC. Excess dye was washed off using PBS and the cells were observed under inverted florescent microscope.

2.2.6.3 Antibiotic release and antimicrobial studies

Antibiotic release from membranes was investigated using ciprofloxacin hydrochloride monohydrate (Himedia, India, MW 385.82 Da). Ciprofloxacin hydrochloride monohydrate 50 µl of concentrated (10 mg/ml) antibiotic solution was completely adsorbed onto each membrane separately. Antibiotic-loaded membranes were further dried in a laminar hood for 2 h and immersed in 10 ml of PBS (pH 7.4) as release medium. At pre-specified time points (*viz.*, 0.5, 1, 2, 4, 9 and 14 days), the antibiotic releasate was taken out and analyzed spectrophotometrically using a multi-plate reader at a wavelength of 270 nm. The releasate was added back to the same falcon and re-incubated until the next time point. Total antibiotic released in each membrane was analyzed separately and quantified from the standard curve.

Antibiotic release study from membranes and their effect on microbial growth inhibition was analyzed using ciprofloxacin hydrochloride monohydrate. This study was executed with gram positive *Staphylococcus aureus (S. aureus)* obtained from Microbial Type Cell Culture Collection and Gene Bank (MTCC, IMTECH, India). For zone inhibition assay, 50 µl of concentrated antibiotic solution (10 mg/ml) was adsorbed onto each membrane circle (diameter =10 mm) separately. Antibiotic-loaded membranes were further dried in a laminar hood for 2 h.

For microbial culture, Luria Bertani broth (Himedia, India) containing 10 g tryptone, 5 g yeast extract, and 10 g sodium chloride per liter was prepared as per manufacturer's protocol. The broth was inoculated with fresh culture of *S. aureus* and was kept in shaker incubator at 37 °C. Luria Bertani agar (Himedia, India) containing 10 g tryptone, 5 g yeast extract, 10 g sodium chloride, and 15 g agar/l was used for culture plate preparation. Luria Bertani agar was autoclaved and plates were prepared by pour plating method and kept overnight at 37 °C to check for undesirable microbial contamination. After ensuring that the plates are contaminant free, they were uniformly spread with 200 µl microbial culture aliquot (OD = 0.8 at 600 nm). The drug inoculated membranes were placed over agar plate and kept overnight in an incubator at 37 °C. The diameter of the zone of inhibition was calculated using ImageJ^{TM} software.

2.2.6.4. Alkaline phosphatase enzyme activity

Alkaline phosphatase enzyme is a hallmark quantitative marker for osteogenic differentiation. Alkaline phosphatase (ALP) enzyme activity of cultured cells was assessed using ALP assay kit (Abcam, USA) following manufacture′s protocol. The kit works on the principle of converting *p*-nitrophenyl phosphate (*p*NPP) to *p*-nitrophenol (*p*NP) and detecting the end product at λ_{max} = 405 nm using a spectrophotometer. In practice, membranes cultured for 7 days were washed with PBS and cells were harvested from all the membranes using trypsin/EDTA. Cells were subsequently washed with cold PBS and centrifuged. After centrifugation, cells were lysed using lysis solution (0.2 % (v/v) Triton X-100 and 5mM $MgCl_2$). Further, the lysate was centrifuged at 12,000 rpm and 4 ^{o}C. Supernatant was then collected and its ALP activity was measured. ALP content in cell culture media was also measured and the cumulative ALP activity was calculated. Sample readings were extrapolated from the standard curve and plotted using the relation,

$$A = [(\text{Corrected absorbance} - \text{y-intercept})/\text{Slope}] \qquad (2.12)$$

ALP concentration in the samples was calculated as

$$\text{ALP activity (U/ml)} = (A/V)/t \qquad (2.13)$$

where *A* is the amount of pNP generated by the sample (in micromol), *V* is volume of the sample added in the assay well (in mL) and *t* is the reaction time (in minutes). ALP activity values obtained were normalized with percentage of alamarBlue reduced and plotted.

2.2.6.5 Statistical analysis

All data are reported as mean along with standard deviation. For each experiment, n= 4 samples were used. Statistical analysis was performed by one-way analysis of variance (ANOVA). All statistical analyses were executed using Microcal OriginPro 8.

Differences between groups of threshold significant level $p \leq 0.05$ were considered statistically significant and values with $p \leq 0.01$ as highly significant.

TH-1620_10612107

Chapter 3

Investigations on bulk magnetic bioglass-ceramics

This chapter presents investigations carried out on two bulk bioactive glass-ceramic systems containing bone mineral and magnetic phases.

3.1 Bulk $41CaO.44SiO_2.4P_2O_5.8Fe_2O_3.3Na_2O$ glass-ceramics

It was pointed out in the first chapter of this thesis that heat treatment of SiO_2-CaO-P_2O_5 glasses containing iron oxide yields ferrimagnetic bioactive glass-ceramics, which have been proposed as thermos-seeds for hyperthermia treatment of cancer [OHUR04a, RKSI08a, RKSI08b, RKSI08c, RKSI09a, QIUH15a]. During heat treatment at elevated temperature inside a closed electric furnace, Fe_2O_3 in the nonmagnetic glasses crystallized in the reduced oxide state as ferrimagnetic magnetite (Fe_3O_4) along with bone mineral phase(s). The induction heat generated by such a ferrimagnetic thermos-seed subjected to an alternating magnetic field of frequency f is a product of f and the magnetic hysteresis loop area [KAWA08a]. In order to improve the efficiency of the thermos-seed either the amount of magnetic phase in the glass-ceramic has to be increased or a stronger magnetic material has to be used. Let us first explore the ways of increasing the amount of iron oxide phase in the glass-ceramic. One cannot arbitrarily increase the amount of iron oxide as this may adversely affect the bioactivity of the system [OHUR04a]. It has been pointed out that substituting up to 8 wt.% Fe_2O_3 for SiO_2 in 45S5 bioglass does not affect the excellent bioactivity of the system

[RKSI08b, RKSI08c]. Since one can control the amount of iron oxide present in the glass-ceramic by tailoring the heat treatment temperature and time, there is a possibility to optimize this ferrimagnetic glass-ceramic system for deriving efficient thermo-seeds. Though a number of studies reveal the potential of bioactive glass-ceramics containing iron oxide for use as thermos-seeds, no attempt has been made so far to obtain optimized thermo-seeds in this complex multiphase system. This section explores the structural, magnetic and *in vitro* bioactivity of $41CaO.44SiO_2.4P_2O_5.8Fe_2O_3.3Na_2O$ (mole %) glasses subjected to a systematic heat treatment.

3.1.1 Preparation

Glass with a composition (in mole %) of $41CaO44SiO_2$ $4P_2O_58Fe_2O_33Na_2O$ was first prepared by melt quenching method described in detail in section 2.1.1. Briefly, appropriate amounts of the starting high purity compounds SiO_2, Fe_2O_3, Na_2CO_3, $CaCO_3$ and $NH_4(H_2PO_4)$ were taken in a platinum crucible, calcined at 800 °C in air before melting the charge at 1550 °C. The melt was then poured between two copper plates at room temperature to form glass. T_g of as-quenched glass was determined to be 621 °C from DSC curve recorded at constant heating rate of 20 °C/minute. So, as-quenched glass pieces were heat treated at different temperatures (T_A) ranging from 750 to 1150 °C for different time periods (t_A) ranging from 1 h to 3 h in air to form glass-ceramics.

3.1.2 Structural characterization

Powder X-ray diffraction technique described in section 2.2.1.1 was used to identify and quantify the phases crystallized in the heat treated glasses. Fig. 3.1 shows the XRD patterns of glass heat treated at 750 °C and 1150 °C at three different t_A. The XRD patterns show the evolution of various crystalline phases with annealing time. Phase identification was carried out using ICDD diffraction data given in Table 2.1. XRD patterns of glass heat treated at 750 °C indicate the initiation of devitrification process as t_A is increased from 1 to 3 h. The XRD patterns confirm the presence of three major crystalline phases in the samples, two bone mineral phases *viz.*, hydroxyapatite [$Ca_{10}(PO_4)_6(OH)_2$] and wollastonite [$CaSiO_3$], and one magnetic phase, *viz.*, magnetite [Fe_3O_4] as the major crystalline phases in both the samples. α-hematite (α-Fe_2O_3) appears as an additional phase in the XRD pattern of the glass heat treated at 1150 °C.

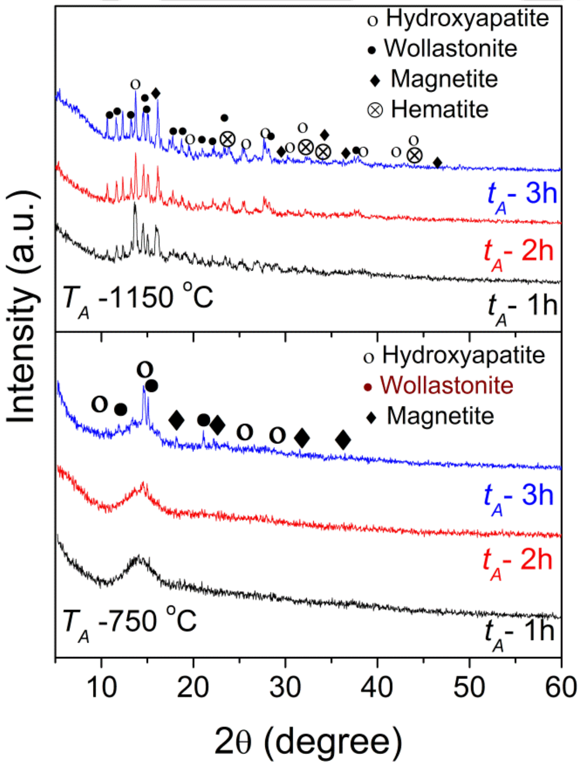

Fig. 3.1: XRD patterns of glass heat treated at different temperatures and time periods.

Presence of bone mineral phases confirms the biocompatible nature of the glass ceramics. Lack of any intense peak in the XRD pattern of glass annealed at 750 °C shows that nucleation and growth of phases has just been initiated at this temperature. Average crystallite size (d_{av}) of different nanocrystalline phases crystallized at temperature above 750 °C was estimated using Eq. 2.2 and given in Table 3.1. d_{av} and ε of the three nanocrystalline phases increase with increase in T_A and t_A.

3.1.3 Magnetic characterization

Fig. 3.2 shows the isothermal magnetization (M - H) curves obtained for the heat treated glasses at three T_A's. All the samples exhibit magnetic hysteresis. However, the shape of the hysteresis loops and the saturation magnetization (M_s) of the samples did not follow a systematic pattern as pointed out by Fig. 3.2. The high magnetization exhibited by glass heat treated at 1050 °C is clearly evident.

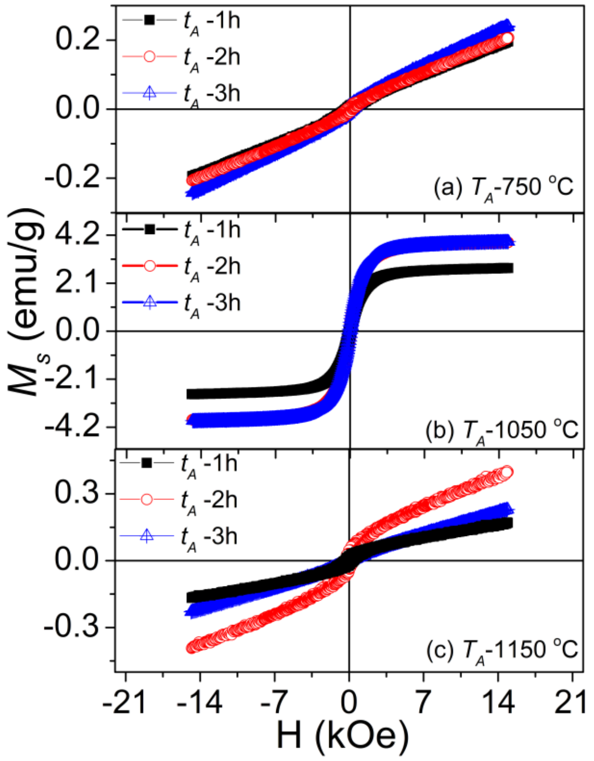

Fig. 3.2: VSM curves of glass annealed at 750 °C, 1050 °C and 1150 °C for different time periods.

Variation of d_{av} of magnetite as a function of T_A and t_A is shown in Fig 3.3. Fig. 3.3 depicts a gentle increase in d_{av} of magnetite up to 1050 °C and a sharp increase beyond this T_A for all t_A. Upon heat treatment at higher T_A, the amount as well as the crystallite size of magnetite increases, resulting in the observed increase in magnetic moment and decrease in coercivity.

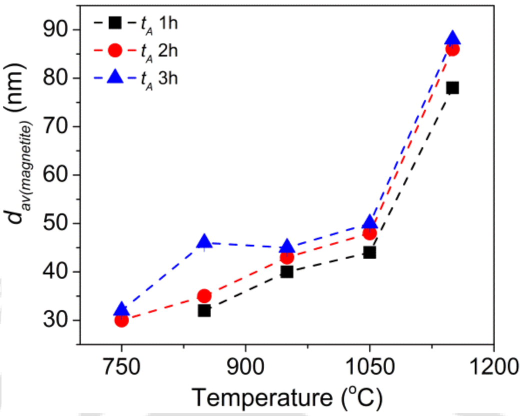

Fig. 3.3: Variation of magnetite crystallite size, $d_{av(magnetite)}$ as a function of annealing parameters T_A ans t_A.

The variation of saturation magnetization (M_s) of the glass with heat treatment conditions is illustrated in Fig. 3.4. Though M_s shows an increase with heat treatment temperature and time, the dramatic increase to 5.15 emu/g for 2 h heat treatment at 1050 °C is strikingly visible from the figure. The reason for the highest M_s is due to the highest amount of magnetite phase present in this sample.

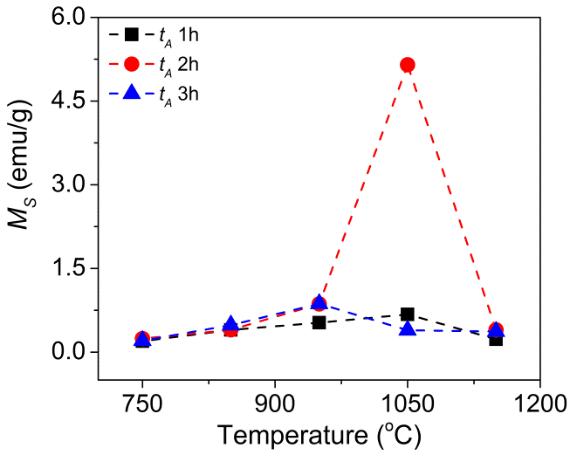

Fig. 3.4: Variation of saturation magnetization (M_s) as a function of annealing parameters T_A ans t_A .

Fig. 3.5 shows that the coercivity (H_c) of magnetite crystallites in the glassy matrix exhibits a random variation. This behavior of H_c can be explained as follows: At low T_A, nucleation and crystallization of magnetite crystallites occur in a randomly distributed manner in the glassy matrix resulting in weak magnetic interaction. H_c is influenced in a significant way by the crystal dimensions. Degree of ordering of the magnetic moment in individual particles of Fe_3O_4 increases with increasing d_{av}, especially for $d_{av} < 50$ nm, due to the formation of single domain particles. Hence, decrease in H_c for magnetite crystallites with d_{av} between 48 nm and 15 nm is due to the increase in the number of magnetic domains in the individual particles with increasing crystallite size [TACA04a]. For $T_A > 1050$ °C, partial conversion of ferrimagnetic Fe_3O_4 into nonmagnetic hematite (α-Fe_2O_3) occurs, leading to an increase in H_c and decrease in M_s [KAWA04a].

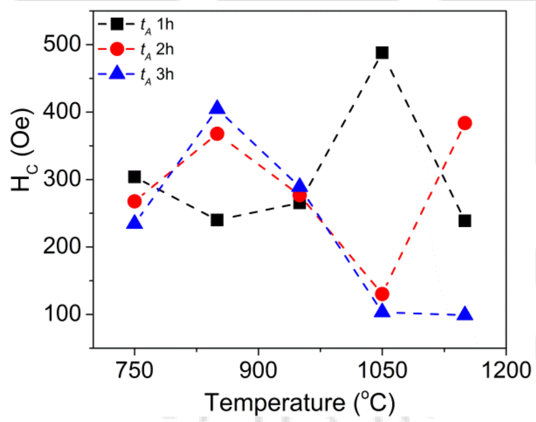

Fig. 3.5: Variation of coercivity as a function of annealing parameters T_A and t_A.

Hysteresis loop area depends on both saturation magnetization and coercive field. The glass heat treated at 1050 °C for 2 h shows the maximum loop area of 1026 erg/g for ±20 kOe field sweep as shown in Fig. 3.6.

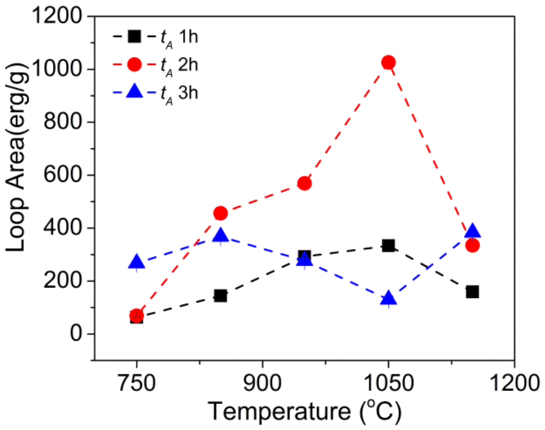

Fig. 3.6: Variation of loop area as a function of annealing parameters T_A ans t_A .

Total magnetic phases and percentage of Fe_3O_4 and α-Fe_2O_3 phases in glass heat treated at different conditions was estimated using this procedure discussed in section 2.2.1.1 and the data obtained are tabulated in Table 3.2. Amount of Fe_3O_4 phase increases in glass heat treated up to 1050 °C in accordance with the XRD results portrayed in Fig. 3.1 and also accounts for the increase in M_s of the glass-ceramic samples. The decrease in the percentage of Fe_3O_4 phase and in turn M_s upon prolonged treatment at 1150 °C is a consequence of the formation of weakly ferromagnetic hematite (α-Fe_2O_3). As pointed out earlier, the highest amount of Fe_3O_4 present in samples heat treated at 1050 °C for 2 h is the reason for the highest M_s recorded at this heat treatment condition. The deterioration in M_s on prolonged heat treatment (*i.e.*, for t_A > 2 h) can be attributed to the increased oxidation of Fe_3O_4 into α-Fe_2O_3. A phase fraction of ~9 % of α-Fe_2O_3 is estimated in samples heat treated at 1150 °C for 3 h. Thus, the deterioration in M_s of glass heat treated at 1050 °C for more than 2 h and at 1150 C is due to the reduction in amount of magnetite and the conversion of magnetite into weakly magnetic hematite phase. Thus, heat treatment of $41CaO44SiO_2 4P_2O_5 8Fe_2O_3 3Na_2O$ glass at 1050 °C for 2h yields the best thermos-seeds.

Table 3.1: Average crystallite size (d_{av}) of Magnetite, hydroxyapatite and wollastonite crystallites glass heat treated at different T_A and t_A.

T_A (°C)	750 °C			850 °C			950 °C			1050 °C			1150 °C		
t_A (Hour)	1h	2h	3h	1h	2h	3h	1h	2h	3h	1h	2h	3h	1h	2h	3h
d_{av} (nm)/% ε (×10^{-4}) (a.u.) **Magnetite**	15	30/13	32/25	18/ 13	35/18	32/29	20/ 14	43/ 19	46/30	48/17	48/ 19	50/30	96/ 40	86/ 45	88/50
d_{av} (nm)/% ε (×10^{-4}) (a.u.) **Hydroxyapatite**	11	11/7	20/8	15 / 7	21/10	29/20	35 / 14	39/20	41/30	38/ 17	46/32	55/34	42/ 32	49/37	55/42
d_{av} (nm)/% ε (×10^{-4}) (a.u.) **Wollastonite**	11	12/9	17/9	17/12	21/12	26/19	23/15	32/18	42/22	32/15	36/33	42/34	45/29	48/31	51/33
d_{av} (nm)/% ε (×10^{-4}) (a.u.) **Hematite**	-	-	-	-	-	-	-	-	-	-	-	-	-	11	13

Table 3.2: Saturation magnetization, percentage of total magnetic phases and relative percentage of Fe_3O_4 and Fe_2O_3 for glass heat treated at different T_A and t_A.

T_A	750 °C			850 °C			950 °C			1050 °C			1150 °C		
t_A	1h	2h	3h	1h	2h	3h	1h	2h	3h	1h	2h	3h	1h	2h	3h
M_s (emu/g)	0.2	0.24	0.26	0.3	0.32	2.03	0.53	0.86	0.87	0.68	5.15	0.39	0.23	0.48	0.37
Total magnetic phase (%)	0.21	0.20	0.21	0.43	0.43	2.20	0.49	0.93	0.94	0.74	5.59	0.42	0.25	0.52	0.40
% Fe_3O_4	0.21	0.20-	0.20	0.44	0.43	2.20	0.49	0.93	0.94	0.74	5.59	0.42	0.25	0.47	0.31
% α-Fe_2O_3	-	-	-	-	-	-	-	-	-	-	-	-	-	0.05	0.09

3.1.4 EPR studies

Room temperature EPR spectra of heat treated glass show significant dependence on both T_A and t_A. EPR spectra of samples are shown in Fig. 3.7. Two absorption lines centered at $g \approx 2.1$ and $g \approx 4.3$ are the characteristic features of EPR spectra of glasses containing Fe ions (an absorption line at $g \approx 6.0$ has also been observed in some systems [MNOF90a, DWMO75a, RAO95a]. The origin of these g values in glasses and glass ceramics are closely related to the coordination numbers. The EPR absorption at $g \approx 4.3$ is characteristic of isolated Fe^{3+} ($3d^5$, $^6S_{5/2}$) ions predominantly situated in low symmetry (rhombic) sites of either tetrahedral or octahedral coordination and the one at $g \approx 2.1$ is attributed to those ions which interact by superexchange coupling. Fe^{2+} ions are not involved in EPR absorption but their interaction with Fe^{3+} ions influences the characteristics of the absorption lines [CAST04a, RAO95a].

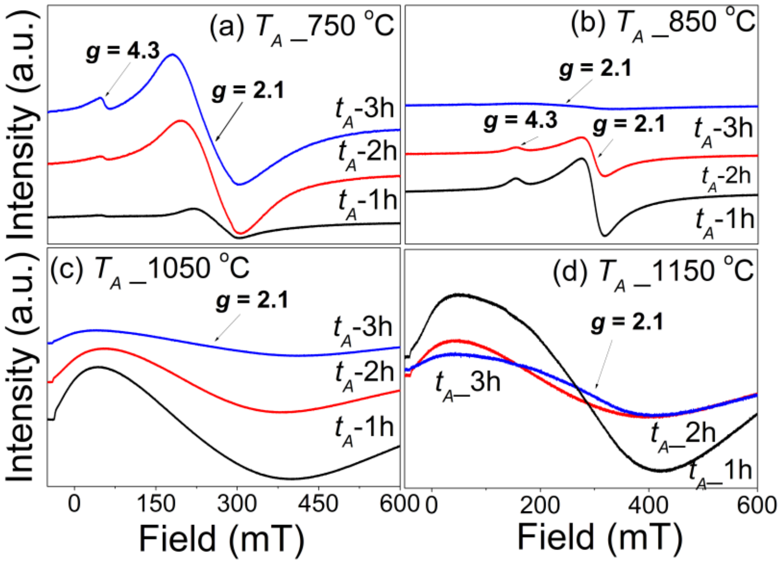

Fig. 3.7: Room temperature EPR spectra of glass annealed at (a) 750 °C, (b) 850 °C, (c) 1050 °C and (d) and 1150 °C for different time periods.

Both the resonance absorptions are present in glass heat treated at 750 °C and 850 °C for different time periods. However, glass heat treated above 850 °C did not exhibit the $g \approx 4.3$ absorption. Since the $g \approx 4.3$ absorption arises from Fe^{3+} ions in low symmetry sites, the disappearance of the $g \approx 4.3$ absorption in the glass-ceramic samples confirms a decrease of low symmetry sites at Fe^{3+}. The development of a strong absorption at $g \approx 2.1$ indicates the development of superexchange interaction facilitated by clustering of Fe ions. EPR parameters, *viz*., absorption line intensity (J) estimated from peak to peak height (I) and linewidth (ΔH) of the EPR absorption profiles of glass heat treated at different conditions are depicted in Fig. 3.8. The increase in J and ΔH of the $g \approx 2.1$ absorption line up to 1050 °C signifies the dominance of clustering mechanism with increasing T_A and t_A [ARDE97a].

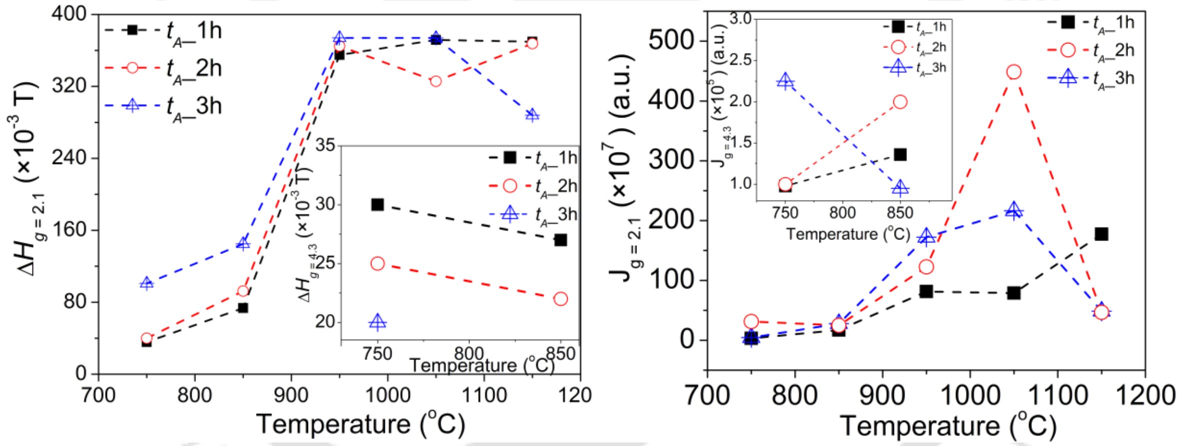

Fig. 3.8: EPR parameters of $g \approx 2.1$ and $g \approx 4.3$ resonances of heat treated glass.

Heat treatment induces nucleation and crystallization of magnetite in the non-magnetic glassy matrix. At low T_A and t_A, nucleation and crystallization of magnetite crystallites occur in a randomly distributed manner in the glassy matrix, resulting in random magnetic interaction. The decrement observed in J and ΔH of $g \approx 2.1$ absorption beyond 1050 °C, can be attributed to the precipitation of hematite phase in the glassy matrix. Presence of such nonmagnetic ions suppresses the superexchnage interaction of the neighbors leading to the observed decrease in the EPR parameters. These results are supported by XRD and magnetization data on the samples.

3.1.5 *In vitro* bioactivity test

In vitro mineralization of the glass-ceramics was evaluated using the procedure discussed in section 2.2.5.1. Fig. 3.9 shows the typical GI-XRD patterns obtained from the surfaces of glass heat treated at 1050 °C for 2 h before and after soaking in SBF for various time periods *i.e*, 0 days (0d) to 15 day (15 d). On immersion in SBF for a day, suppression of crystalline peaks of the glass-ceramic shows the formation of an amorphous surface layer. It has been shown that *in vitro* test involving immersion of bioactive specimen in SBF factually reflects the *in vivo* response of the specimen [KOKU06a]. Apatite formation on the surface of the glass-ceramics immersed in SBF is governed by chemical reaction of the surface of the matrix with the fluid [OHTS92a]. After 3 days of immersion, two reflections appear at $2\theta \sim 26°$ (002) of HA and $2\theta \sim 32°$. The latter broad reflections corresponds to the overlap of (112), (300) and (202) of HA. With further immersion time, these peaks grow in intensity and become sharper, indicating the formation of a well crystallized HA layer on the surface of the sample. This *in vitro* behaviour confirms the strong bioactive character of the samples which is primarily due to the large amounts of bone mineral phase present in the sample. Average size (d_{av}) of HA crystallites in the surface layer was estimated from profile analysis of the broadened (002) reflection using Eq. (2.3). d_{av} increases from about 17 ± 0.5 nm to 32 ± 0.6 nm in samples immersed for 3 days to 15 days. Variation of d_{av} with immersion time depicted in Fig. 3.10 shows an increase in HA crystallite size in samples treated in SBF for more than 3 days. Sharpening of the broad peaks signifies HA layer evolution from small nanocrystallites to a well-crystallized aggregate.

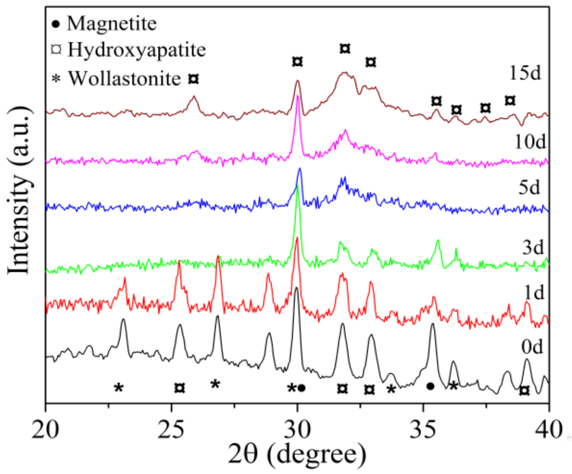

Fig. 3.9: GI-XRD patterns of glass heat treated at 1050 °C for 2 h showing the nucleation and growth of HA surface layer as a function of immersion time in SBF.

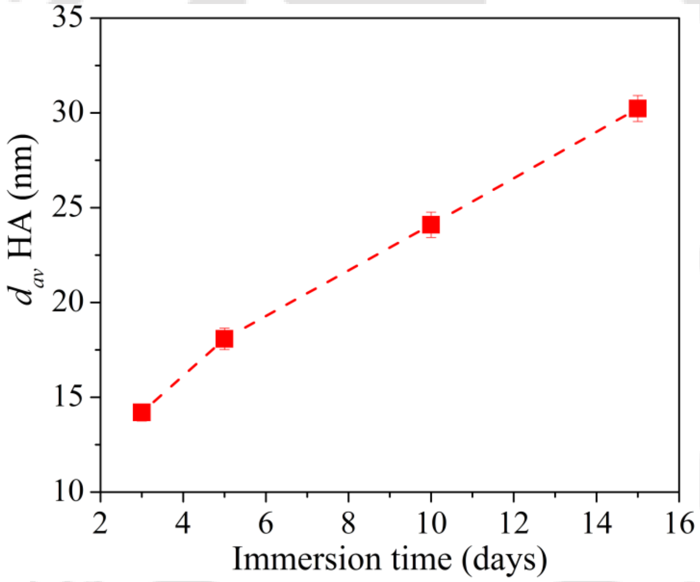

Fig. 3.10: Average crystallite size of HA surface layer on glass heat treated at 1050 °C for 2 h after immersed in SBF.

FESEM micrographs of the glass-ceramic treated in SBF provide visual evidence of gradual development of apatite layer on the surface of glass-ceramics after immersion for various time periods. Gradual formation of the HA surface layer, its crystallization and aggregation with increased immersion time is pictorially depicted in Fig. 3.11. After 15 days of immersion, the surface of sample is completely covered with HA layer. EDS spectrum of the sample surface immersed in SBF for 15 days shown in Fig. 3.12 confirms the presence of Ca, and P along with Na and Cl. Presence of Na and Mg presence is expected due to their presence in SBF.

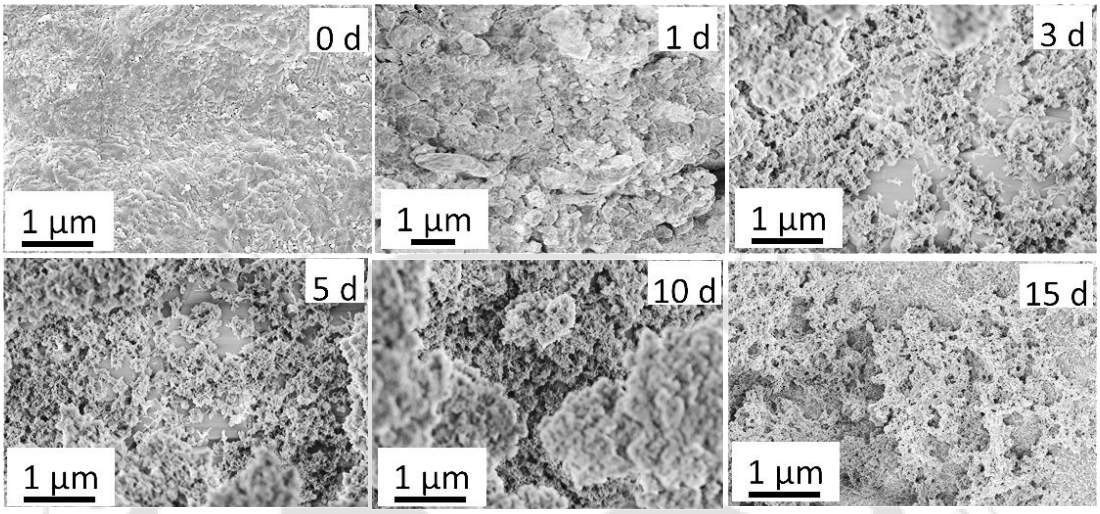

Fig. 3.11. FESEM images of glass heat treated at 1050 °C for 2 h after immersion in SBF up to 15 days showing the growth of HA on the surface.

HA formation and its growth on the surface of a bioactive specimen is a pH sensitive reaction as it involves exchange of ions with the medium [OHTS92a]. As glass heat treated at 1050 °C for 2h shown better structural and magnetic properties, samples heat treated at 1h, 2h and 3h chosen for pH measurement.

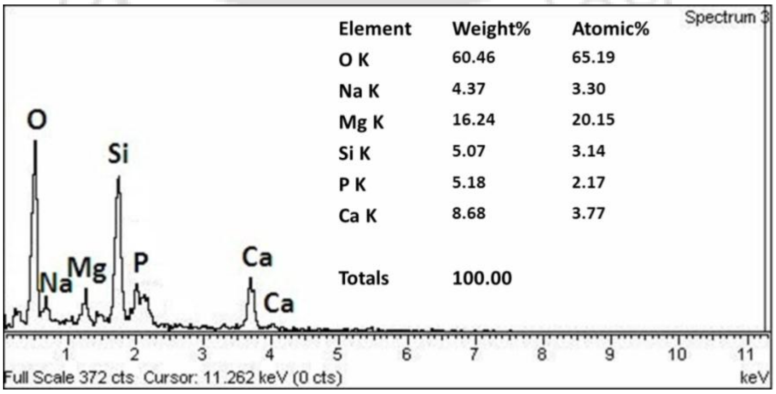

Element	Weight%	Atomic%
O K	60.46	65.19
Na K	4.37	3.30
Mg K	16.24	20.15
Si K	5.07	3.14
P K	5.18	2.17
Ca K	8.68	3.77
Totals	100.00	

Fig. 3.12. EDS spectrum of glass heat treated at 1050 °C for 2 h after immersion in SBF up to 15 days.

pH variation of SBF containing glass heat treated at 1050 °C for 1, 2 and 3 h is depicted in Fig. 3.13. Mechanism of HA formation in bioactive silica-based ceramic materials can be described in terms of pH variation of the medium (SBF) as follows: During early stage of immersion (up to 3 days), the reaction is initiated through exchange of H_3O^+ ions from SBF with cations such as Na^+, Ca^{2+} in the sample. Though H_3O^+ ions do not influence the pH of medium much, they initiate the necessary hydrolysis reaction. This ion exchange reaction results in the formation of a hydrated silica gel layer. This layer is abundant in silanol (Si-OH) groups and provides favorable sites for the calcium phosphate nucleation. This process is signified by a small increase in pH of SBF as observed in Fig. 3.13. As immersion time increases from 5 to 10 days, water molecules in the SBF react with the Si-O-Si bond to form additional Si-OH groups which induce HA nucleation and a corresponding large increase in pH. Data in Fig. 3.13 shows that the ion exchange process saturates at ~ pH 8.0 indicating that the HA layer formation is complete. It can be seen from the figure that the sample heat treated for 2 h shows a comparatively faster ion exchange than the one heat treated for 1h and 3h.

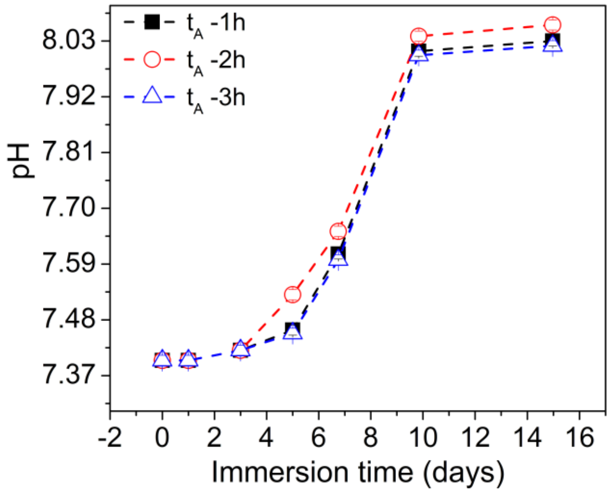

Fig. 3.13. Variation of pH of glass heat treated at 1050 °C at t_A = 1 h, 2 h and 3 h.

3.2 Bulk 15(ZnO,Fe_2O_3).50SiO_2.20(CaO,P_2O_5).15Na_2O glass-ceramics

It is known that zinc helps in many physiological processes such as optimizing human immune system, enhancing wound healing, promoting cleansing of debris and exudate from the wound surface and inhibiting bacterial growth [SOGO05a, AINA09a, RKSI10a, RKSI11a, BALA07a]. Incorporation of zinc in a bioactive glass does not seem to deteriorate its bioactivity [BALA07a]. It has already been pointed out that treatment of ZnO-Fe_2O_3-CaO-SiO_2 glasses resulted in glass-ceramics containing $Zn_xFe_{3-x}O_4$ phase with high magnetization (M_s = 165 emu/g) [KAWA04a]. In our quest to try the second strategy of preparing bioglass-ceramics containing a stronger magnetic phase, we chose to study 15(ZnO,Fe_2O_3).50SiO_2.20(CaO,P_2O_5).15Na_2O glass. In this composition, Ca/P and Fe/Zn molar ratios are 1.67 and 6.5, which correspond to their molar ratio in bone mineral and ferrimagnetic $Zn_{0.4}Fe_{2.6}O_4$ phases.

3.2.1 Preparation

Glass with a composition (in mole %) of 15(ZnO,Fe_2O_3).50SiO_2.20(CaO,P_2O_5).15Na_2O was prepared by melting quenching method. T_g of as-quenched glass was determined to be 520 °C from a DSC run performed at constant heating rate of 20 °C/minute. So, glass pieces were heat treated in air at temperatures (T_A) between 550 and 850 °C for different time periods (t_A) ranging from 1 h to 3 h in air to yield glass-ceramics.

3.2.2. Structural investigations

Fig. 3.14(a-d) show the XRD patterns of glass heat treated at T_A = 550, 650, 750 and 850 °C for t_A = 1, 2 and 3 h, along with that of the parent glass. XRD patterns corresponding to glass heat treated at each T_A is separately shown in the figure for ease of visualization. It is evident from Fig. 3.14(a) that heat treatment at 550 °C for 1 h is sufficient to induce significant crystallization in the glass. XRD patterns of glass heat treated at 550 °C show the initial devitrification process as t_A is increased from 1 to 3 h. Appearance of broadened reflections in the XRD patterns confirms the evolution of various nanocrystalline phases with heat treatment. Indexing the XRD patterns reveals the presence of bone mineral phase calcium sodium phosphate ($NaCaPO_4$) in all the heat treated samples. After indexing the reflections corresponding to $NaCaPO_4$, a few unindexed extra peaks were observed which matched with $ZnFe_2O_4$ powder diffraction file (Table 2.1). Since, Zn/Fe molar ratio in the parent glass was optimized for nucleating $Zn_{0.4}Fe_{2.6}O_4$ phase, we wanted to verify if this phase of $ZnFe_2O_4$ could be crystallized in this effort.

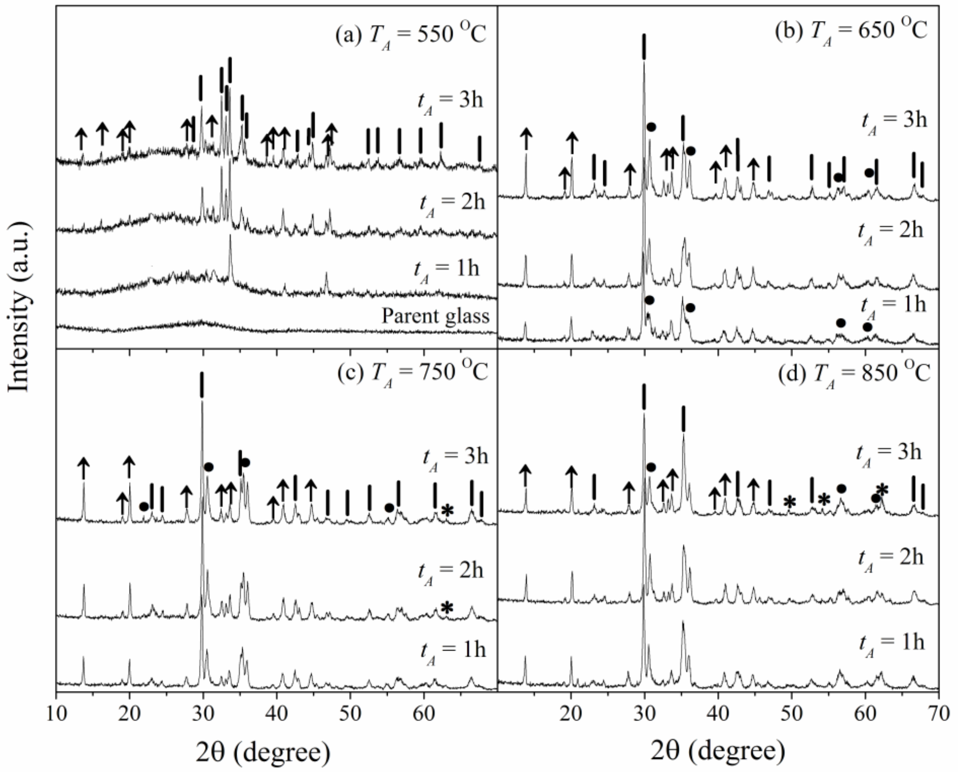

Fig. 3.14: X-ray diffraction patterns of glass heat treated at (a) 550 °C, (b) 650 °C, (c) 750 °C, and (d) 850 °C. Crystalline phases present are calcium sodium phosphate (↑), zinc iron oxide (|), magnetite (●) and α-hematite (∗).

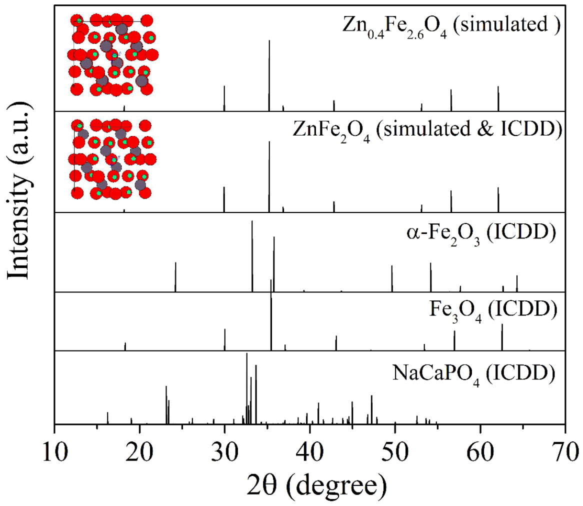

Fig. 3.15. XRD patterns of $NaCaPO_4$, Fe_3O_4, α-Fe_2O_3 and $ZnFe_2O_4$ from ICDD. Unit cell and simulated XRD patterns of $Zn_{0.4}Fe_{2.6}O_4$, are also shown. Black, red and green symbols in the unit cells denote Zn, Fe and O atoms, respectively.

Lack of ICDD file on $Zn_{0.4}Fe_{2.6}O_4$ prompted us to simulate the XRD pattern for $Zn_{0.4}Fe_{2.6}O_4$ using CaRIne Crystallography 3.1^{TM} software. XRD patterns of $ZnFe_2O_4$ and $Zn_{0.4}Fe_{2.6}O_4$ were simulated using unit cells shown in Fig. 3.15. Peak positions and intensities of the reflections in both these zinc ferrite phases (*i.e.*, $ZnFe_2O_4$ and $Zn_{0.4}Fe_{2.6}O_4$) are nearly the same, making it very difficult to distinguish between the two phases. Hence, the second phase present in the glass annealed at 550 °C would be referred to as zinc ferrite phase henceforth, although the Zn/Fe ratio in the matrix points towards the presence of $Zn_{0.4}Fe_{2.6}O_4$. Heat treatment of the glass at 650 °C indicates [*cf.* Fig. 3.14(b)] the formation of magnetite (Fe_3O_4) and growth of calcium sodium phosphate and zinc ferrite nanocrystallites. Formation of Fe_3O_4 at this temperature is due to the decomposition of zinc ferrite through one of the following reactions [KANE04a].

$$3ZnFe_2O_4 = 3Zn + 2Fe_3O_4 + 2O_2 \qquad (3.1)$$

or

$$6ZnFe_2O_4 = 6ZnO + 4Fe_3O_4 + O_2 \tag{3.2}$$

Fig. 3.14(c) shows that heating the glass to 750 °C increases the amount of decomposition of $ZnFe_2O_4$ to magnetite and upon prolonged heating, Fe_3O_4 gets oxidized to form hematite (α-Fe_2O_3) through the following reaction [GENU14a],

$$2Fe_3O_4+0.5O_2 = 3Fe_2O_3 \tag{3.3}$$

As discussed in section 3.1, heat treatment of glass containing iron oxide above 650 °C favours the formation of maghemite (γ-Fe_2O_3) and hematite (α-Fe_2O_3). Of these two phases, α-Fe_2O_3 is a weak ferromagnetic material (M_s = 0.3 emu/g) above its Morin transition temperature ($T_M \approx 263$ K) and antiferromagnetic below T_M [TEJA09a]. Thus, during the course of progressive heat treatment of $15(ZnO,Fe_2O_3).50SiO_2.20(CaO, P_2O_5).15Na_2O$ glass, calcium sodium phosphate and $ZnFe_2O_4$ nucleate and grow as primary phases at $T_A \approx 550$ °C. On further increase in T_A, $ZnFe_2O_4$ decomposes into Fe_3O_4. On prolonged heating at $T_A > 650$ °C, Fe_3O_4 further decomposes into α-Fe_2O_3. Reduction in intensity of reflections assigned to zinc ferrite phase in XRD patterns of glass heat treated at $T_A > 650$ °C supports this interpretation.

Calcium sodium phosphate is a bone mineral and its presence indicates the biocompatible nature of the glass-ceramics. Average crystallite sizes (d_{av}) of the nanocrystalline phases that crystallize in this glass at $T_A \approx 550$ °C have been calculated using the Williamson - Hall relation [Eq. 2.2], Variation of average crystallite size d_{av} of zinc ferrite and calcium sodium phosphate crystallites in glass heat treated at different T_A and t_A are depicted in Fig. 3.16 and also tabulated in Table 3.3. Both the crystallites grow with increase in T_A and t_A, Table 3.3 shows that the internal strain increases with T_A and t_A, probably due to rapid growth of closely nucleated crystallites.

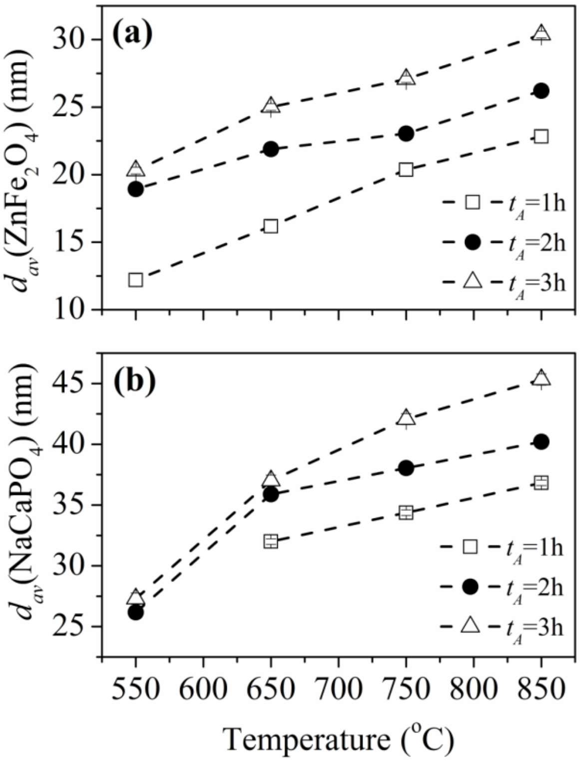

Fig. 3.16: Variation of average crystallite size d_{av} of (a) zinc ferrite and (b) calcium sodium phosphate crystallites in glass heat treated at different T_A and t_A.

3.2.3 Magnetic characterization

Since the main interest in this work was to evaluate the prospects of the heat treated glass for use as thermo-seeds, their room temperature magnetic properties were evaluated. Fig. 3.17(a-d) depicts the room temperature magnetic hysteresis (*M-H*) loops of glass heat treated at different T_A and t_A. Insets in Fig. 3.17 provide an expanded view of the data close to the origin. It is evident from the *M-H* data that none of the samples show magnetic saturation up to an applied magnetic field of ±15 kOe, which the expected behavior of samples containing small amounts of ferrimagnetic phase(s). Table 3.3 lists the magnetization of the glass measured at ±15 kOe ($M_{s(15kOe)}$) after heat treatment at different T_A and t_A. It can be seen that $M_{s(15kOe)}$ of glass heat treated at any one t_A (say, 1 h or 2 h or 3 h) increases with T_A.

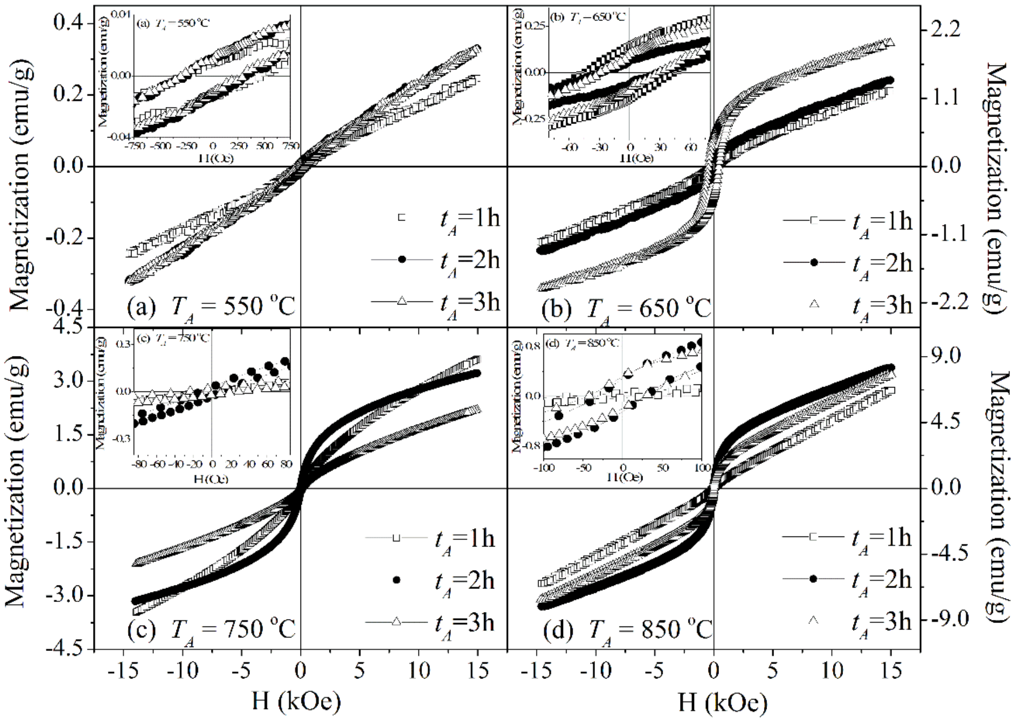

Fig. 3.17: Room temperature magnetic hysteresis loops of glass heat treated at different T_A and t_A. Insets show an expanded view of the data close to the origin.

However, a closer look at the data in Table 3.3 tells us that $M_{s(15kOe)}$ increases with increase in t_A for glass heat treated at $T_A \leq 650$ °C. On the other hand, $M_{s(15kOe)}$ of glass heat treated at $T_A = 750$ °C decreases with increase in t_A, whereas, heat treatment at 850 °C yields the highest $M_{s(15kOe)}$ for $t_A = 2$ h (*cf.* Fig. 3.18). This result can be compared with $M_{s(15kOe)}$ value of 0.32 emu/g reported for bioglass 45S5 containing 8 mole % Fe_2O_3 heat treated at 850 °C for 2 h (*cf.* Table 3.2). In fact, the maximum $M_{s(20kOe)}$ of 5.15 emu/g obtained for this glass-ceramic when heat treated at 1050 °C for 2 h is also much lower than the $M_{s(15kOe)}$ obtained for the present sample upon heat treatment at 850 °C for 2 h. This clearly shows the stronger magnetic properties of $15(ZnO,Fe_2O_3).50SiO_2.20(CaO, P_2O_5).15Na_2O$ glass-ceramic.

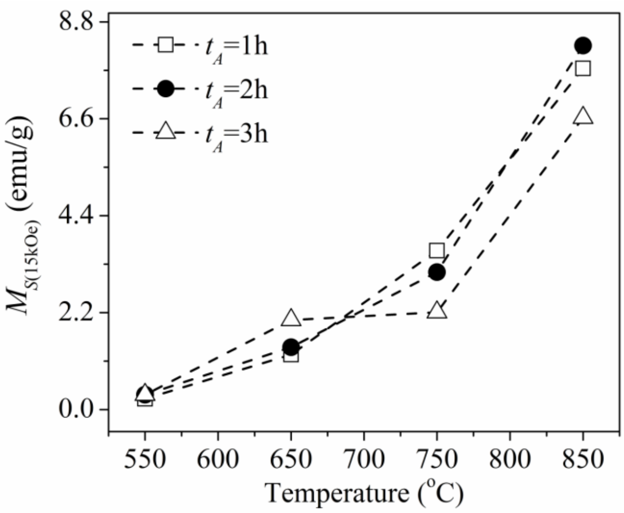

Fig. 3.18: Magnetization ($M_{s(15kOe)}$) of glass heat treated at different T_A and t_A.

Since the magnetic properties arise due to the magnetic phase(s) present in the sample, the $M_{s(15kOe)}$ data reflects the changes in the constitution and quantity of magnetic phase(s) crystallizing in the glass upon heat treatment. One can estimate the percentage of magnetic phase present in the sample from the ratio $M_{s(g-c)}/M_{s(mph)}$, where $M_{s(g-c)}$ is the measured $M_{s(15kOe)}$ of heat treated glass samples and $M_{s(mph)}$ is the average saturation magnetization of the magnetic phase(s) present in the sample. Quantitative analysis of the crystal fraction of various magnetic phases present in the heat treated samples carried out as per section 2.2.1.1. Primary diffraction peaks of zinc ferrite (311), magnetite (311) and hematite (121) phases in the respective XRD patterns were used in this analysis after normalization and baseline subtraction. By estimating the ratio of the integrated intensity of the primary peak of the magnetic phases present, one can estimate $M_{s(mph)}$ as ($165x + 92y + 0.3z$), where 165 [NOHS12a], 92 [CULL08a] and 0.3 [TEJA09a] are the M_s (in emu/g) and x, y and z are the crystal fraction of zinc ferrite, magnetite and hematite, respectively. Percentage of $ZnFe_2O_4$, Fe_3O_4 and α-Fe_2O_3 phases in glass heat treated at different conditions estimated is tabulated in Table 3.3 along with total magnetic phase present in the samples. It can been seen that, the amount of $ZnFe_2O_4$ phase increases in glass heat treated up to 650 °C in accordance with the XRD results portrayed in Fig. 3.14 (a, b) and also accounts for the increase in $M_{s(15kOe)}$ of the glass-ceramic samples. The decrease in the percentage of $ZnFe_2O_4$ phase and in turn $M_{s(15kOe)}$ upon prolonged treatment at 750 °C is a consequence of the formation of Fe_3O_4 (whose M_s is lower than that of the $ZnFe_2O_4$ phase) and α-Fe_2O_3 (which is a very weak ferromagnetic material).

High amounts of magnetic phases present (~68 % of $ZnFe_2O_4$, ~25 % Fe_3O_4 and only ~7 % of α-Fe_2O_3) in samples heat treated at 850 °C for 2 h are responsible for the highest $M_{s(15kOe)}$ recorded at this heat treatment condition. Deterioration in $M_{s(15kOe)}$ on prolonged (*i.e.*, for $t_A > 2$ h) heat treatment at this temperature is due to the decomposition of $ZnFe_2O_4$ phase and increased oxidation of Fe_3O_4 into α-Fe_2O_3. Phase fraction of ~11 % of α-Fe_2O_3 is estimated in samples heat treated at 850 °C for 3h.

Coercivity (H_c) of the samples decreases with increasing T_A as shown in Fig. 3.19 (a) and in the insets of Fig. 3.16. Higher H_c at 550 °C is a result of spontaneous and random nucleation and growth of $ZnFe_2O_4$ phase initiated at this temperature. During heat treatment, iron content tends to aggregate into clusters in the glassy oxide matrix. Increase in $ZnFe_2O_4$ crystallite size lowers the coercivity sharply. For $T_A > 650$ °C, partial conversion of ferrimagnetic Fe_3O_4 into α-Fe_2O_3 results in the reduction of magnetic content and leads to saturation of H_c. The area under the hysteresis loop increases with increasing T_A as illustrated in Fig. 3.19 (b). The maximum hysteresis loop area of 5362 erg/g was recorded for glass heat treated at 850 °C for 2 h.

Hence, $15(ZnO,Fe_2O_3).50SiO_2.20(CaO, P_2O_5).15Na_2O$ glass heat treated at 850 °C for 2 h has the best combination of magnetic properties required for a thermos-seed.

Table 3.3: Average crystallite size (d_{av}) of zinc ferrite and calcium sodium phosphate crystallites, magnetization at 15 kOe ($M_{s(15kOe)}$), percentage of total magnetic phases, relative percentage of $ZnFe_2O_4$, Fe_3O_4, α-Fe_2O_3 and hysteresis loop area for ±15 kOe sweep for glass heat treated at different T_A and t_A.

	T_A = 550 °C			**T_A = 650 °C**			**T_A = 750 °C**			**T_A = 850 °C**		
t_A	**1h**	**2h**	**3h**	**1h**	**2h**	**3h**	**1h**	**2h**	**3h**	**1h**	**2h**	**3h**
d_{av} (nm)/% ε ($\times10^{-4}$) (a.u.) $ZnFe_2O_4$	12/5	19/17	20/32	16/5	22/22	25/36	20/12	23/41	27/43	23/22	26/39	30/43
d_{av} (nm)/% ε ($\times10^{-5}$) (a.u.) $NaCaPO_4$	-	26/12	27/23	32/24	35/32	37/35	34/32	38/33	42/50	36/32	40/45	45/56
$M_{s(15kOe)}$ (emu/g)	0.25	0.33	0.34	1.25	1.41	2.03	3.61	3.12	2.21	7.74	8.26	6.62
Total magnetic phase (%)	0.15	0.20	0.21	1.00	1.13	1.59	2.83	2.56	2.03	5.33	5.75	4.33
% $ZnFe_2O_4$	0.15	0.20	0.21	0.45	0.50	0.76	1.40	1.05	1.12	3.20	3.52	2.63
% Fe_3O_4	-	-	-	0.55	0.63	0.83	1.43	1.51	0.88	2.04	2.13	1.57
% α-Fe_2O_3	-	-	-	-	-	-	-	-	0.03	0.09	0.1	0.13
Loop area for H = ±15kOe (erg/g)	285	314	308	1066	1149	1651	2893	2694	1923	5014	5362	5188

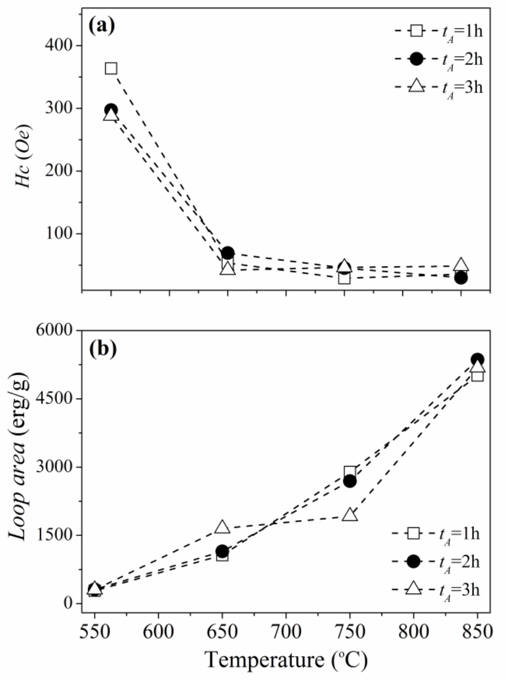

Fig. 3.19: Variation of (a) coercivity and (b) area under the hysteresis loop under ±15 kOe of glass-ceramics as a function of T_A and t_A.

3.2.4 EPR studies

EPR absorption spectra of glass heat treated at 750 °C and 850 °C recorded at room temperature are plotted in Fig. 3.20 (a) and (b), respectively. The integrated spectra are also shown in Fig. 3.20 so that the influence of t_A at these T_A's could be observed.

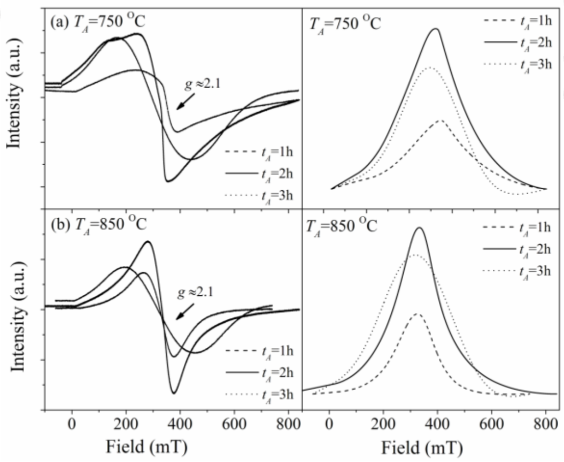

Fig. 3.20: Room temperature EPR absorption (derivative and integrated) spectra of glass heat treated at (a) 750 °C (b) and 850 °C for 1, 2 and 3 h.

Since Fe^{3+} ions in $ZnFe_2O_4$ and Fe_3O_4 occupy similar sites in their spinel structure, the following discussion will simply refer to Fe^{3+} ions present in both these phases. EPR spectra of both the samples show only one resonance absorption at $g \approx 2.1$ corresponding to cluster formations of zinc-iron oxide [SING11a, KOMA08a]. It can be observed that peak to peak height (I) of this absorption line decreases as t_A increases at both temperatures.

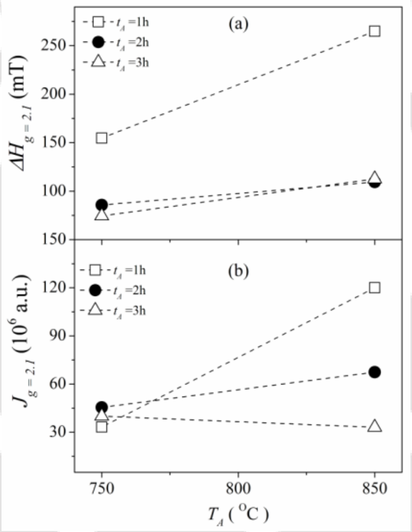

Fig. 3.21: (a) Linewidth and (b) line intensity of the EPR resonance at $g \approx 2.1$ of glass heated treated at 750 °C and 850 °C for different t_A.

Linewidth (ΔH) and intensity (J) of the EPR absorption profile of the glass heat treated at 750 and 850 °C are depicted in Fig. 3.21(a) and Fig. 3.21(b), respectively. It is evident from Fig. 3.21(a) that ΔH increases when T_A is increased from 750 °C to 850 °C irrespective of t_A. But prolonged heating at 750 °C results in decrease in ΔH. This decrement observed in ΔH for $t_A > 1$ h is due to the precipitation of the weak magnetic phase in the glassy matrix upon prolonged heating at this temperature. Presence of such weak magnetic phase suppresses the super-exchange interaction, leading to the observed decrease in the EPR parameters [ENIU05a, RKSI1a, JEYA94a]. Fig. 3.21(b) shows a much complex variation of line intensity with T_A and t_A. J increases at 850 °C for t_A up to 2 h but shows a decrease for $t_A = 3$ h. Increase in J for lower t_A signifies the dominance of clustering mechanism as the crystallization of magnetite increases and the decrease in J for 3 h heat treatment signifies the precipitation of weakly magnetic hematite at this temperature as discussed above.

3.2.5 *In vitro* bioactivity test

Glass sample heat treated at 850 °C for 2 h was chosen for SBF study since they exhibited the best magnetic properties required for a thermo-seed. Procedure outlined in section 2.2.5 was followed for this study. Specimen immersed in SBF were taken out after 1, 3, 5, 10 and 15 days and lightly washed with acetone.

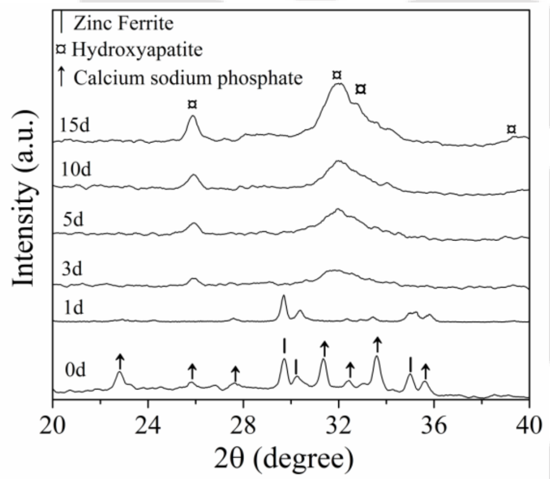

Fig. 3.22: GI-XRD patterns of glass heat treated at 850 °C for 2 h showing the nucleation and growth of HA surface layer with immersion time in SBF.

Fig. 3.22 shows the typical GI-XRD patterns obtained from the surfaces of glass-ceramics before and after soaking in SBF for various time periods. XRD pattern of the untreated (fresh) sample is designated as 0 d in Fig. 3.22. On immersion in SBF for a day, suppression of crystalline peaks shows the formation of an amorphous surface layer on the glass-ceramic sample. After 3 days of immersion, the HA two

Indian Institute of Technology Guwahati

reflections centered at 2θ values of ~26° (002) and 32° (overlapping (112), (300) and (202) appear. With further immersion time, these reflections get stronger and sharper, indicating the formation of a well crystallized HA surface layer. Average HA crystallite size d_{av} increases from 12 ± 0.5 nm to 28 ± 0.6 nm in samples immersed for 3 days and 15 days. Variation of d_{av} with immersion time depicted in Fig. 3.23 shows an increase in HA crystallite size with immersion time. Zn present in the biomaterial can induce a special stacking of HA nanocrystals leading to preferential orientation for HA [BALA07a].

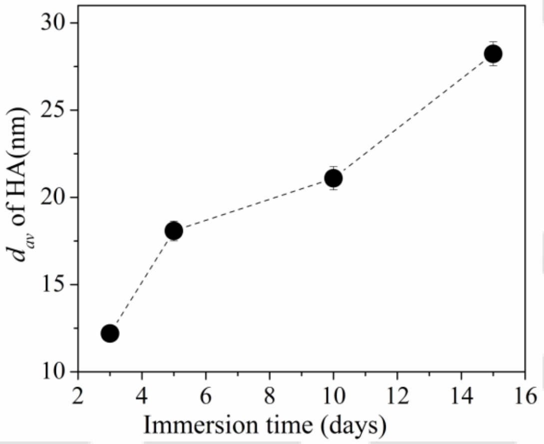

Fig. 3.23: Average crystallite size of HA surface layer on glass heat treated at 850 °C for 2 h after immersion in SBF.

FESEM micrographs of glass-ceramics immersed in SBF for various time periods in SBF are shown in Fig. 3.24 (a-e). The gradual formation of the HA surface layer at various stages of immersion can be visualized from these pictures. Fig. 3.24(f) shows the EDS spectrum of the sample surface immersed in SBF for 15 days which confirms the presence of Ca, and P along with Na and Cl. Here, Na and Cl in the surface layer is a characteristic of the medium used. Zn and Fe are not observed in the spectrum indicating that they do not get incorporated in the HA layer.

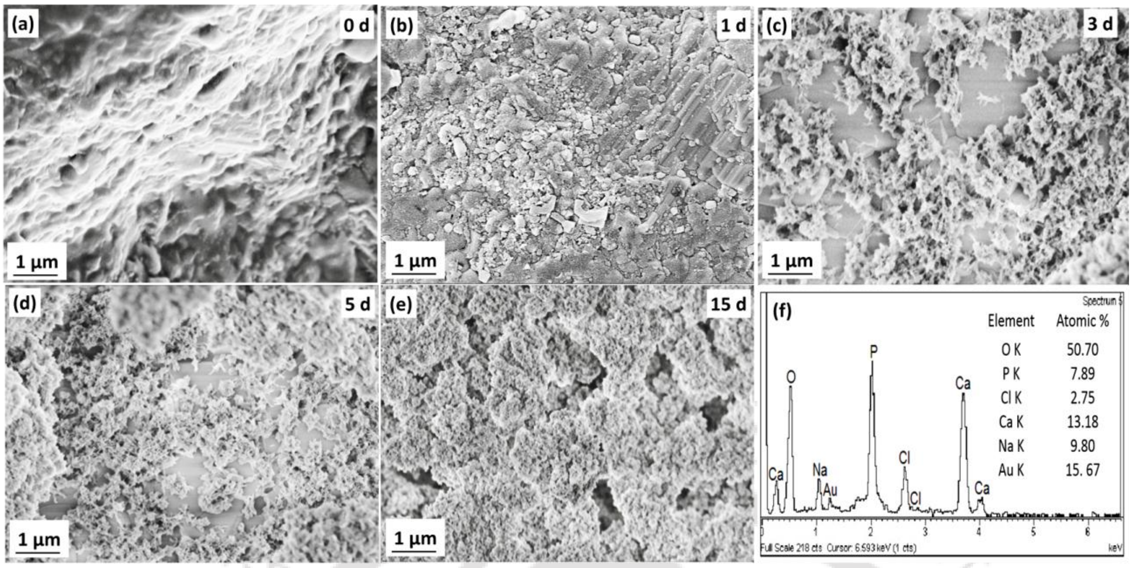

Fig. 3.24: (a-e) FESEM images of glass heat treated at 850 °C for 2 h after immersion in SBF up to 15 days showing the growth of HA on the surface. (f) EDS spectrum of sample immersed in SBF for 15 days.

Earlier reports [RKSI10a, SHAH10a] have also ruled out the possibility of Fe and Zn incorporation in the HA layer during immersion in SBF in agreement with our GI-XRD results shown in Fig. 3.22. Moreover, Sogo *et al.* [SOGO05a] have pointed out that it is difficult to form Zn containing apatite during immersion in SBF which might be the reason for its absence in our EDS data.

Monitoring pH of SBF during immersion provides information about the HA formation and its growth on the surface of a bioactive specimen since it is a pH sensitive reaction [OHTS92a]. In order to study the chemical degradation of glass-ceramics and the effect of the weak magnetic α-Fe_2O_3 phase, a comparative study on pH variation of glass heat treated at 750 °C and 850 °C (*cf*. Fig. 3.25) was undertaken. Mechanism of HA formation in bioactive silica-based ceramic materials is described section 3.1.5 in terms of pH variation of the medium (SBF).

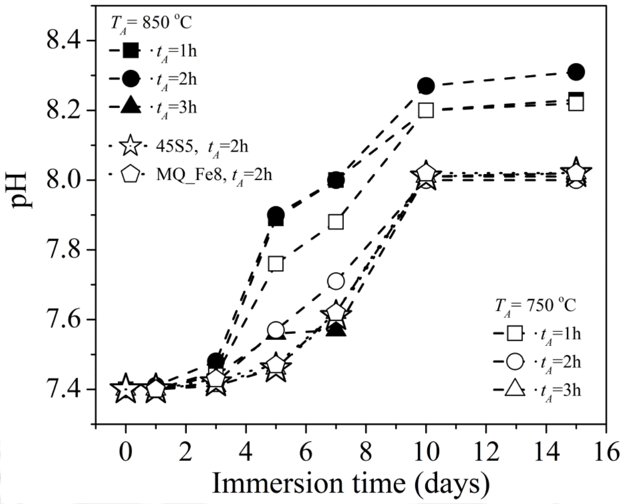

Fig. 3.25: Variation of pH of 15(ZnO,Fe_2O_3).50SiO_2.20(CaO,P_2O_5).15Na_2O glass heat treated at 750 °C (open symbols) and 850 °C (filled symbols) for 1 h, 2 h and 3 h as a function of immersion time in SBF. pH variations of bulk 45S5 (open star) glass and 41CaO44$SiO_2$4$P_2O_5$8$Fe_2O_3$3Na_2O (MQ_Fe8, open hexagon) glass heat treated at 850 °C for 2 h are also shown.

Fig. 3.25 shows the variation of pH of 15(ZnO,Fe_2O_3).50SiO_2.20(CaO, P_2O_5).15Na_2O glass heat treated at 750 °C and 850 °C (filled symbols) for 1 h, 2 h and 3 h as a function of immersion time in SBF. pH variations of bulk 45S5 glass and 41CaO.44SiO_2.4P_2O_5.8Fe_2O_3.3Na_2O glass heat treated at 850 °C for 2 h (designated as MQ_Fe8) are also shown in the Fig. for comparison. It can be seen from the Fig. that samples annealed at 750 °C show a slower increase in pH as compared to one annealed at 850 °C. As immersion time increases from 5 to 10 days, water molecules in the SBF react with the Si-O-Si bond to form additional Si-OH groups which induce HA nucleation. In addition, release of Na^+, Ca^{2+} (and Zn^{2+}) ions accelerates HA nucleation by increasing the ionic activity in the fluid and promotes calcium phosphate nucleation on the surface of sample. Migration of Zn^{2+} increases the pH of SBF and influences the ion exchange mechanism in the following way. Formation of HA is the result of electrostatic interaction between Si-OH group on the glass ceramic surface and the Ca and P ions in the SBF. Formation of Si-OH is accompanied by an increase in pH of SBF. In this process, the glass ceramic surface acquires a negative charge. Zn^{2+} migration enhances this negative charge which strengthens the electrostatic interaction with positively charged Ca ions in the SBF. Zn^{2+} migrates into SBF solution and precipitates as zinc hydroxide ($Zn(OH)_2$) [SOGO05a]. In the case of glass heat treated at 750 °C, a slower pH variation is observed as it has relatively lesser amount of $ZnFe_2O_4$ phase (due to conversion into Fe_3O_4 and α-Fe_2O_3 phases with increasing t_A). The observed trend in pH variation is similar to the one observed in bioglass 45S5 ($46.1SiO_2.26.9CaO.24.4Na_2O.2.5P_2O_5$ in mole %) [RAHA11a] and MQ_Fe8 glass heat treated at 850 °C for 2 h although the actual pH values are quite different (*cf*. Fig. 3.25). This suggests that Fe ions do not get involved in the ion exchange mechanism and hence do not influence the pH of SBF during immersion. Glass annealed at 850 °C for 1 h shows similar trend of pH variation but records slightly higher value of pH as compared to the one annealed at 750 °C for 1 h. On the other hand, glass annealed at 850 °C for 2 h which contains maximum amount of $ZnFe_2O_4$ phase exchanges more Zn^{2+} ions with SBF resulting in the highest value of pH for the same time of immersion. Thus, higher Zn^{2+} ion release in SBF leads to a rapid increase in pH value from 8.00 to 8.38 in 15 days of immersion for this specimen. pH saturates at 8.01 after 15 days of immersion for the glass heat treated at 750 °C for 2 h, However, the same sample heat treated for t_A = 3 h shows a lower pH due to the presence of lesser amount of zinc ferrite phase. This study shows that glass heat treated at 850 °C for 2 h induces larger and faster ion exchange with SBF leading to rapid nucleation and growth of HA layer at the surface. Direct comparison of the pH variation exhibited by heat treated bioglass 45S5 and MQ_Fe8 from the section 3.1 shows that the present glass-ceramics containing zinc ferrite, especially the glass heat treated at 850 °C for 2 h, has better ion exchange mechanism and hence better in vitro bioactivity.

3.3 Summary

- Presence of hydroxyapatite and wollasonite in $41CaO44SiO_24P_2O_58Fe_2O_3 3Na_2O$ and calcium sodium phosphate phases in $15(ZnO,Fe_2O_3).50SiO_2.20(CaO,P_2O_5).15Na_2O$ are mainly responsible for the the bioactive nature of these glass ceramics.
- Deterioration of magnetic properties upon prolonged heat treatment of $41CaO44SiO_24P_2O_58Fe_2O_33Na_2O$ glass well above its T_g us due to the conversion of magnetite into weakly ferromagnetic hematite (α-Fe_2O_3). Excessive precipitation of this weak magnetic phase suppresses the super-exchange interaction between neighboring iron ions, resulting in the observed deterioration in magnetic properties.
- Heat treatment of $41CaO44SiO_24P_2O_58Fe_2O_33Na_2O$ at 1050 $^{\circ}$C for 2 h yielded glass-ceramics with the best combination of magnetic properties.
- Conversion of precipitated zinc ferrite into magnetite and further to weakly ferromagnetic hematite (α-Fe_2O_3) causes deterioration of the magnetic properties of $15(ZnO,Fe_2O_3).50SiO_2.20(CaO,P_2O_5).15Na_2O$ glass heat treated for prolonged periods above T_g.
- $15(ZnO,Fe_2O_3).50SiO_2.20(CaO,P_2O_5).15Na_2O$ glass heat treated at 850 °C for 2 h contains the maximum amount of magnetic as well as bone mineral phases, which makes it best suited for use as thermo-seed in hyperthermia treatment of cancer.

Chapter 4

Investigations on nanoporous bioglass/glass-ceramics and magnetic bioglass/glass-ceramics

In the present chapter, a systematic study on preparation and characterization of sol-gel derived bioactive glass 45S5 and bioglass 45S5 with 2 and 3 wt. % Fe_2O_3 is reported.

4.1 Nanoporous 45S5 bioglass and glass-ceramics

As mentioned in chapter one, 45S5 bioglass composition has excellent biological properties and is hence considered as the prototype bioglass. Though sol-gel derived glasses exhibit better bio response than their melt quenched counterparts, obtaining a completely amorphous 4SS5 glass composition by sol-gel route has been elusive so far. The major challenge in sol-gel synthesis of this bioglass composition is in controlling the kinetics of hydrolysis and polymerization reactions. Attempts to prepare several quaternary bioactive glass compositions by Siqueira *et al*. [SIQU11a, SIQU13a] and Padilla *et al*. [PADI05a] by varying the phosphate precursor resulted in semi-amorphous end products. Vallet-Regí, *et. al* [RAMI02a] pointed out that the challenge lies in the optimization and control of nitrates and phosphate precursors used in the sol-gel synthesis of bioglass. The motive behind the present study is to explore an alternate methodology to prepare bioglass with composition close to 45S5 bioglass by using an appropriate phosphate precursor and controlling the hydrolysis and gelation reactions.

Here, the methodology for obtaining completely amorphous 45S5 bioglass by sol-gel route is explained.

4.1.1 Sol-gel methodology

The modified sol-gel method adopted to prepare bioglass has been explained with a flow-chart in section 2.2.2. Three phosphate precursors, *viz.*, phosphorous pentaoxide, phosphoric acid and di-ammonium hydrogen orthophosphate were used in our search to find the suitable precursor. Nitric acid was used as catalyst. Deionized water was used as solvent. The reactants were taken in proportions required to obtain a final product with the 45S5 composition, *viz.*, 45 wt% SiO_2, 24.5 wt% Na_2O, 24.5 wt% CaO, and 6 wt% P_2O_5. 1 mol L^{-1} HNO_3 was used as catalyst to maintain a pH of 1~2 required to initiate hydrolysis at room temperature since TEOS by itself is not very sensitive to hydrolysis. Condensation reaction followed at room temperature at a slightly higher pH value. The same sol-gel procedure was adopted for the three different phosphate precursors in order to understand the effect of the phosphate precursor under controlled aqueous acidic environment. As-prepared gel was aged for 3 days at ambient conditions and freeze dried at −40 °C. As-dried powder was heat treated at 70 °C for 3 days to eliminate nitrates and other unreacted substances. The last step represents thermal stabilization of the powders in which residual nitrates and other unreacted substances are removed in gaseous form leaving behind a highly porous and gelatinous powder. Dried gel powders were designated as $BG\_P_2O_5$, $BG\_H_3PO_4$ and $BG\_(NH_4)_2HPO_4$ based on the phosphate precursor used in the synthesis.

4.1.2 Structural characterization

XRD patterns of the dried gel powders prepared using different phosphate precursors are shown in Fig. 4.1 (a-c). It is obvious that Fig. 4.1 (a and b) indicate crystalline peaks while Fig. 4.1(c) shows a completely amorphous pattern devoid of any crystalline inclusions. It is evident that Fig. 4.1(c) represents the ideal amorphous pattern we are attempting to obtain for the end product with 45S5 bioglass composition.

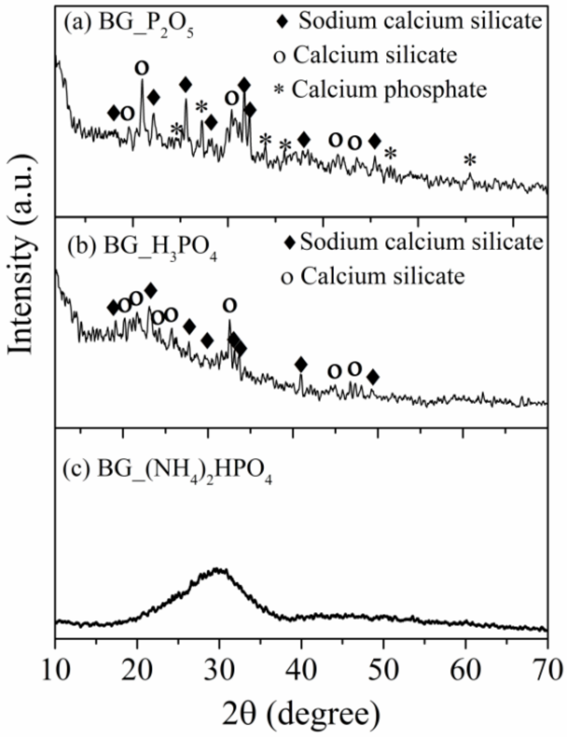

Fig. 4.1: Room temperature XRD patterns of sol-gel derived powders obtained using (a) P_2O_5, (b) H_3PO_4 and (c) $(NH_4)_2HPO_4$ as phosphate precursors.

It is relevant to point out here report that the XRD pattern of sol-gel derived SiO_2–CaO–P_2O_5 powders exhibited the presence of crystalline phosphate phases [SIQU13a]. Moreover, attempts to include 5% to 90% of P_2O_5 in SiO_2–CaO–P_2O_5 led to partially crystallized gel powders [PADI05a]. When H_3PO_4 is used as phosphate precursor, sudden precipitation of gel takes place in the presence HNO_3 catalyst, leading to the crystallization of $Na_2Ca_2Si_3O_9$ as the major phase and $CaSiO_3$ as a minor phase as shown in Fig. 4.1 (b). The microstructure of the specimen obtained by sol-gel process depends on the hydrolysis and condensation reactions. A number of conditions can influence the hydrolysis and condensation reactions. Of these, the most pertinent ones are water-to-alcoxide ratio, type and amount of catalyst, type of organic group attached to the silicon atom and solvent effects [MILE11a].

Sol-gel is highly pH sensitive reaction and can be processed under basic and acidic environments. Several pH-dependent rate profiles have been reported for the hydrolysis and condensation reactions, where it has been found that reaction rates are largely dependent on pH [RWJO89a]. For instance, in acid catalyzed reaction, hydrolysis occurs at a higher rate, while condensation occurs at a slower rate. Whereas, in base catalyzed reaction, an inverse behaviour has been noticed between the rates of the two reactions [RWJO89a, MILE11a, SKYO02a, EDZA92a]. It is this inverse relationship between the rates of the hydrolysis and condensation reactions that must be taken into account in controlling the kinetics of the reaction and hence controlling the ultimate network structure [RWJO89a]. To create a desirable amorphous glassy network through the sol–gel process, the sol must undergo a rapid hydrolysis followed by a slower gelation process. With this understanding, we proceeded to test the phosphate precursor $(NH_4)_2HPO_4$. This phosphate precursor is basic in pH. Hence, after complete hydrolysis at an acidic pH of 1~2, $(NH_4)_2HPO_4$ increases the pH of the mixture towards basic region. The higher pH influences the kinetics of the reaction and results in slower gelation. Slower gelation results in less number of untreated constituents which ultimately precipitate as crystalline phases. Such pH control of the reactions with the use of $(NH_4)_2HPO_4$ can thus induce rapid hydrolysis and slower gelation and hence a completely amorphous gel product. Fully amorphous XRD pattern of BG_$(NH_4)_2HPO_4$ gel powder depicted in Fig.4.1(c) confirms the above reasoning and illustrates the role of $(NH_4)_2HPO_4$ in obtaining a fully amorphous 45S5 glass by sol-gel process.

Since sol-gel synthesis is a two-step wet chemical process, incomplete hydrolysis and condensation reactions result in unreacted precipitates and nitrates in the system. In the present case, the thermal stabilization step takes care of the above and yields fully amorphous BG_$(NH_4)_2HPO_4$ gel powder. FT-IR spectrum of this sample shown in Fig. 4.2 does not contain any of the characteristic N-O bands, which confirms the elimination of nitrates from the end product [BSMI99a].

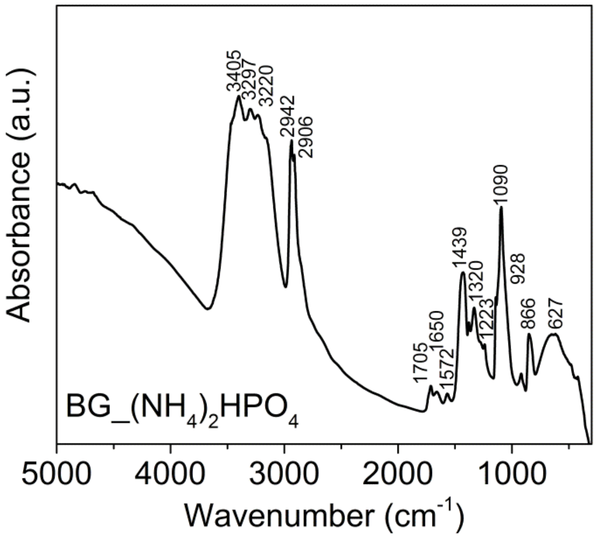

Wavenumber (cm^{-1})	**Assignment**
Silicate chains 1090	Si-O-Si antsymmetric stretching (ν_3)
Phosphate chains	
1223, 1320	PO_2 asymmetric stretching
928	$(PO_4)^{3-}$
627	P-O-P symmetric stretching
Network modifiers	
1439	Carbonate group
866	C-O stretching (ν_2)
3405, 3297, 3220	SiOH (Silanol group)
2942, 2906	Hydrogen bonding
1705, 1650,1572	Molecular water

Fig. 4.2: FT-IR spectrum of BG_$(NH_4)_2HPO_4$ along with a table containing the assignments for the observed peaks.

In order to confirm the amorphous nature of BG_$(NH_4)_2HPO_4$ down to atomic length scales, HRTEM images were taken. HRTEM image shown in Fig. 4.3 (a) confirms the complete amorphous structure of BG_$(NH_4)_2HPO_4$ as no lattice fringes depicting crystalline order could be seen down to a few nm scale. Fig. 4.3 (b) shows the EDS spectrum and the overall concentration of the elements present in the specimen, It can be seen that the measured elemental compositions are Si (21.04 at.%), Ca (17.51 at.%), Na (18.18 at.%), P (2.62 at.%) and O (40.66 at.%) against the nominal composition of 45S5, *viz.*, Si (21.55 at.%), Ca (18.22 at.%), Na (18.10 at.%), P (2.10 at.%) and O (40.03 at.%). The close agreement with the measured and nominal elemental compositions shows that the specimen has a composition very close to 45S5. Fig. 4.3 (c) shows the low resolution FESEM image of BG_$(NH_4)_2HPO_4$ powders showing nearly spherical and agglomerated amorphous particles.

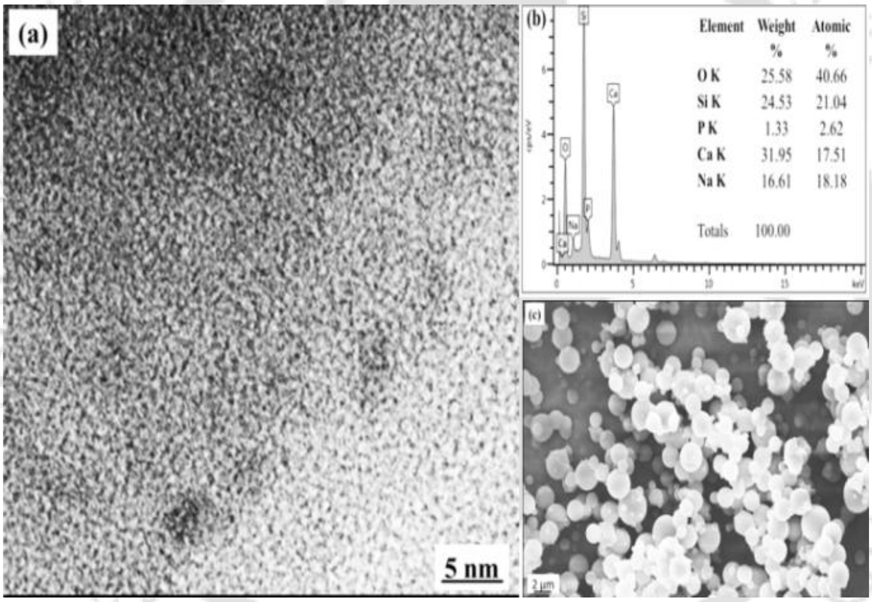

Element	Weight %	Atomic %
O K	25.58	40.66
Si K	24.53	21.04
P K	1.33	2.62
Ca K	31.95	17.51
Na K	16.61	18.18
Totals	100.00	

Fig. 4.3: (a) HRTEM image, (b) EDS spectrum with overall elemental composition map, and (c) FESEM image of BG_$(NH_4)_2HPO_4$.

4.1.3 Thermal properties

Having successfully prepared fully amorphous glass with composition very close to bioglass 45S5 by sol-gel route, we proceeded to characterize the glass. Glass transition temperature (T_g) is the most important parameter for a glass. Fig. 4.4 shows the DSC curve of BG_$(NH_4)_2HPO_4$ recorded at a constant heating rate of 20 K minute^{-1}, illustrating an endothermic baseline shift beginning at 661 °C, and an exotherm with onset at 840 °C and peak at 896 °C. The endothermic baseline shift signifies the supercooled liquid to liquid (glass) transition. The onset temperature of the transition is identified as T_g [BRET09a]. The exotherm corresponds to the crystallization of the bone mineral phase sodium calcium silicate. Bretcanu *et al.* [BRET09a] obtained crystallization temperature (T_g) (onset) at 549 °C and T_c (peak) of 676 °C for melt quenched 45S5 glass powder from DTA curve recorded at the same heating rate.

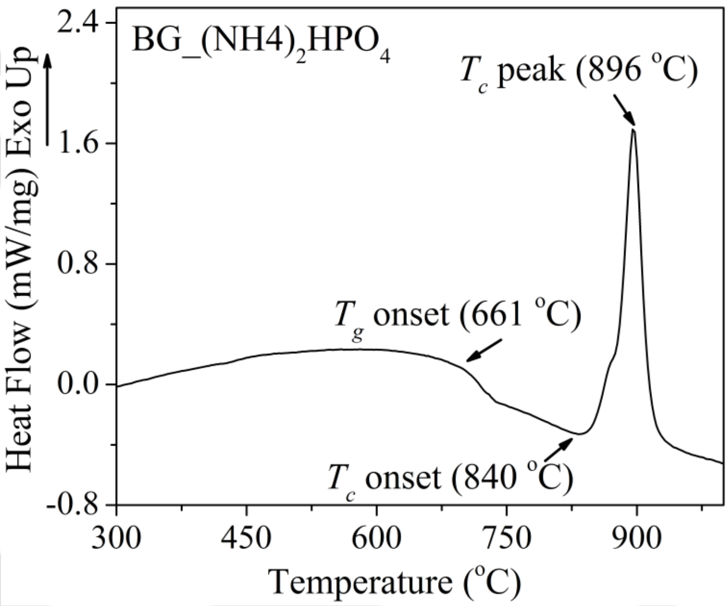

Fig. 4.4: DSC curve of BG_$(NH_4)_2HPO_4$ recorded at $\phi = 20$ K minute^{-1}, showing glass transition and crystallization temperatures.

Massera *et al.* [JMAS12a] reported T_g and T_c of melt quenched 45S5 bioglass powder particles of size < 45 μm heated at 15 K minute^{-1} to be 552 °C and 715 °C, respectively. They also observed that T_c increased considerably for coarser (300–500 μm) powder particles. The dependence of the characteristic temperatures on the particle size of melt quenched 45S5 bioglass makes it difficult to make a direct comparison of the characteristic temperatures of the sol-gel and melt quenched glasses. However, the large difference between T_c and T_g observed in the case of the sol-gel glass powders is obvious from the above comparison.

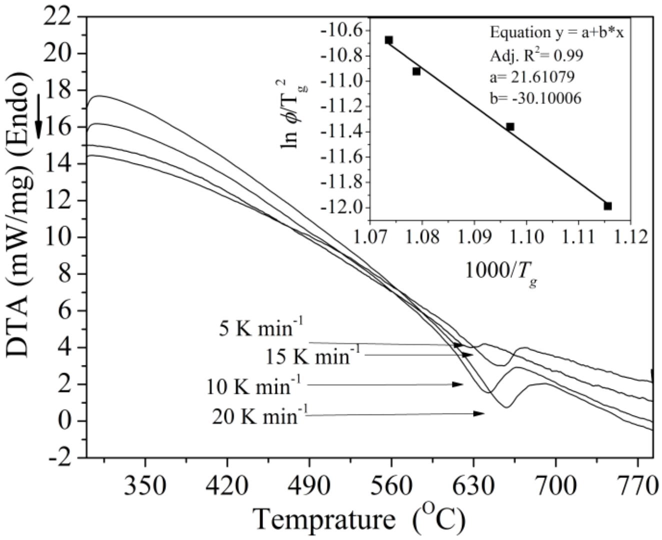

Fig. 4.5: DTA curves recorded at 5, 10, 15, 20 K minute^{-1} near T_g of BG_$(NH_4)_2HPO_4$. Inset shows the Kissinger's plot and the least squares fit to Eq. 2.5 to extract E_K.

Activation energy, which is a measure of the inhibition to the reaction, could be estimated using Kissinger's equation (*cf.* Eq. 2.5). Fig. 4.5 shows the DTA curves of BG_$(NH_4)_2HPO_4$ recorded at constant heating rates of 5 to 20 K minute^{-1}, illustrating the corresponding shift (624 – 661 °C) in T_g with heating rate. Inset in Fig. 4.5 shows the Arrhenius plot corresponding to Eq. (2.5) and the least squares fit to data to extract the activation energy E_K. E_K (= 250 kJ mol^{-1}) obtained can be compared with the values of 316 kJ mol^{-1} [BRET09a] reported for melt quenched 45S5 bioglass powder, which indicates that the sol gel derived glass has relatively better thermal stability.

Since we have a fully amorphous glass in BG_$(NH_4)_2HPO_4$, heat treatment of BG_$(NH_4)_2HPO_4$ will help us in understanding the devitrification

TH-1620_10612107

behaviour of the sol-gel derived 45S5 bioglass. Based on the DTA curves depicted in Fig. 4.5, BG_$(NH_4)_2HPO_4$ was heat treated above its T_g at three different temperature, *viz.*, 650, 750 and 850 °C for 1 h each to induce crystallization and form glass-ceramics. Fig. 4.6 shows the XRD patterns of heat treated BG_$(NH_4)_2HPO_4$ indicating the presence of sodium calcium silicate.

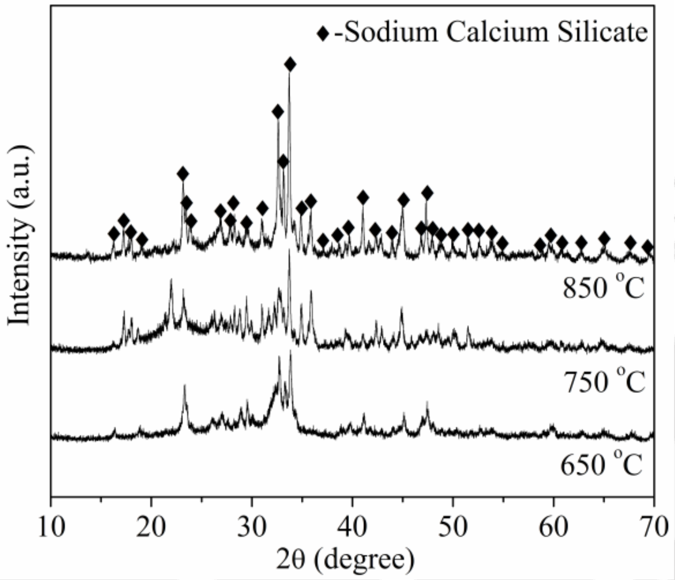

Fig. 4.6: Room temperature XRD patterns of BG_(NH4)$_2$HPO$_4$ heat treated at different temperatures.

It is clear from Fig. 4.6 that $Na_2Ca_2Si_3O_9$ is the only phase crystallizing in the glass heat treated up to 850 °C. Fully developed Bragg peaks and the flat baseline shows that the crystallization of this phase is nearly complete after heat treatment at 850 °C. Reports in the literature show that heat treatment above 600 °C results in the crystallization of $Na_2Ca_2Si_3O_9$ as the main crystalline phase in sol-gel derived Na_2O–CaO–$2SiO_2$ system [ADAM13a, BRET09a, DCCL03a].

Average crystallite size (d_{av}) and microstrain (ε) of $Na_2Ca_2Si_3O_9$ phase in BG_$(NH_4)_2HPO_4$ heat treated at different temperatures have been estimated from the data in Fig. 4.6 using the Williamson-Hall relation (Eq. 2.2) [GKWI52a]. d_{av}

of $Na_2Ca_2Si_3O_9$ increases almost linearly with heat treatment temperature, *i.e.*, from 29 ± 0.05 nm ($\varepsilon = 23 \times 10^{-5}$), 32 ± 0.05 nm ($\varepsilon = 37 \times 10^{-5}$) nm and 38 ± 0.05 nm ($\varepsilon = 45 \times 10^{-5}$) for 650, 750 and 850 °C respectively. Increase in crystallite size due to growth of the crystallites with increase in heat treatment temperature is expected. The continuous increase in ε with increasing temperature is a consequence of the rapid growth of the nanocrystallites within the confined space in the glassy matrix.

4.1.4 *In vitro* bioactivity test

HA forming ability is considered to be a critical factor in facilitating the chemical fixation of biomaterials to bone tissue and ultimately the *in vivo* success of the bone grafting material. BG_$(NH_4)_2HPO_4$ and glass-ceramics obtained by heated treatment of BG_$(NH_4)_2HPO_4$ at 850 °C for 1 h were chosen for *in vitro* bioactivity test. *In vitro* bioactivity test was carried out by soaking both BG_$(NH_4)_2HPO_4$ glass and the glass ceramic pellets in SBF. Structural changes on the surface of the glass and glass-ceramics samples treated in SBF were analysed using GI-XRD (Fig. 4.7 and 4.8). Appearance of crystalline peaks in the GI-XRD patterns of glass samples immersed in SBF for a day or more, confirms the formation of a crystalline layer on the surface of the glass (Fig. 4.7). On soaking in SBF for 3 days, prominent peaks appear at 2θ values of ~26° and ~32°. These peaks correspond to (002) and (211) reflections of HA crystallites. Minor peaks of wollastonite (Calcium silicate) phase were also observed as an intermediate phase during the immersion period.

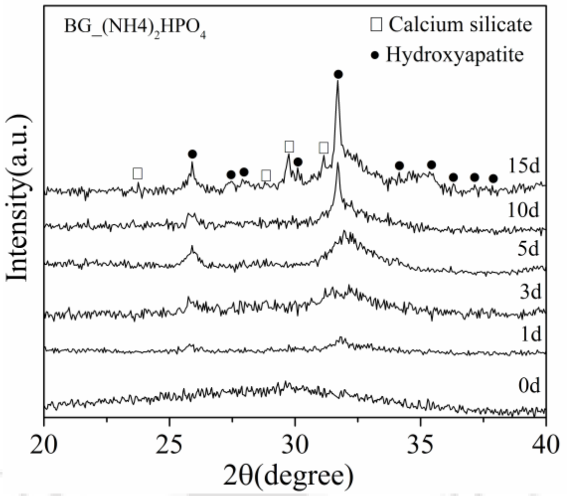

Fig. 4.7: GI-XRD patterns of BG_(NH4)$_2$HPO$_4$ showing the nucleation and growth of HA surface layer as a function of immersion time in SBF.

When bioactive glass/glass-ceramic comes in contact with SBF, a partial dissolution occurs producing an ionic exchange of Ca^{2+} for 2H^{+} within the material network leading to the formation of silanol groups on the surface of the glass/glass-ceramics. Later, there is a partial dissolution of amorphous silica as SiO$_3^{2-}$. This enhances the creation of crystallization nuclei for the Ca–P phase [PADI05a, KOKU06a, OHAN91a].

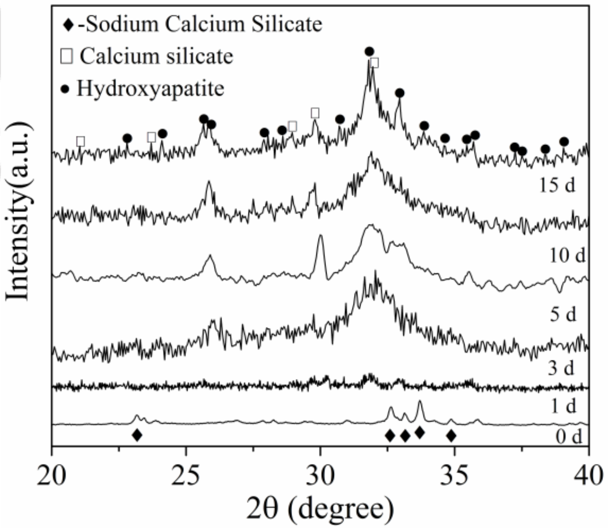

Fig. 4.8: GI-XRD patterns of glass ceramic derived by heat treating BG_(NH4)$_2$HPO$_4$ at 850 °C for 1 h. as a function of immersion time in SBF.

Average size (d_{av}) of HA crystallized was estimated from the (002) reflection at 25.88° peak using the Schërrer`s relation (first term in Eq. 2.2). d_{av} increases from 17 ± 0.5 nm to 41 ± 0.6 nm in glass and from 28 ± 0.5 nm to 52 ± 0.6 nm in glass-ceramic, respectively, after immersion for 3 days to 15 days in SBF. Fig. 4.9 shows that the trends in HA crystallite growth on both glass and glass ceramic with immersion time is almost similar. A rapid increase in HA crystallite size up to 5 days of immersion followed by a slower and linear increase thereafter is seen for both the glass and glass-ceramic samples. In the case of the glass-ceramic sample, consistently higher HA crystallite size suggests an enhanced growth of HA layer on its surface as compared to the glass. The slight increase in the HA crystallite size on ceramic is due to the presence of bone mineral phases at its surface. This confirms the strong bioactive character of the samples which is primarily due to the large amounts of bone mineral phase present in the sample.

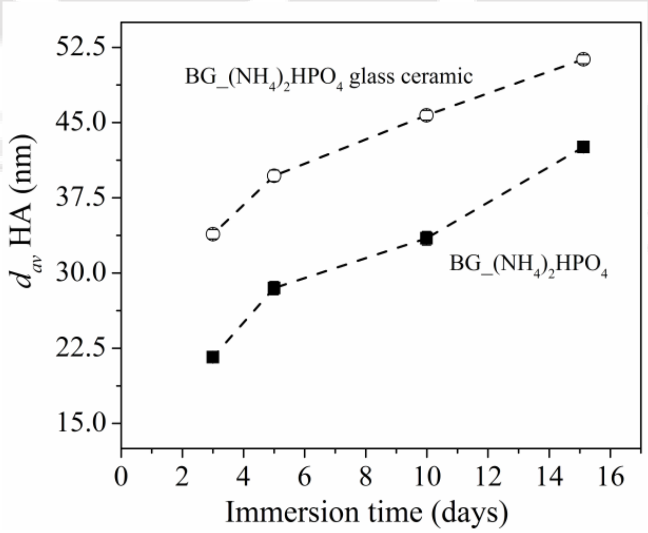

Fig. 4.9: Average crystallite size of HA surface layer on sol-gel derived glass (filled square) and glass-ceramic (open circle) after immersion in SBF.

Preferential growth of HA at different sites on BG_$(NH_4)_2HPO_4$ surface can be observed from FESEM micrographs shown in Fig. 4.10.

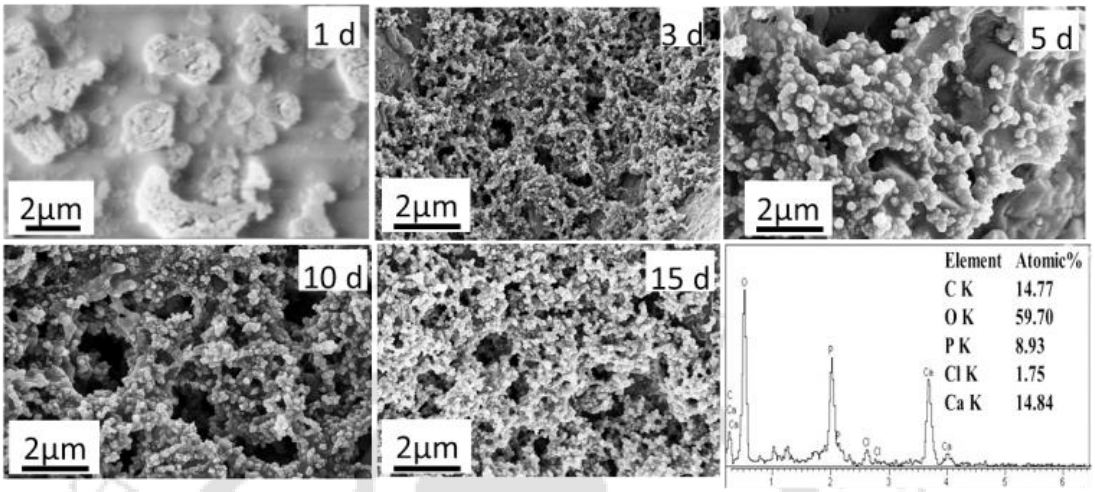

Element	Atomic%
C K	14.77
O K	59.70
P K	8.93
Cl K	1.75
Ca K	14.84

Fig. 4.10: FESEM micrographs of BG_$(NH_4)_2HPO_4$ soaked in SBF for 15 days showing the growth of HA on the surface. EDS spectrum of sample surface after 15 days immersion shows Ca/P molar ratio of 1.66 at.

The micrographs provide visual evidence of gradual development of apatite on the surface of glass after immersion for various time periods in SBF. On immersion for a day, the surface shows agglomerated submicron sized HA particle. After 15 days of immersion, surface of sample is completely covered with HA layer. The EDS spectrum of the surface of sample immersed in SBF for 15 days is also shown in the figure. Na and Cl presence in the HA layer is expected due to their presence in SBF. The value of Ca/P ratio of 1.66 obtained may be compared with the value of 1.67 of HA in human bone.

pH of SBF solution plays a crucial role in deciding the bioactive nature of the specimen. pH variation was recorded to understand the ion exchange mechanism between glass/glass-ceramics surface and SBF as a function of immersion time (*c.f.* Fig. 4.11). Two aspects of pH variation need a careful observation *viz.*, change in magnitude of pH value and rate of change of pH.

Mechanism of HA formation in bioactive silica-based ceramic materials can be described in terms of pH variation of SBF as follows: During early stage of immersion, the reaction is initiated through exchange of H_3O^+ ions from SBF with cations such as Na^+, Ca^{2+} in the sample.

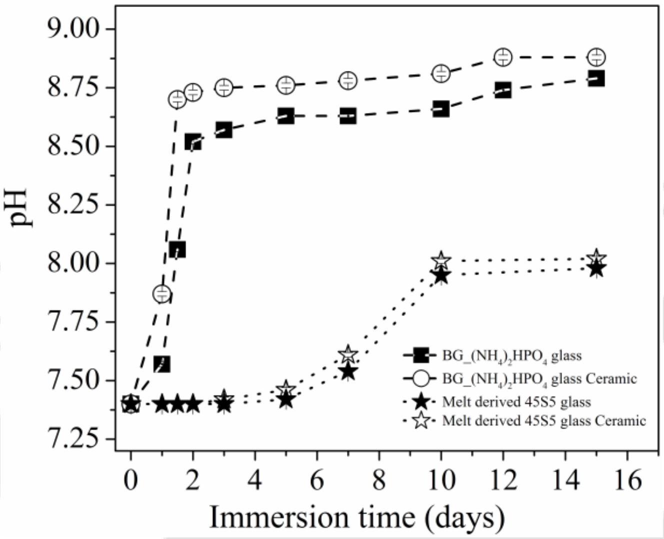

Fig. 4.11: Variation of pH of BG_$(NH4)_2HPO_4$ (filled squares) and glass-ceramic (open squares) as a function of immersion time in SBF. Data on melt derived 45S5 bioglass (filled stars) and glass-ceramic (open stars) are also shown for comparison.

Growth profiles of HA layer on sol-gel and melt derived 45S5 bioglass/glass ceramics are different. Because of higher surface reactivity of sol-gel derived glass/glass-ceramics, a slight increase in pH is observed as early as after 12 h of immersion. Though H_3O^+ ions do not influence the pH of the SBF much, they initiate the necessary hydrolysis reaction. This ion exchange reaction results in the formation of a hydrated silica gel layer. This layer is abundant in silanol (Si-OH) groups and provides favourable sites for calcium phosphate nucleation. Further, water molecules in the SBF react with the Si-O-Si bond to form additional Si-OH groups which induce HA nucleation. Sol-gel derived amorphous and crystalline specimen show faster pH variation whereas no pH variation was observed in case of melt derived specimen in early days of immersion. This is due to the higher roughness of the sol-gel glass/glass-ceramic surface, which facilitates the ion exchange mechanism leading to higher nucleation on the surface and hence rapid formation of HA on the surface. Also, the glass-ceramic specimen contains calcium-rich phase (sodium calcium silicate) on the surface of BG_$(NH_4)_2HPO_4$ which releases of Na^+, Ca^{2+} ions and accelerates HA nucleation by increasing the ionic activity in the fluid. This promotes calcium phosphate nucleation on the surface of sample and a corresponding rapid increase in pH of SBF. This explanation is in line with the bioactive mechanism of bioglass response in SBF proposed earlier [KOKU06a].

High dissolution rate and chemical degradation of sodium calcium phosphate on ceramic surface has been found to promote nucleation and growth of HA layer [KOKU06a]. Further, this higher pH of the SBF solution affects the interfacial reaction kinetics and promotes self-nucleation of HA. Eventually, the surface of the gel-derived 45S5 gets covered with fine HA as seen in the FESEN micrographs (Fig. 4.10) at pH value 8.87 after 15 days of immersion. This study shows that BG_$(NH_4)_2HPO_4$ heat treated at 850 °C for 1 h induces larger and faster ion exchange with SBF, leading to rapid nucleation and growth of HA layer at the surface. However, the BG_$(NH_4)_2HPO_4$ sample shows a lower pH (8.78) due to the time taken for initiation of the ion exchange mechanism. The results presented herein demonstrate that the glass-ceramic derived from BG_$(NH_4)_2HPO_4$ has better bioactivity, as indicated by the pH-time profile to form HA and dissolution rate of sodium calcium silicate, than its melt derived counterpart.

4.2 Nanoporous magnetic bioglass and glass-ceramics

Due to uncontrolled kinetics of the chemical reactions in the sol-gel process, it is difficult to incorporate additives without destroying the amorphous glassy network. Also, it is indeed very rare to find reports of oxide glasses containing small amounts of iron oxide which exhibit strong magnetic behaviour and there are no reports in the literature of fully amorphous bioglass compositions containing iron oxide exhibiting significant magnetic behaviour. Magnetic bioglass-ceramics which are bioactive as well as magnetic, serve a variety of biomedical applications as mentioned in the first chapter A thorough understanding of sol-gel chemistry and successful synthesis of fully amorphous 45S5 bioglass propelled us to develop a sol-gel procedure for synthesis of a magnetic bioglass whose composition is that of Hench's 45S5 bioglass with a small percentage (2 and 3 wt.%) of Fe_2O_3 substituted for SiO_2.

4.2.1 Sol-gel synthesis of magnetic bioglass

The modified sol-gel procedure adopted to prepare magnetic bioglass is depicted in Fig. 4.12 as a flow chart. The flow chart shows that the sol-gel procedure adopted is the same as the one in Fig. 2.2(a) until the step involving the addition of the phosphate precursor. After this, the precursor for iron oxide, *viz.*, $Fe(NO_3)_3.9H_2O$ is added to the sol containing Tetraethyl orthosilicate (TEOS), Calcium nitrate tetrahydrate ($Ca(NO_3)_2.4H_2O$), sodium nitrate ($NaNO_3$) and di-ammonium hydrogen orthophosphate $(NH_4)_2HPO_4$. Concentration of TEOS and ferric nitrate were adjusted to yield a final composition of $24.5CaO.(45\text{-}x)SiO_2.6P_2O_5.24.5Na_2O.xFe_2O_3$ with $x = 2$ and 3 Fe_2O_3 wt.% designated as BG_Fe_2 and BG_Fe_3. BG_Fe_2 was also heat treated at 850 °C for 1 h to yield sol-gel based bioglass-ceramics designated as BC_Fe_2.

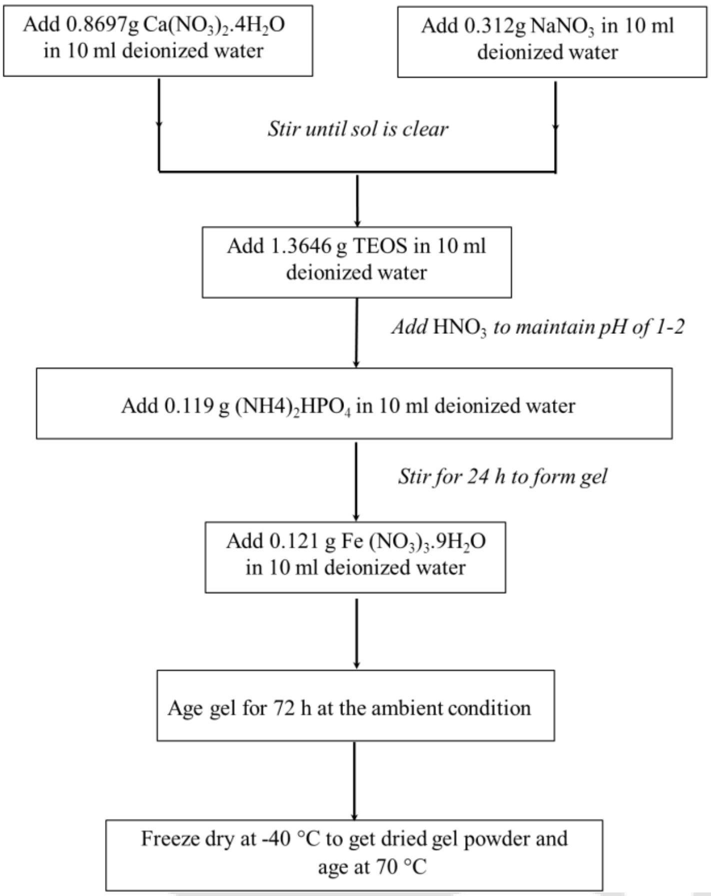

Fig. 4.12: Sol-gel procedure adopted to prepare 45S5 bioglass containing 2 wt% Fe_2O_3.

4.2.2 Structural characterization

Fig. 4.13 shows the XRD patterns of BG_Fe_2, BG_Fe_3 and BC_Fe_2 powders recorded at room temperature. XRD pattern of BG_Fe_2 shows the typical features of a completely amorphous material, *viz*., a broad hump with no perceptible crystalline reflections. However, XRD pattern of BG_Fe_3 shows the presence of strong crystalline (Bragg) reflections superposed on an amorphous background. On the other hand, XRD pattern of BC_Fe_2 reveals strong crystalline reflections which could be indexed to sodium calcium silicate and a magnetic iron oxide phase. Magnetic nature of the glass-ceramic BG_Fe_3 sample (as discussed later in section 4.2.4) is due to the presence of this iron oxide phase. Hence, iron oxide phase can exist either as ferrimagnetic maghemite (γ-Fe_2O_3) [PDF # 39-1346 or ferrimagnetic magnetite (Fe_3O_4) in the glassy matrix the third stable iron oxide phase *viz.*, α-Fe_2O_3 is antiferromagnetic [STLI59a] and hence cannot contribute to the observed magnetization in BG_Fe$_2$. Though it is difficult to distinguish these two iron oxide phases due to the close proximity of their Bragg peak positions, it is more likely that the maghemite (γ-Fe_2O_3) phase of iron oxide is present in the as-prepared sol-gel powders due to the low (70 °C) processing temperature involved in the synthesis. Since, BC_Fe$_2$ was obtained by heat treatment of BG_Fe$_2$ at 850 °C inside a closed furnace under a reducing environment one expects the magnetic γ-Fe_2O_3 present in BG_Fe$_2$ to reduce into magnetite (Fe_3O_4). It has been clarified that heat treatment of melt quenched glasses containing Fe_2O_3 at elevated temperature in a closed furnace results in the formation of glass-ceramics with Fe_3O_4 [RKSI08b]. These conclusions drawn will also be justified with temperature dependent magnetization data to be discussed later in this section.

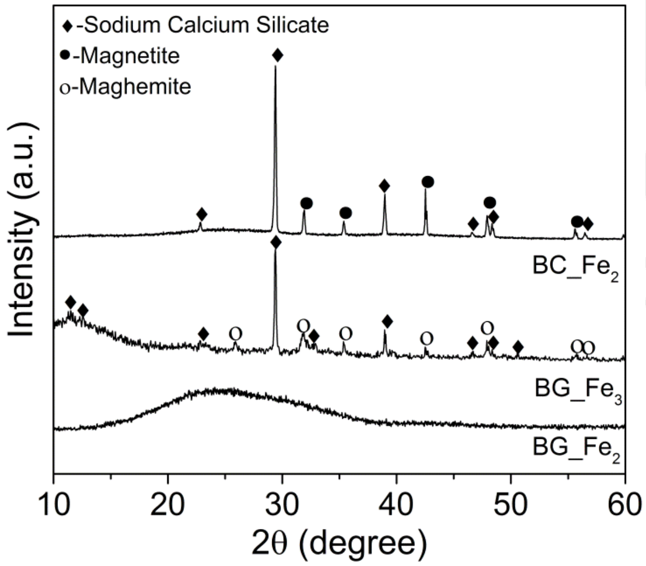

Fig. 4.13: Room temperature XRD patterns of BG_Fe$_2$, BG_Fe$_3$ and BC_Fe$_2$ powders.

Volumetric fraction of $Na_2Ca_2Si_3O_9$ and magnetic phase (γ-Fe_2O_3 or Fe_3O_4)

present in BG_Fe$_3$ and BC_Fe$_2$ can be estimated from the normalized XRD patterns by calculating the ratio of the integrated area under the primary diffraction peak of individual crystalline phases by the procedure explained in in chapter 2. The ratio $Na_2Ca_2Si_3O_9$:γ-Fe_2O_3 and $Na_2Ca_2Si_3O_9$:Fe_3O_4 estimated for BG_Fe$_3$ and BC_Fe$_2$ are 90.5:9.5 and 90:10, respectively. Broadened Bragg reflections (*cf.* Fig. 4.13) signify that the crystalline phases in BC_Fe$_2$ are composed of nanocrystallites. Average crystallite size (d_{av}) of the two nanocrystalline phases present in BG_Fe$_3$ and BC_Fe$_2$ was estimated using Williamson - Hall relation (Eq. 2.2). d_{av} (ε) of sodium calcium silicate and maghemite phases in BG_Fe$_3$ are 39 ± 0.05 nm (18×10^{-6}) and 22 ± 0.05 nm (20×10^{-6}), respectively. d_{av} (ε) of sodium calcium silicate and magnetite phases in BC_Fe$_2$ is 49 ± 0.05 (20×10^{-6}), and 38 ± 0.07 nm (19×10^{-6}), respectively.

In order to confirm the amorphous nature of BG_Fe$_2$ down to atomic length scales, HRTEM images were taken and analyzed. HRTEM image shown in Fig. 4.14(a) corresponds to BG_Fe$_2$, and the inset in the figure shows the FFT image of the circled region in Fig. 4.14(a). Fig. 4.14 (b) shows the EDS spectrum and overall concentration of elements present in BG_Fe$_2$. There is clear evidence for the existence of nanocrystalline regions in the HRTEM image of BC_Fe$_2$ depicted in Fig. 4.14(c). SAED pattern (inset in Fig. 4.14(c)) shows the diffraction pattern of the glass-ceramic sample of BC_Fe$_2$, The crystalline spots in the SAED pattern could be indexed to reflections from the (220), (311) and (400) planes of magnetite. Fig. 4.14(d) displays the FFT of HRTEM image which shows lattice fringes corresponding to nanocrystalline regions present in the amorphous matrix. Interplaner (d_{hkl}) spacing of 0.253 nm estimated from the FFT profile corresponds to that of (311) plane of magnetite.

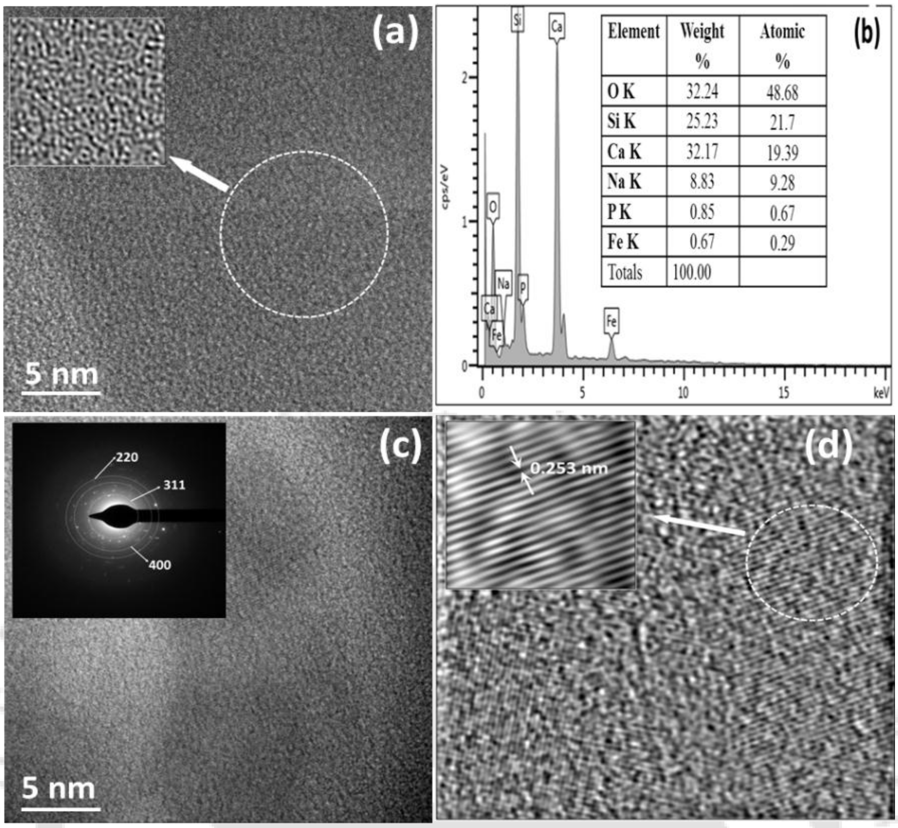

Element	Weight %	Atomic %
O K	32.24	48.68
Si K	25.23	21.7
Ca K	32.17	19.39
Na K	8.83	9.28
P K	0.85	0.67
Fe K	0.67	0.29
Totals	100.00	

Fig. 4.14: HRTEM image of BG_Fe$_2$ (Inset shows FFT image of the circled region). (b) EDS spectrum with overall elemental composition map of BG_Fe$_2$. (c) HRTEM image of BC_Fe$_2$ (inset shows the SAED pattern corresponding to diffraction from a magnetite crystallite). (d) FFT HRTEM image of BC_Fe$_2$ (inset shows expanded view of the marked crystalline region).

Measured elemental compositions (Fig. 4.14 (b)) of Si (= 21.7 at.%), Ca (= 19.39 at.%), Na (= 9.28 at.%), P (= 0.67 at.%), Fe (= 0.29 at.%) and O (= 48.68 at.%) can be compared with the nominal composition of bioglass 45S5 with 2 wt% Fe_2O_3 substituted for SiO_2, *viz.*, Si (= 20.86 at.%), Ca (= 19.49 at.%), Na (= 9.15 at.%), P (= 0.57 at.%), Fe (= 0.28 at.%) and O (= 49.65 at.%). The close agreement between the measured and nominal elemental compositions shows that the specimen has a composition very close to 45S5 with 2 wt.% Fe_2O_3 substitution for SiO_2.

4.2.3 Thermal properties

Fig. 4.15 shows the DSC curve of BG_Fe_2 recorded at a constant heating rate of 20 K minute^{-1}, illustrating an endothermic baseline shift at 649 °C followed by two exothermic crystallization peaks (T_c's) at 855 °C and 889 °C. The endothermic baseline shift in Fig. 4.15 signifies the glass transition, whose onset temperature is considered as the glass transition temperature (T_g). T_c at 855 °C corresponds to the crystallization temperature of magnetite and the other at 889 °C corresponds to the crystallization of the bone mineral phase sodium calcium silicate. The observed T_g of BG_Fe_2 is lower than that of melt derived counterpart (656 °C) [RKSI09a].

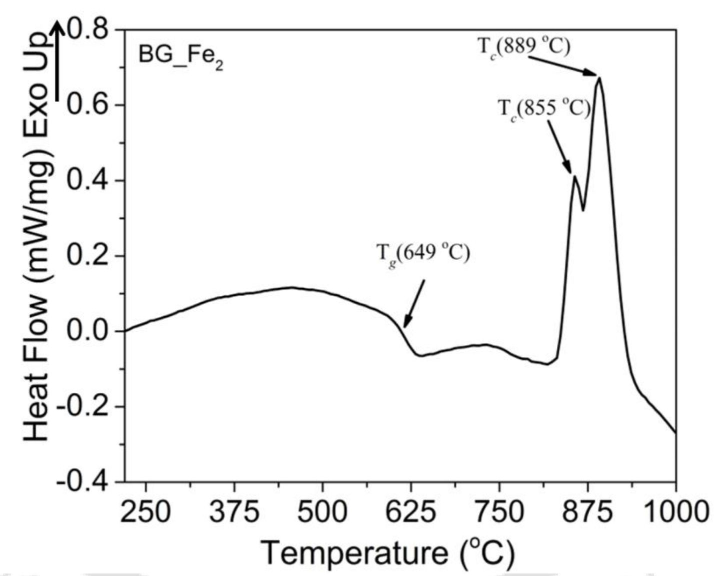

Fig. 4.15: DSC curve of BG_Fe_2 recorded at a constant heating rate of 20 K minute^{-1}.

It may be noted that bone mineral phases, wollastonite and HA crystallize along with magnetite when melt quenched glass of the same composition is subjected to heat treatment above T_g [RKSI08c]. But, in the case of sol-gel derived glass, magnetite crystallizes first followed by the bone mineral phase sodium calcium silicate as shown in this work. The reason for this is the lower T_c of sodium calcium silicate as compared to wollastonite. This is the major difference observed in the devitrification behaviour of melt quenched and sol-gel derived glasses of same nominal composition.

4.2.4 Magnetic properties

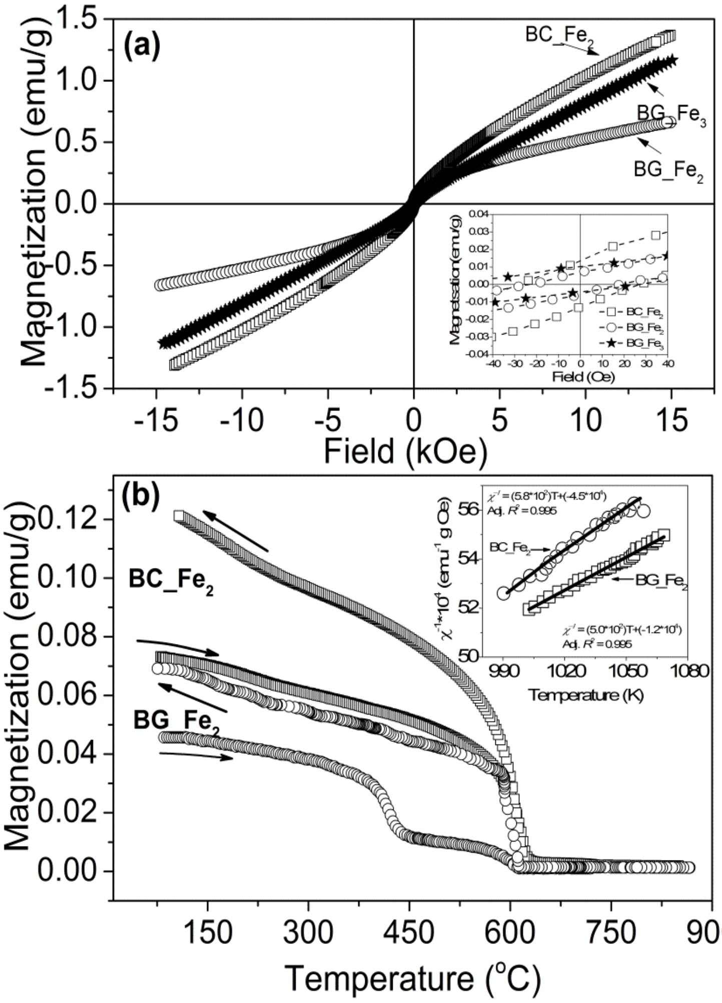

Fig. 4.16: (a) Room temperature *M-H* curves of BG_Fe$_2$, BG_Fe$_3$ and BC_Fe$_2$. Inset shows an expanded view of data close to the origin. (b) *M-T* curves of BG_Fe$_2$ and BC_Fe$_2$ recorded during heating and cooling cycles under an applied field of 1 kOe. Inset shows the linear fits to χ^{-1}-T data of BG_Fe$_2$ and BC_Fe$_2$ recorded above their T_C.

The most striking result obtained in this study is the spontaneous magnetization exhibited by the sol-gel derived glass powder (BG_Fe$_2$). It is obvious from the *M-H* data shown in Fig. 4.16 (a) that none of three samples show magnetic saturation up to an applied magnetic field of ±15 kOe, which is the typical behaviour of samples containing small amounts of ferrimagnetic phase. Inset in the figure gives an expanded view of data close to the origin. Table 1 lists the magnetic parameters of different sol-gel derived powders extracted from Fig. 4.16(a).

Table 4.1: Magnetization at 15 kOe ($M_{s(15kOe)}$), remanent magnetization ($M_{r(15kOe)}$), coercivity (H_c) and hysteresis loop area (A_{Hys}) for ±15 kOe sweep, and percentage of magnetic phase in BG_Fe$_3$ and BC_Fe$_2$ samples.

Magnetic parameters	**BG_Fe$_2$**	**BG_Fe$_3$**	**BC_Fe$_2$**
$M_{s(15kOe)}$ (emu/g)	0.66	1.16	1.36
$M_{r(15kOe)}$ (emu/g)	0.017	0.021	0.027
Coercivity (H_c)	21	45	33
Loop area (A_{Hys}) (erg/g)	33.25	120.34	139.94
% of magnetic phase	-	0.15	0.16

It should be noted that such nonlinear magnetic behaviour exhibited by BG_Fe$_2$ in Fig. 1.16(a) is quite uncommon for a glassy material which lacks long range structural order. To understand the origin of significant magnetization observed in amorphous BG_Fe$_2$, one has to note that unlike melt quenched glasses; sol-gel derived glasses have highly porous structure. The microstructure of sol-gel derived glasses depends strongly on the hydrolysis and condensation reactions. A number of processing conditions can influence the hydrolysis and condensation reactions. Of these, the most prominent ones are water-to-alcoxide ratio, type and amount of catalyst, type of organic group attached to the silicon atom and solvent effect [CBRI90a]. Sol-gel involves highly pH sensitive reactions that can be processed under basic and acidic environments. Several pH-dependent rate profiles have been reported for the hydrolysis and condensation reactions which clearly indicate that the reaction rates are strongly dependent on pH [RWJO89a, CBRI90a]. BG_Fe$_2$ has a highly disordered glassy structure containing iron oxide clusters of different sizes (and hence different magnetic moments) whose position and easy axis of orientation are randomly distributed. Hence, the sites these iron oxide clusters can occupy are randomly positioned. If the iron oxide clusters occupy the pore volumes present in the sol-gel glass, interaction between iron ions is possible. Interaction between the magnetic ions in the nanoclusters distributed in the pore volumes of the glass can result in long-range magnetic interaction within the sample. It has been pointed out [CMHU82a] that such micromagnetic type behavior can lead to long range magnetic interaction in a glassy matrix as observed in BG_Fe$_2$.

Fig. 4.16 (b) shows the M-T curves of BG_Fe$_2$ and BC_Fe$_2$ samples recorded under heating and cooling cycles with an applied field of 1 kOe. A steady decrease in magnetization is observed as the temperature is increased from the ambient. The glass sample (black symbols) shows lower magnetization (0.045 emu/g) at room temperature, which decreases to zero as the temperature is increased to 850 °C, signifying the transition to the paramagnetic state. Two magnetic transitions, one at 440 °C (corresponding to T_C of maghemite) and the other at 622 °C (corresponding to T_C of magnetite), are observed in M-T curve of BG_Fe$_2$ recorded during the heating cycle. However, cooling curve of BG_Fe$_2$ shows only one transition corresponding to that of magnetite. This confirms the presumption made in section 4.2.2 about the magnetic content in BG_Fe$_2$. It is now clear that BG_Fe$_2$ contains iron oxide in the form of maghemite (γ-Fe_2O_3), which transforms into magnetite when heated beyond 440 °C. On the other hand, the M-T curve of BC_Fe$_2$ shows only one transition at 602 °C in the heating cycle which again confirms that the glass-ceramic sample contains iron oxide in the form of magnetite. The higher magnetization of the thermally cycled samples is due to the increase in the amount and average crystallite size of magnetite.

Maghemite is a ferrimagnetic mineral with a structure essentially similar to magnetite (Fe_3O_4) and chemical composition similar to hematite (α-Fe_2O_3) [CJSE04a]. Due to their similar crystal structure, maghemite and magnetite have similar magnetic properties, with the former having a lower thermal stability [XMLI10a]. Hence, maghemite has a lower Curie temperature (T_C) than magnetite. Reports in the literature show that T_C of maghemite can vary widely from 250 °C to 350–900 °C [CJSE04a]. This disparity in the reports could be attributed to various factors such as purity, method of preparation and thermal history, *etc*.

Magnetic susceptibility (χ) of BG_Fe$_2$ and BC_Fe$_2$ above T_C in the paramagnetic regime is expected to follow the Curie-Weiss law (Eq. 2.6). Inset in Fig. 4.16 (b) shows the χ^{-1}–T data corresponding to BG_Fe$_2$ and BC_Fe$_2$ for T > T_C. Inset shows the linear behaviour of χ^{-1}–T data in the temperature range of 677 °C –777 °C (950 – 1050 K) as predicted by Curie-Weiss law. θ_p (C_M) values calculated from intercept (slope) for BG_Fe$_2$ for BG_Fe$_2$ and BC_Fe$_2$ are -37.4 K (0.0017 emu KOe^{-1}mole^{-1}) and -77.7 K (0.0020 emu KOe^{-1}mole^{-1}), respectively. The negative value of θ_p confirms the ferrimagnetic nature of both the samples, indicating the presence of ferrimagnetic magnetite.

Amount of magnetic phase present in these sample was estimated from the ratio of measured magnetic moment ($M_{s)15\ kOe)}$) of the sample to the magnetic moment of magnetic phase *i.e.*, magnetite (M_s = 92 emu/g [RDCU72a]) or maghemite (M_s = 74 emu/g [CJSE04a]). Accordingly, percentage of maghemite and magnetite present in BG_Fe$_3$ and BC_Fe$_2$ turn out to be 0.15 and 0.16, respectively.

EPR absorption (derivative) spectra of BG_Fe$_2$ and BC_Fe$_2$ are shown in Fig. 4.17. EPR absorption at $g \approx 4.3$ is characteristic of isolated Fe^{3+} (3d^5, $^6S_{5/2}$) ions distributed in different sites and the one at $g \approx 2.1$ is attributed to those ions which interact by superexchange coupling [KOMA08a, DWMO75a].

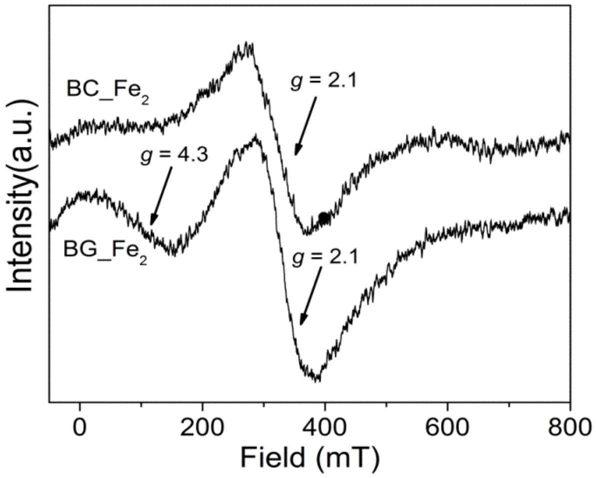

Fig. 4.17: EPR spectra of BG_Fe_2 and BC_Fe_2 powders.

Fe^{2+} ions are not involved in EPR absorption but their interaction with Fe^{3+} ions influences the characteristics of the absorption lines [KOMA08a, DWMO75a, MNOF90a, RAO95a]. g ≈ 2.1 resonance is present in both the glass and glass-ceramic samples, whereas the absorption line at g ≈ 4.3 is not observed for BC_Fe_2. Presence of both the absorption lines in BG_Fe_2 indicates that both Fe^{2+} and Fe^{3+} ions are present in both isolated as well as clustered manner in the porous amorphous matrix. The magnetic behaviour exhibited by BG_Fe_2 reflects the presence of long range (ferri) magnetic interaction between these iron ions. Two types of interactions can exist in a glassy system containing Fe_2O_3 network modifiers, *viz.*, dipole-dipole and superexchange type interactions [KOMA08a]. Both these interactions are structure sensitive and are due to the presence of both Fe^{2+} and Fe^{3+} ions. Both the iron ions occupy two types of sites with different coordinations. Fe^{2+} generally occupies octahedral sites. Absence of the g ≈ 4.3 absorption line in BC_Fe_2 indicates a decrease in low symmetry sites of Fe^{3+} ion and the formation of Fe ion clusters. EPR parameters, *viz.*, absorption line intensity (J) and linewidth (ΔH) of EPR absorption profile of the samples define the environment around the Fe ions. Both J and ΔH of $g \approx$

2.1 absorption line increases from $J = 49.1 \times 10^6$ and $\Delta H = 99 \times 10^{-3}$ T for BG_Fe$_2$ to $J = 123 \times 10^6$ and $\Delta H = 244 \times 10^{-3}$ T for BC_Fe$_2$. Increase in J value of $g \approx$ 2.1absorption signifies the predominance of clustering mechanism in BC_Fe$_2$.

4.2.5 *In vitro* bioactivity test

In-vitro bioactivity test was carried out by soaking BG_Fe$_2$ and BC_Fe$_2$ pellets in simulated body fluid (SBF). SBF was prepared according to the procedure discussed in chapter 2 (section 2.2.5) Fig. 4.18 (a) and (b) show the GI-XRD patterns of BG_Fe$_2$ and BC_Fe$_2$ immersed in SBF for 15 days. It is clear from the figures that HA layer formation follows the same trend as in the case of BG_Fe$_2$ and BC_Fe$_2$ immersed in SBF. It can also be seen from the two figures that a surface layer forms after 1 day of immersion in SBF, which gradually develops into a crystalline HA layer after 15 days of immersion. A closer look at Fig. 4.18(b) would reveal a comparatively rapid growth of HA layer on BC_Fe$_2$ due to the presence of bone mineral crystallites at its surface.

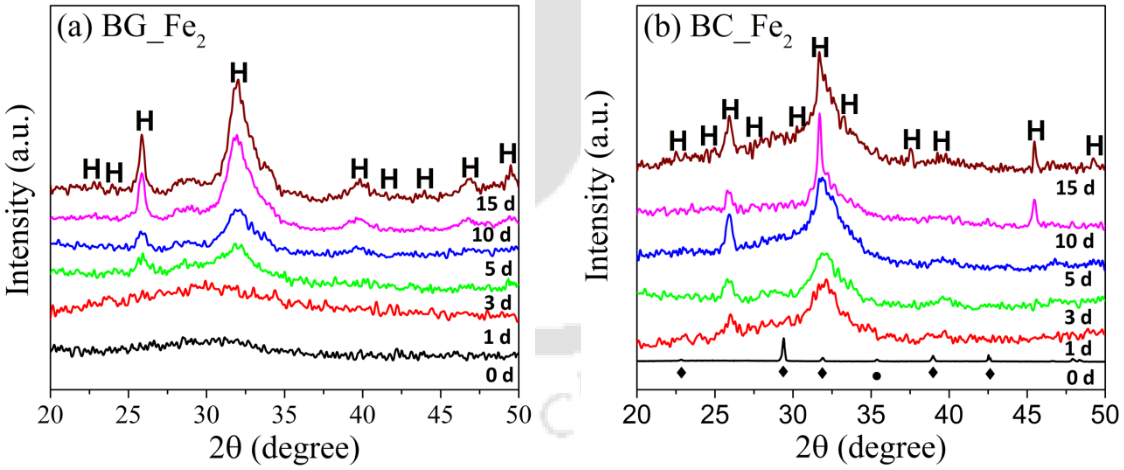

Fig. 4.18: GI-XRD patterns of (a) BG_Fe$_2$ and (b) BC_Fe$_2$ soaked in SBF.

Fig. 4.19 depicts the subtle differences in the growth of the HA layer on BG_Fe$_2$ and BC_Fe$_2$ by showing the variation of average crystallite size of HA as a function of immersion time. The rapid increase in the crystallite size, especially at early hours of immersion on the surface of BC_Fe$_2$ indicates the strong bioactive character of the glass-ceramic sample which is primarily due to the large amounts of bone mineral

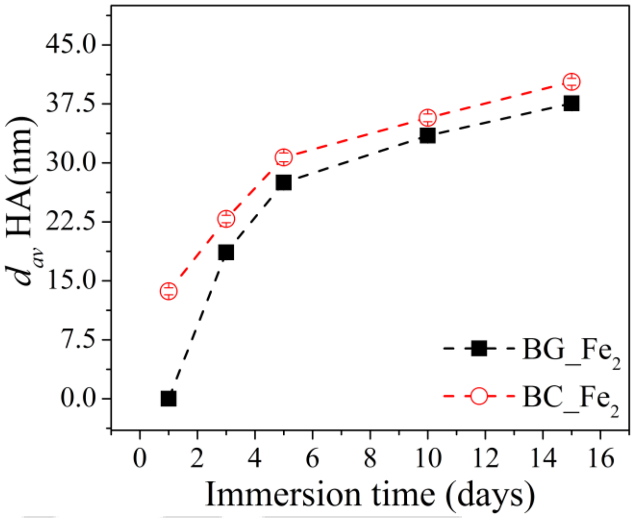

Fig. 4.19: Average crystallite size of HA surface layer on BG_Fe$_2$ (filled squares) and BC_Fe$_2$ (unfilled circles) after immersion in SBF.

phase present in the sample. d_{av} of HA crystallized was estimated from the (002) reflection at 25.88º peak using the Schërrer`s relation (first term in Eq. 1). d_{av} increases from 18 ± 0.56 nm to 37 ± 0.42 nm in the case of BG_Fe$_2$ and from 22 ± 0.46 nm to 40 ± 0.44 nm in the case of BC_Fe$_2$, as the immersion time in SBF is increased from 3 days to 15 days. Mechanism of HA formation in bioactive silica-based ceramic materials was discussed in section 4.1.4. Fig. 4.20 shows that upon immersion of sol-gel derived BG_Fe$_2$ and BC_Fe$_2$ pellets in SBF, its pH increases more rapidly than bulk melt-quenched samples (Ref_BG and Ref_BC) investigated earlier [AKSR12a]. The significant increase in pH in first few hours of immersion of BG_Fe$_2$ and BC_Fe$_2$ pellets is to be noted. This rapid change in pH can be understood in terms of ion exchange mechanism between the sample and SBF, leading to HA layer formation. pH increases from 7.40 to 7.53 in just 12 h of immersion of the sol-gel derived samples (*cf.* Fig. 4.20) it took 3 days to achieve the same by the melt quenched counterparts [DARC03a]. This is due to the rapid dissolution of sodium calcium silicate crystallites, which facilitates faster precipitation and formation of the HA layer on the surface of the sol-gel derived specimens. This observation is in agreement with an earlier report [DARC03a] which demonstrated that silanol group formation and silicon dissolution in

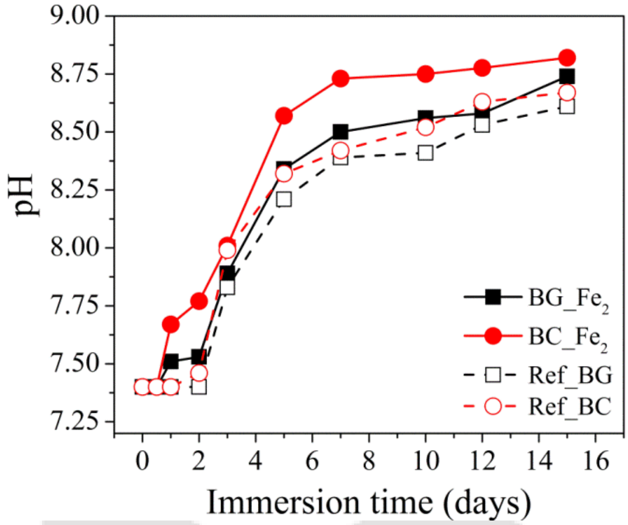

Fig. 4.20: Variation of pH as a function of immersion time of BG_Fe$_2$ and BC_Fe$_2$ in SBF. Data on melt derived counterparts Ref_BG and Ref_BC extracted from [AKSR12a] are also shown for comparison.

SBF is higher in sol-gel derived 58S (58 SiO_2, 33 CaO and 9 P_2O_5 wt.%), 68S (68 SiO_2, 23 CaO and 9 P_2O_5 wt.%), 77S (77 SiO_2, 14 CaO and 9 P_2O_5 wt.%) and 91S (91 SiO_2 and 9 P_2O_5 wt.%) glasses than melt quenched glasses 45S5 and 60S (60 SiO_2, 17 CaO, 17 Na_2O and 6 P_2O_5 wt.%). The HA layer formation mechanism is the same for both glass and glass ceramic. However, the pH of the medium reaches saturated value of 8.5 in the case of BG_Fe$_2$ after immersions for 3 days, whereas a saturated pH value of 8.7 was attained in the case of BC_Fe$_2$ after 3 days of immersion. This indicates that the ion exchange mechanism is more rapid in sol-gel derived glass/glass ceramics as compared to melt quenched counterparts (*cf.* Fig. 4.20), mainly because of the larger surface area of the sol-gel derived samples.

4.3 Summary

- Our attempts showed that with $(NH_4)_2HPO_4$ as the phosphate precursor, it is possible to obtain fully amorphous bioglass 45S5 by sol-gel route.
- This study makes a significant impact on the debate on the relative merits of sol-gel and melt derived glass/glass ceramic. Sol-gel derived samples exhibit superior bioactivity as compared to the bulk melt derived counterparts.
- Magnetic bioactive glass with composition close to that of bioglass 45S5 with 2 wt% iron oxide substitution was successfully synthesized by sol-gel route for the first time.
- The novelty of this sol-gel product stems from the magnetic interaction of homogenously dispersed iron oxide nanoclusters within the porous glassy matrix which induces spontaneous magnetization in it.
- Advantages such as porous structure and the ability to form nanocomposites provide distinct advantage for these sol-gel products in biomedical applications.
- Since this methodology allows for production of materials with controlled stoichiometry and particle size, it can be applied for large production of biomaterials for potential applications such as bone implant and bone scaffolds.
- This work reported is limited to demonstration of a novel magnetic sol-gel glass with iron load capacity of 2 wt%. Ways to incorporate larger amount of iron oxide in the glass has to be explored to obtain higher magnetization required for applications such as hyperthermia treatment of cancer.

Chapter 5

Investigations on electrospun fibrous membranes

The first section of this chapter discusses the preparation and characterization of PVA-PVP membranes for wound care application and the second section describes the synthesis of osteoconductive scaffolds for bone regeneration fabricated by combining sol-gel and electrospinning processes.

5.1 Electrospun PVA-PVP nanofibrous membranes

Interactive wound closure is a relatively new concept which involves dressings which not only protect the wound but also interact with cellular environment during the wound healing process. Interactive wound dressings work on the principle of wound management. They absorb excess exudate and prevent the wound from desiccation, provide a barrier to bacteria and minimize contamination of the wound, apart from being free of toxic particulate components. By maintaining a moist environment, interactive dressings decrease dehydration and cell death [SUJA12a, KEAS98a]. Water soluble PVP known for its hydrophilicity, biodegradability and biocompatibility is a natural choice to fabricate antimicrobial wound dressing. But, the highly hygroscopic PVP is unsuitable for electrospinning. On the other hand, PVA is a synthetic

TH-1620_10612107

biocompatible polymer with excellent physicochemical and mechanical properties, which can be electrospun. Since PVA and PVP have similar functional group, they can be easily cross-linked. This section is focused on preparation and characterization of simple PVA-PVP nanofibrous membranes for use as interactive, antibiotic eluting wound dressing materials.

5.1.1 Preparation

Nanofibrous membranes of water soluble PVA (MW ~80000 g/mol) and PVP (MW ~40000 g/mol) were prepared using electrospinning technique after optimizing solution and process parameters. Ikeda *et al.* [IKED86a] showed that polymers in the MW range of 1.4×10^4 Da to 9.4×10^4 Da exhibit optimal antimicrobial activity. Bearing this in mind, we chose PVA of MW ~80000 g/mol and PVP of MW ~40000 g/mol so as to have a good control of the viscosity and electrical conductivity of the blended polymer solutions. Best blending was obtained when 8 % w/v aqueous PVA solution was mixed with 20% w/v aqueous PVP solution under stirring at room temperature. Three sets of homogeneously blended PVA:PVP solutions with weight ratios of 100:0, 90:10 and 75:25 were used for electrospinning the following membranes: (i) 100% (8% w/v) PVA, (ii) PVA:PVP ratio of 90:10, and (iii) PVA:PVP ratio of 75:25. They were designated as PVA_{100}:$PVP_{0,}$ PVA_{90}:PVP_{10} and PVA_{75}:PVP_{25}, respectively. Attempts to prepare membranes with higher PVP content were not successful.

Table 5.1: Viscosity and electrical conductivity of aqueous PVA:PVP solutions.

Solution constitution 8%w/v PVA:20%w/v PVP	**Viscosity (cP)**	**Electrical conductivity (µS)**
0:100	14	289
75:25	114	606
90:10	223	424
100:0	249	189

5.1.2. Structure and morphology

FESEM images of the composite fibrous membranes shown in Fig. 5.1 indicate homogenous and interconnected fibrous network with no beads or string formation. Hybrid polymeric fibers obtained from PVA-PVP solutions appeared more entangled.

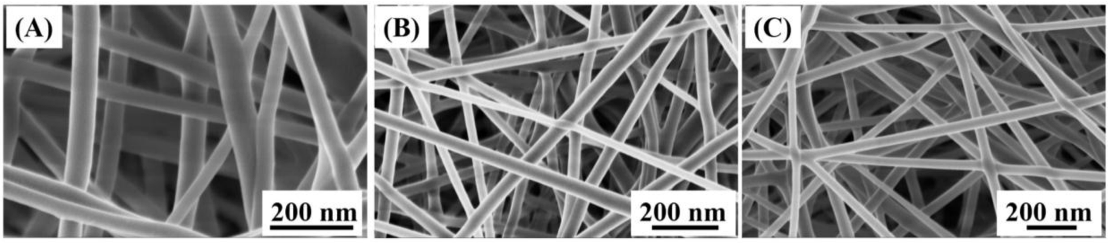

Fig. 5.1: FESEM images of (A) PVA_{100}:PVP_0, (B) PVA_{90}:PVP_{10} and (C) PVA_{75}:PVP_{25} membranes showing fibrous morphology.

Average diameter of the individual fibers was estimated from multiple FESEM images using ImageJ software. The diameter for each sample reported is the mean of at least 80 independent measurements. Average diameter of the fibers was estimated to be 107, 103 and 84 nm in PVA_{100}:PVP_0, PVA_{90}:PVP_{10} and PVA_{75}:PVP_{25} membranes, respectively. ES process is strongly influenced by MW of the solvent, electrical conductivity of the solution and viscosity of the solution. With increasing PVP content, electrical conductivity of solutions increases and viscosity reduces as depicted in Table 5.1, which are responsible for the observed decrease in fiber diameter. Increase in solution conductivity tends to increase the deposition area of fibers due to increase in the trajectory of the polymer jet. This stretches the fibers and makes them narrower. Besides this, viscosity determines the extent of entanglement of polymer molecule chains within the solution [RAMA05a]. PVA (MW ~80000 g/mol) and blended solutions of PVA:PVP with PVP content up to 25 % had appropriate viscosity to maintain continuous jet stream during ES. Electrical resistance of the polymer solution decreases because of the lower viscosity of PVA_{90}:PVP_{10} and PVA_{75}:PVP_{25}, which favours the formation of fibers with lower diameters.

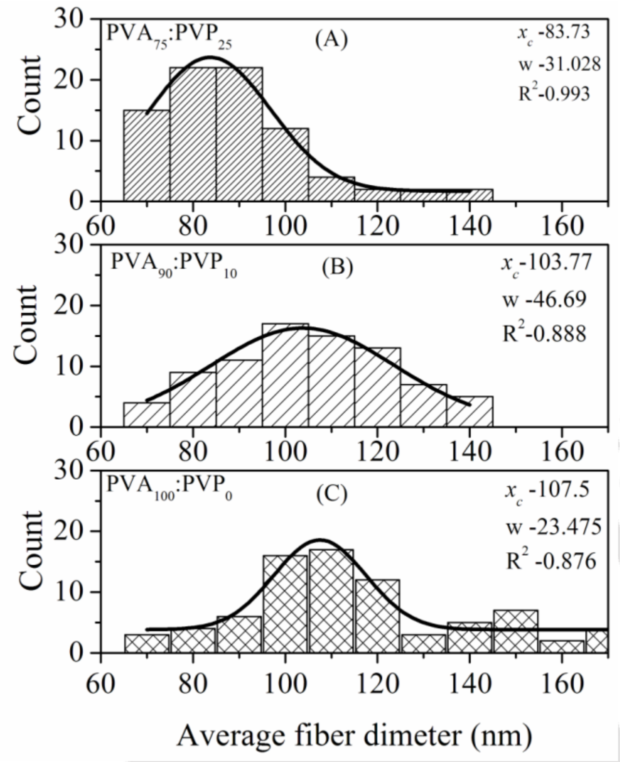

Fig. 5.2: Fiber diameter distributions in (A) PVA_{75}:PVP_{25}, (B) PVA_{90}:PVP_{10} and (C) PVA_{100}:PVP_{0} membranes (x_c (nm) is the mean, w (nm) is the width and R^2 is a measure of the goodness of the Gaussian fit to data).

Fig. 5.3 shows the XRD patterns of the three different membranes (*cf.* section 2.2.1.1). PVA is a semi-crystalline polymer whose crystalline nature results from the strong intermolecular interaction between PVA molecular chains through hydrogen bonding. Semi-crystalline PVA usually displays XRD peaks centered at $2\theta = 11°$ (100), 19.8° ($10\bar{1}$), 22.9° (200) and 40.6° (unassigned) [NRAJE13a, UMAS14a]. The broadened peaks exhibited by PVA_{100}:PVP_{0} membrane can be attributed to the 1-d nanostructure of the electrospun membrane and the poor crystallinity of the rapidly solidified liquid polymer jets. On the other hand, PVP is an amorphous polymer which exhibits two very broad humps between $2\theta = 11°–15°$ and 19°–24°. It is evident from Fig. 5.3 that the XRD pattern of PVA_{90}:PVP_{10} and PVA_{75}:PVP_{25} membrane reveal broad humps located at $2\theta = 11°$ and 22°. The overlap of PVP and PVA peaks results in the broad peak in the 2θ range of 19°–24°. With the addition of more PVP, the (100) and $(10\bar{1})$, peaks of PVA become sharper indicating an improvement in crystallinity of the nanofibers. Electrical conductivity of the polymer solution increases from 189 μS for pure PVA solution to 606 μS for the PVA_{75}:PVA_{75} solution (Table 5.1). Increase in conductivity of the polymer solution results in more oriented molecular order inside the nanofibers. Therefore, with PVP inclusion, nanofibers become more aligned, leading to the observed texture or preferred orientation along the $(10\bar{1})$, direction. When solution viscosity is lower (*cf.* Table 5.1), the same applied voltage stretches out fibers more, leading to improved crystallinity and texture of the fibres.

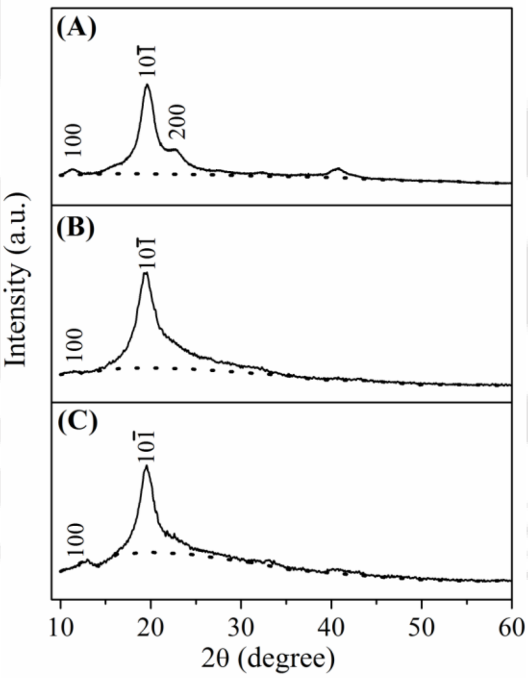

Fig. 5.3: XRD patterns of (A) PVA_{100}:PVP_{0}, (B) PVA_{90}:PVP_{10} and (C) PVA_{75}:PVP_{25} membranes. Dotted line shows the amorphous background due to PVP.

Chemical structure of the membranes was characterized with a FT-IR spectrophotometer (*cf.* 2.2.1.4). Fig. 5.4 shows the evolution of the characteristic absorption bands of PVA and PVP in the hybrid nanofibrous membranes. Since these two polymers possess some common functional groups, the group regions of IR spectra partially overlap which result in overlapping of bands in the blends.

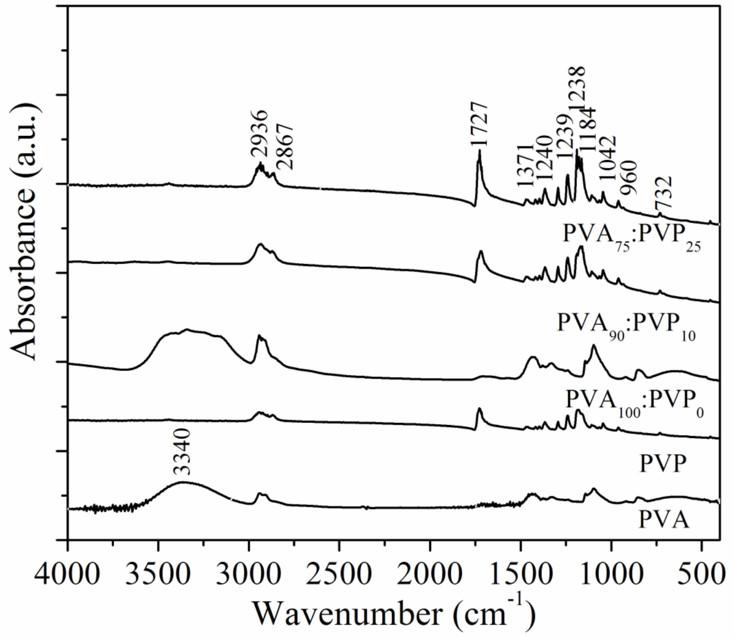

Fig. 5.4: FT-IR spectra of PVA, PVP, PVA_{100}:PVP_0, PVA_{90}:PVP_{10} and PVA_{75}:PVP_{25} membranes.

FT-IR spectra of PVA powder and PVA_{100}:PVA_0 membranes clearly reveal the major peaks associated with PVA. For instance, the broad C–H alkyl stretching band (ν = 2867-2914 cm^{-1}) and the strong hydroxyl bands typical of free alcohol (–OH stretching band at ν = 3340 cm^{-1}) along with hydrogen bonded band (ν = 3200-3570 cm^{-1}) are observed in these spectra. The higher intensity of peaks in electrospun PVA indicates improved crystallinity in the nanofibrous membranes [NRAJE13a, UMAS14a]. Absorption peaks at 1042 cm^{-1} (C–O, 1090–1150 cm^{-1}), 960, 1371 cm^{-1} (CH_2 bending) and 732 cm^{-1} (CH_2 rocking) which are characteristic of PVA, appear in all the spectra. The vibrational band characterizing each polymer in the fingerprint region becomes prominent as the respective content increases in the blend. The characteristic hump at 3340 cm^{-1} (O-H stretching) of PVA diminishes in intensity with

PVP incorporation. This indicates that PVP gets cross-linked with the hydroxyl group of PVA. The absorption pattern of PVA_{100}:PVP_0 membranes show weak absorption at 1727 cm^{-1} corresponding to partially hydrolyzed acetate C=O group which grows in intensity when PVP content is increased. Moreover, the absorption at 1238-1240 cm^{-1} which is attributed to C-N vibration increases with PVP content [NRAJE13a, UMAS14a].

5.1.3 Mechanical properties

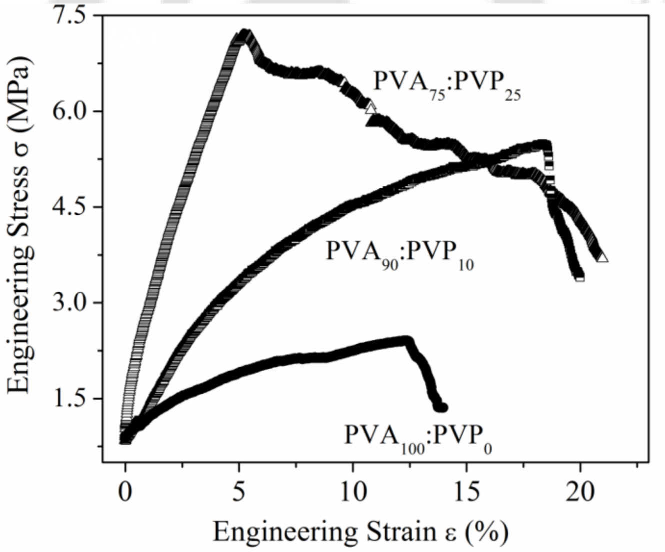

Fig. 5.5: Tensile stress-strain curve for PVA_{100}:PVP_0, PVA_{90}:PVP_{10} and PVA_{75}:PVP_{25} membranes.

Mechanical testing of the membranes was performed using the Deben microtest unit as described in section 2.2.4. Ultimate tensile strength and Young modulus of the membranes were estimated from the stress versus strain plots. During tensile testing of the membranes, the load was gradually applied until the samples started to tear. Fig. 5.5 shows the variation of tensile stress (σ) as a function of % strain (ε) for PVA and PVA-PVP nanofiber membranes. All of the membranes were tested in laboratory environment under identical conditions.

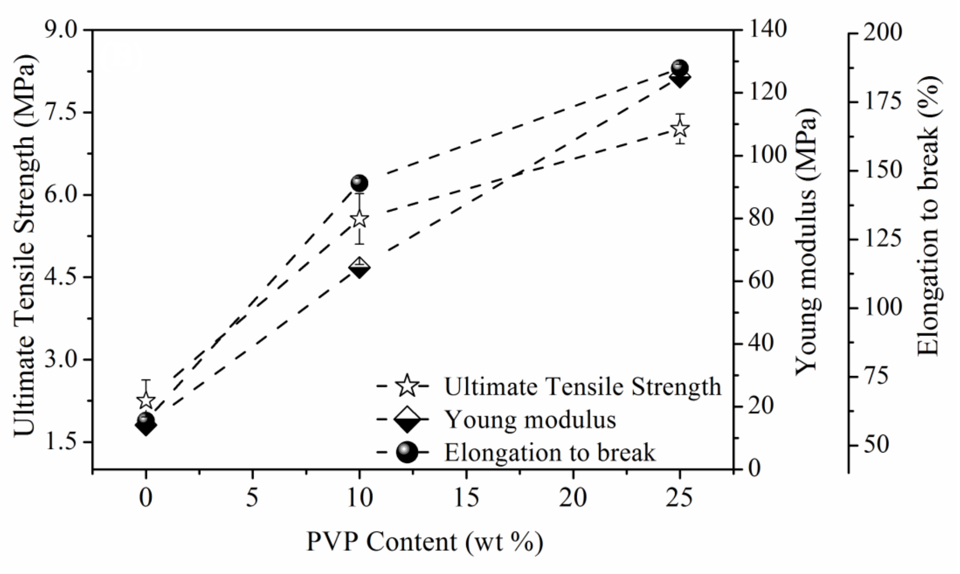

Fig. 5.6: Ultimate tensile strength, Young's modulus and elongation at break as functions of strain (%) for PVA_{100}:PVP_0, PVA_{90}:PVP_{10} and PVA_{75}:PVP_{25} membranes.

Ultimate tensile strength of the membranes increased with PVP substitution from 2.25 MPa for the pure PVA membrane to 5.55 and 7.20 MPa for the membranes with 10% and 25% PVP, respectively. The corresponding values of Young's modulus are 14.2, 64.3 and 125.0 MPa, respectively (*cf*. Fig. 5.6). Failure occurs at higher loads for the membranes with higher PVP content. The initial increase in the tensile strength and Young's modulus (*i.e.* for the composites containing 10% of PVP) can be attributed to the improved crosslinking in PVA-PVP composite. Chemical bonding between these two polymers gives rise to higher mechanical strength. Recent studies indicate that chemical bonding could result in interfacial shear stress as high as ~0.05 GPa [PERE10a]. Tensile strength of these membranes is in good agreement with the result obtained for other electrospun products [PERE10a, ESSA14a, JEON07a, ZAMA11a]. Compared to other dressing materials, tensile strength of the electrospun nanofibers was found to be lower but these membranes exhibit a larger elongation. In the case of chitosan film and gelation based bandage, tensile strength was found to be

~67 MPa and 12.7 MPa, and elongation at break was 21%-67% and 40%, respectively [ZAMA11a,PEHK00a]. These observed differences in strength can be attributed to the process adopted to cast the fiber. In the present studies, a steady rise of elongation at break was observed with increasing percentage of PVP, as expected. Compared to pure PVA (~59%), the elongation of the membrane containing 10% and 25% PVP increased to ~145% and ~187%, respectively. It is obvious that PVP incorporation induces interconnected fibrous network, as observed from the FESEM images, which increases elongation of the membrane before rupture.

5.1.4 In vitro fluid uptake and degradation behaviour

Fluid uptake ability and degradation behavior of the membranes were investigated by soaking the membranes for various time periods in SBF as per the recipe given in section 2.2.5. In order to provide an appropriate physiological environment, *pH* of SBF was adjusted to 7.40 and the test environment was maintained at 37°C. Degree of swelling or capability of fluid retention of the membranes was determined using the Eq. 2.9 (*cf.* section 2.2.5.2).

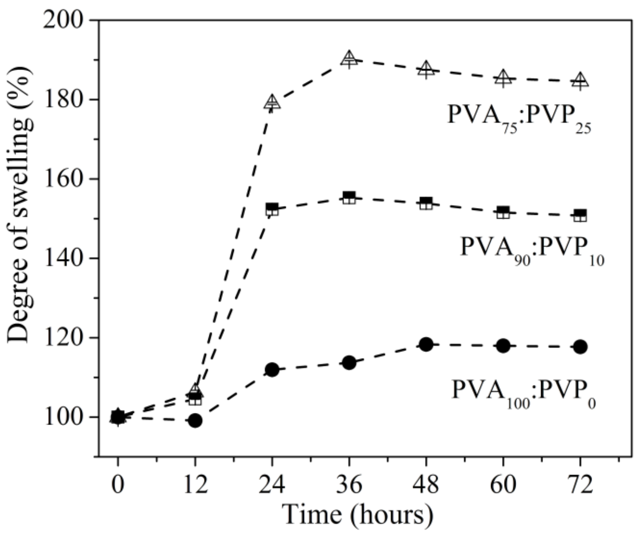

Fig. 5.7: Swelling profile of PVA_{100}:PVP_0, PVA_{90}:PVP_{10} and PVA_{75}:PVP_{25} membranes for 3 days of immersion in SBF.

TH-1620_10612107

As already mentioned, moist environment reduces the level of exudate, improves wound bed moisture retention, improves wound collagen matrix, removes cellular products and protects the epithelializing bed [KEAS98a, SUJA12a]. Moisture retentivity study was performed on all specimens and the results are displayed in Fig. 5.7. Upto 12 h of soaking, PVA_{100}:PVP_{0}, PVA_{90}:PVP_{10} and PVA_{75}:PVP_{25} membranes did not exhibit significant swelling. This may be due to less amount of fluid diffusion through membranes at the initial stage of immersion. A gradual increase in swelling was observed in all membranes after 12 h of immersion. Significant increase in fluid uptake was observed between 12 h to 36 h of immersion and thereafter the fluid uptake remained nearly constant. Comparing the percentage of swelling of PVA_{100}:PVP_{0}, PVA_{90}:PVP_{10} and PVA_{75}:PVP_{25} membranes after immersion in SBF for 36 h shows that PVA_{100}:PVP_{0} membranes swelled by 10 % whereas PVA_{90}:PVP_{10} and PVA_{75}:PVP_{25} exhibited higher swelling of 16 % and 20 %, respectively. Due to the nanoporous structure of the membranes, fluid hydrates the membranes to a larger extent, leading to volumetric expansion of the membranes. Swelling ratio of PVA_{75}:PVP_{25} membrane was always higher than that of PVA_{100}:PVP_{0} membrane because of the presence of the strong hydrophilic PVP in the latter. The high hydrophilic nature and hence the high affinity for water, makes PVP rich membranes to swell to a larger extent. At this stage, these membranes are expected to maintain a moist environment and to decrease dehydration and cell death. They can also maintain blood and nutrients supply and increase the rate of re-epithelialization. Water retentivity in PVA_{75}:PVP_{25} membrane was found to be much higher (190 %) than the value (90 %) reported by Maheshwari *et al.* [UMAS14a]. Incorporation of PVP in PVA induces these membranes to maintain a better moist environment in the time period of study.

In vitro degradation studies were conducted on the three membranes as per procedure explained in section 2.2.5.2. Fig. 5.8 shows the degradation profile of the three membranes immersed in SBF.

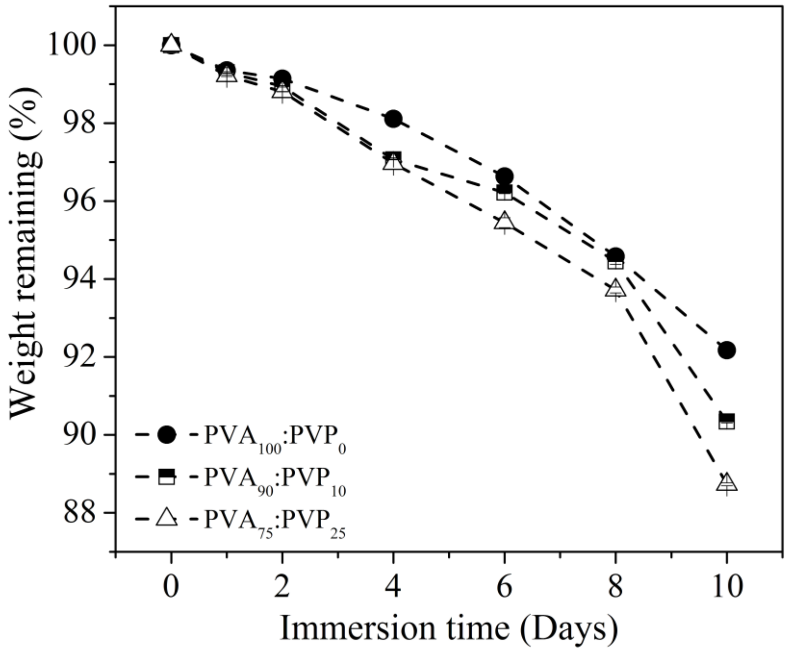

Fig. 5.8: Degradation profile of PVA$_{100}$:PVP$_0$, PVA$_{90}$:PVP$_{10}$ and PVA$_{75}$:PVP$_{25}$ membranes for 10 days of immersion in SBF.

The degradation property allows *in situ* degradation of necrotic material which is then absorbed into the fluid phase of the dressing [KEAS98a, SUJA12a]. Comparison of this data with the swelling behavior exhibited in Fig. 5.7 shows that the membranes do not show much degradation up to 36 h of immersion since they were absorbing the fluid during this period. However, after 4 days of immersion time, significant degradation is observed. PVA$_{100}$:PVP$_0$ membrane shows a weight loss of 8% after 10 days of immersion, while the composite membranes exhibit 10% and 12% weight losses for the same period of immersion. Interaction of water with the functional group of PVP leads to disintegration of molecular chains of the polymer. Hence, higher degradation was observed in PVA$_{75}$:PVP$_{25}$ membrane as expected, because of its higher hydrophilic PVP content. It is interesting to note that PVA_{75}:PVP_{25} exhibited the highest swelling as well as degradation behavior among the three membranes.

5.1.5 Bioactivity analysis

5.1.5.1 Cell culture and alamarBlue cell proliferation assay

In vitro cell proliferation study was performed as per procedure explained in section 2.2.6.1. L929 murine fibroblast cells and HaCaT human keratinocyte cells were chosen for this study and cultured in DMEM/F12 (Gibco, USA) supplemented with 10% FBS and antibiotics. Non-seeded wells containing only the membranes were supplemented with 10% alamarBlue dye and used as a negative control. AlamarBlue assay was carried out to quantify proliferation of cells as a function of time. Reduction in alamarBlue corresponds to cell metabolism which co-relates to the number of proliferating cells. After 7 days of culture, L929 fibroblast cell number showed the following trend: ~70 % on pure PVA, ~50 % on PVA_{90}:PVP_{10} and ~33 % on PVA_{75}:PVP_{25} as compared to 1 day (*cf*. Fig. 5.9(A)) In the case of HaCaT cell, similar trend was observed with 3.9 fold proliferation on PVA, ~3.8 fold on PVA_{90}:PVP_{10} and ~3.4 fold on PVA_{75}:PVP_{25} membrane as compared to day 1 (*cf*. Fig. 5.9(B)). Following 7 days of culture, both PVA_{100}:PVP_{0} and PVA_{90}:PVP_{10} membranes exhibited significantly higher cell proliferation for both L929 fibroblasts ($p < 0.01$) and HaCaT cells ($p < 0.05$) compared to PVA_{75}:PVP_{25}. Cell proliferation rates on PVA_{75}:PVP_{25} membranes for both cell types were found to be less. Hydrophilicity of PVP [UMAS14a] is the reason for lesser proliferation on PVA_{75}:PVP_{25} membrane which is also evident from our results (*cf*. Fig. 5.9 (A, B)). Thus, PVA is responsible for the cell proliferation attribute of the membranes. *In vitro* culture results using native skin cell types *i.e.* fibroblast and keratinocytes confirm the biocompatibility of these membranes.

Further, these studies assert that these matrices can be applied as dressings on human skin without any adverse side effects or irritation [MAND12a, MAND09a, MAND09b].

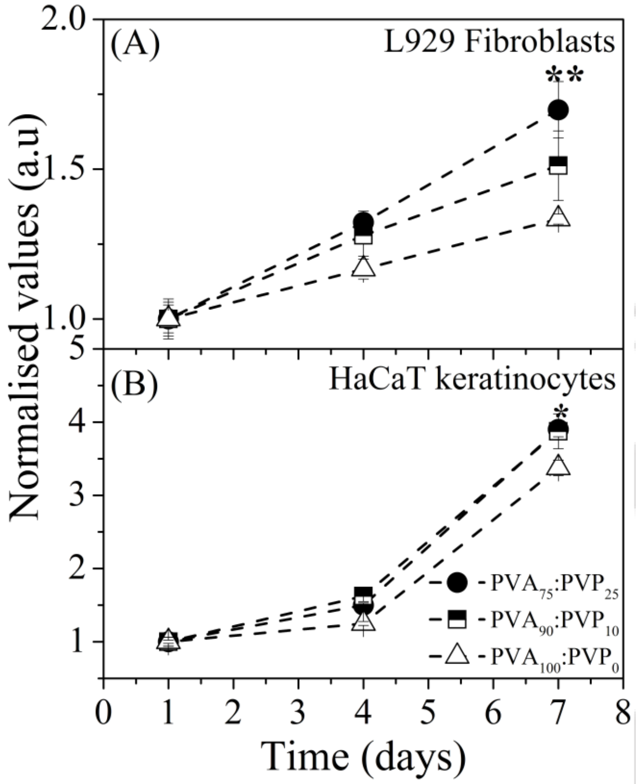

Fig. 5.9: AlamarBlue cell proliferation assay showing (A) L929 fibroblast cell, and (B) HaCaT keratinocyte cell proliferations on the three membranes. Data represents the average value along with standard deviation (*$p < 0.05$, **$p < 0.01$).

5.1.5.2 Live/Dead assay for cellular viability

To test the cytocompatibility, viability and adherence of cells of these membranes, live/dead assay (*cf.* section 2.2.6.2) was done. As evident from the fluorescence images, a high proportion of seeded cells of both L929 (Fig. 5.10 (A-C)) and HaCaT (Fig. 5.10 (D-F)) attached firmly to the membranes and proliferated well. Cells were mostly in their native spindle morphology suggesting the membranes to be cell supportive and hence highly biocompatible. Cells were observed to spread to their normal morphology throughout the membrane irrespective of their composition. So, one can safely assume that these membranes are suitable for biomedical (especially, skin/wound) applications.

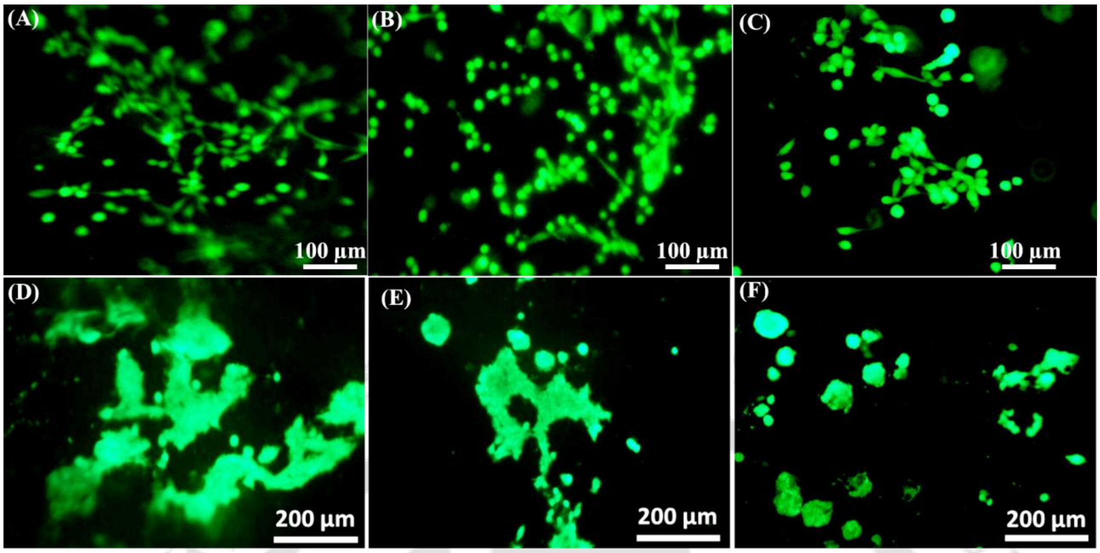

Fig. 5.10: Live cell image of L929 fibroblasts on (A) PVA_{100}:PVP_0, (B) PVA_{90}:PVP_{10} and (C) PVA_{75}:PVP_{25} membranes. Live cell image of HaCaT keratinocytes on (D) PVA_{100}:PVP_0 (control) (E) PVA_{90}:PVP_{10} and (F) PVA_{75}:PVP_{25} membranes.

5.1.5.3 In vitro antimicrobial tests

Antibiotic release from membranes was investigated using ciprofloxacin hydrochloride monohydrate (Himedia, India, MW 385.82 Da) and experiment was performed as per the procedure explained in section 2.2.6.3.

Ciprofloxacin hydrochloride monohydrate is a broad-spectrum antibiotic which is known to be effective against both the gram-positive and gram-negative bacteria and so it was used as a model antibiotic in this study [DRUS86a]. Ciprofloxacin antibiotic release from membranes was evaluated as a function of composition for the three membranes. Following 24 h of incubation, % release of antibiotic was found to be 12 ± 2 %, 16 ± 2 %, and 22 ± 3 % from PVA_{100}:PVP_0, PVA_{90}:PVP_{10} and PVA_{75}:PVP_{25} membranes, respectively (Fig. 5.11). These electrospun membranes exhibited varied release profiles depending upon their composition. On day 14 of incubation, the cumulative release was 56 ± 6 %, 62 ± 5 %, and 76 ± 8 % from PVA_{100}:PVP_0,

PVA_{90}:PVP_{10} and PVA_{75}:PVP_{25}, respectively. The observed slow and sustained release of antibiotic is expected to enhance the healing rate of wound by protecting it from external microbes without any probable side-effects. This is a major advantage of such smart dressing, as they can themselves deliver bioactive molecules and protect the wound from cross contamination, which ultimately lead to faster healing of the wound.

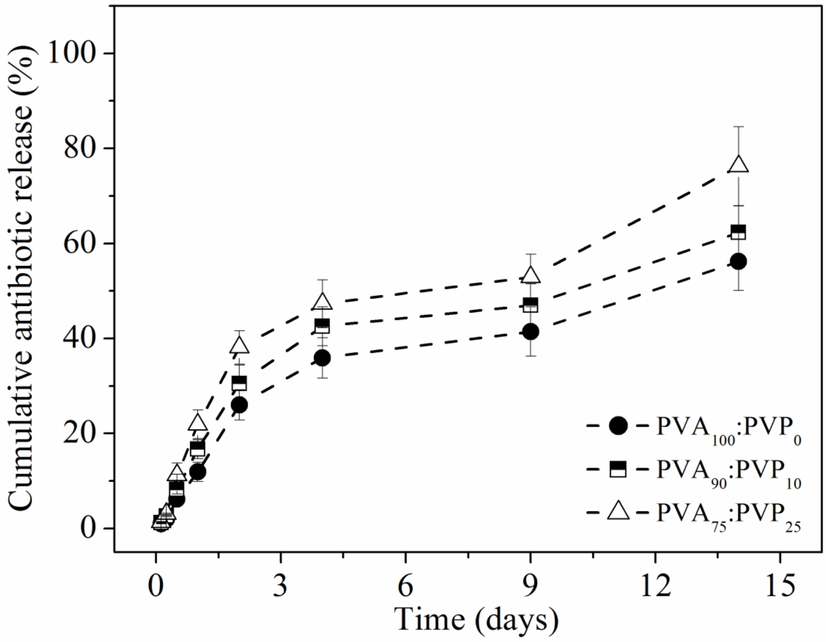

Fig. 5.11: Cumulative antibiotic release from PVA_{100}:PVP_0, PVA_{90}:PVP_{10} and PVA_{75}:PVP_{25} membranes.

Antibiotic release study from membranes and its effect on microbial growth inhibition was analyzed using ciprofloxacin hydrochloride monohydrate. This study was performed with gram positive *Staphylococcus aureus* (S. aureus) as per the procedure discussed in section 2.2.6.3. *S. aureus* is considered to be a classic opportunist since it takes advantage of broken skin or other entry sites to cause an infection and ciprofloxacin is very effective against this microbe [DRUS86a, HARRI02a]. The drug incorporated membranes were placed over agar plate and kept overnight in an incubator at 37 °C. The diameter of the zone of inhibition was calculated using ImageJ software. Antibiotic release from drug adsorbed membranes was evaluated by observing the inhibition to *S. aureus* growth in agar plates. *S. aureus* is one of the most common causes of skin and wound infections after injury or surgery [HARR02a]. The diffused antibiotic from membranes creates a clear zone of inhibition to microbial growth in the agar solution. Formation of zone of inhibition around the membranes confirms the antibiotic release from the membranes. The diameter of inhibition zone was 25.2 ± 0.6 mm, 26.6 ± 0.8 mm, and 31.1 ± 0.9 mm for PVA_{100}:PVP_0, PVA_{90}:PVP_{10} and PVA_{75}:PVP_{25}, respectively. Observed zone of inhibition serves as additional confirmation for *in vitro* antibiotic release by the membranes (*cf*. Fig. 5.11). The results obtained show that the fabricated membranes are capable of sustained release of encapsulated drug over time and the protective action of ciprofloxacin against external pathogenic microbes.

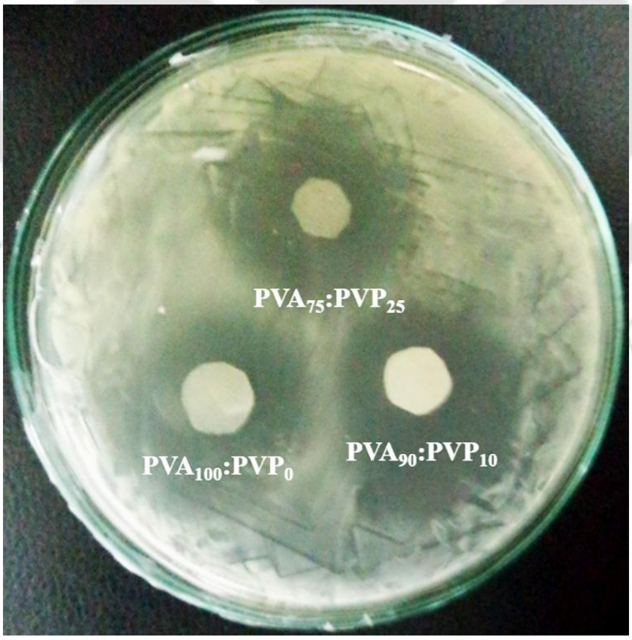

Fig. 5.12: Zone of microbial growth inhibition around PVA_{100}:PVP_0, PVA_{90}:PVP_{10} and PVA_{75}:PVP_{25} membranes.

Indian Institute of Technology Guwahati

5.2 PVA-bioglass 45S5 based composite nanofibrous membranes

For effective bone tissue engineering, the synthetic scaffold architecture should mimic the porous microstructure of cancellous bone [BETT15a, MURU15a] apart from possessing suitable surface chemistry to promote cell attachment, proliferation and differentiation [HENC06a, MNRA11a, NIEH09a] and mechanical properties compatible with the host tissue. Bioactive glasses (BGs) and biodegradable synthetic polymers are among the most widely studied materials for orthopedic applications [HENC06a, RAHA11a, COST12a]. BGs are known for their excellent biocompatibility, biodegradability, osteoconductivity, and ability to form a bonelike mineral phase at the interface when in contact with living tissues [HENC06a]. Addition of magnetic components has been found to lead to superior biomaterial properties with wider applications including actuated local drug delivery, *in vivo* imaging and magnetic hyperthermia [RKSI14a, BHAT14a]. By combining sol-gel process with electrospinning techniques, it is possible to develop nanofibrous composites exhibiting bioactive as well as magnetic properties. Keeping this in mind, attempts were made in this chapter to prepare composites nanofibrous membranes.

5.2.1 Preparation

An aqueous solution of 8 wt % PVA (MW ~80000 g/mol, 99 %) was prepared by fully dissolving PVA powder in ultra-pure deionized water at 80 °C under continuous stirring for 4 h followed by natural cooling to room temperature. Bioglass (BG) with composition $45SiO_2.24.5Na_2O.24.5CaO.6P_2O_5$ (in wt %) and magnetic bioglass (MBG) consisting of BG composition with 2 wt % Fe_2O_3 were separately synthesized as per the procedure already discussed in chapter 4. Gel form of these glasses was then blended with PVA solution by gentle stirring for 24 hours at room temperature to form

TH-1620_10612107

PVA-BG and PVA-MBG solutions. Electrical conductivity and viscosity of the gelatinous solutions were measured and found to be in electrospinning range (*cf*. Table 5.2.). PVA-BG and PVA-MBG solutions were then electrospun with anode tip to collector distance of 12 cm, potential difference of 15 kV and solution flow rate of 2.0 ml/h to obtain continuous nanojets which condensed into nanofibers. The composite nanofibers were collected on aluminum foils. Free standing 40 μm thick nanofibrous membranes were obtained after electrospinning for 3 h under the above conditions (*cf.* 2.2.3).

Table 5.2: Viscosity and electrical conductivity of aqueous PVA-bioglass solutions.

Solution Composition	Viscosity (cP)	Electrical conductivity (μS)
PVA	15	290
PVA-BG	467	321
PVA-MBG	461	354

5.2.2 Structure and morphology

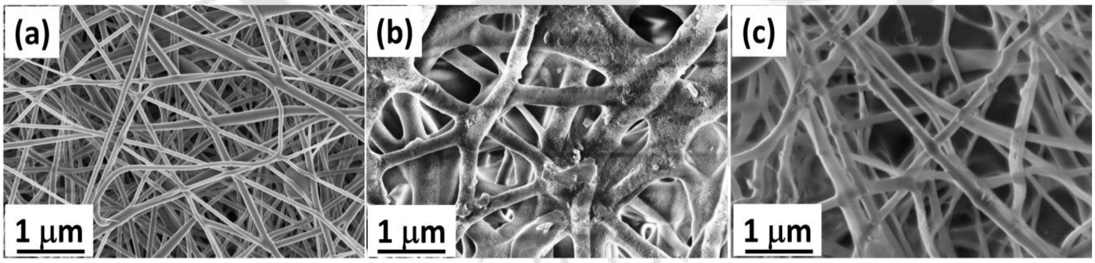

Fig. 5.13: FESEM images of (a) PVA, (b) PVA-BG and (c) PVA-MBG membranes showing interlinked fibrous morphology.

FESEM micrographs of the composite nanofibrous membranes shown in Fig. 5.13 indicate interconnected fibrous network devoid of bead or string formation. This interconnected fiber structure plays an important role in improving the mechanical strength of the scaffolds. The micrographs also reveal a homogeneous distribution of bioglass and magnetic bioglass within the PVA fibers. Pure PVA fibers have a smooth surface. However, the membranes containing MBG appears to be highly porous and textured. This shows that magnetic content in the filler promotes the formation of a highly textured scaffold. BG/MBG aggregates can be observed to be homogenously distributed inside the nanofibers.

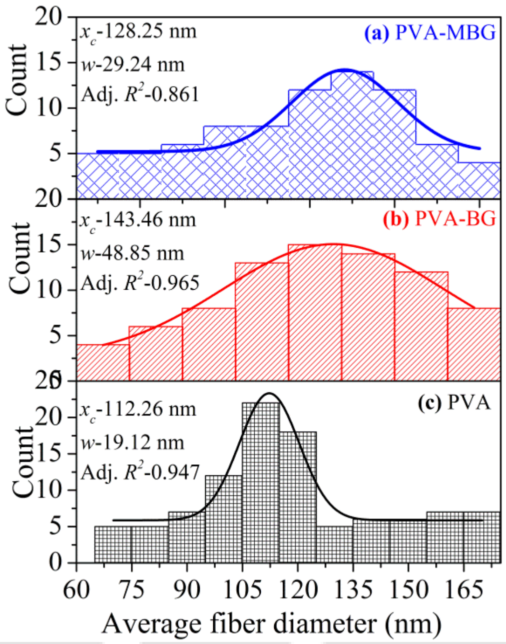

Fig. 5.14: Fiber diameter distributions in (a) PVA, (b) PVA-BG, and (c) PVA-MBG membranes (x_c is the peak or mean value, w is the width and R^2 indicates the goodness of the Gaussian fit).

The average diameter of the fibers of PVA membrane estimated from Gaussian fit to fiber distribution data shown in Fig. 5.14 was found to be 112 nm. Corresponding average fiber diameters of PVA-BG and PVA-MBG membranes were 143 nm and 128 nm, respectively. It is evident that additives broaden the fiber (diameter) size distribution considerably. Fiber diameter is significantly reduced in membrane containing MBG as compared to the one containing BG. Data given in Table 5.2 shows that the viscosity of PVA-BG and PVA-MBG solutions is nearly the same but the electrical conductivity of the latter is considerably higher. This indicates that magnetic content in the filler influences the electrical conductivity of the solution. Increase in solution conductivity tends to increase the deposition area of fibers due to increase in polymer jet's trajectory. This stretches the fibers and yields narrower fibers.

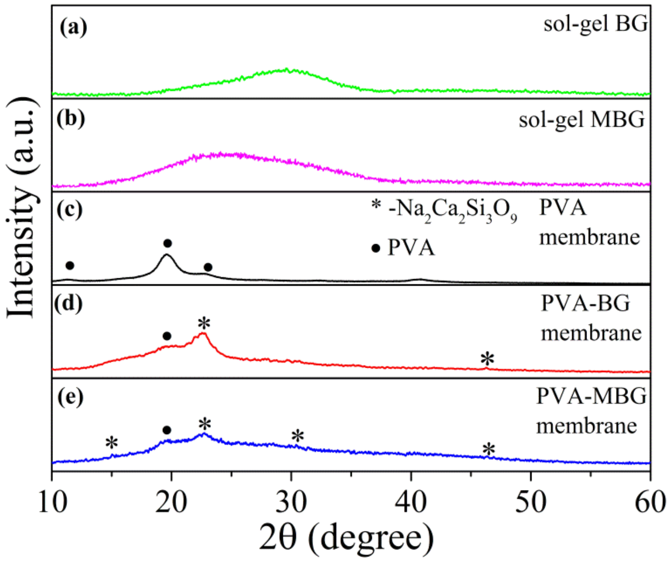

Fig. 5.15: XRD patterns of (a) sol-gel derived BG (b) sol-gel derived MBG and (c) PVA membrane, (d) PVA-BG membrane and (e) PVA-MBG membrane. Symbols • and ∗ denote XRD peaks of PVA and $Na_2Ca_2Si_3O_9$, respectively.

XRD patterns of sol-gel derived BG, sol-gel derived MBG, electrospun PVA, electrospun PVA-BG and electrospun PVA-MBG membranes are shown in Fig. 5.15 (a-e). It is evident from Fig. 5.15 (a, b) show the amorphous nature of the sol-gel derived BG and MBG. Semi-crystalline PVA usually displays XRD peaks centered at 2θ =11° (100), 19.8° ($10\bar{1}$), 22.9° (200) and 40.6° (unassigned) [NRAJE13a, UMAS14a]. Broadened XRD peaks exhibited by pure PVA membrane shown in Fig. 5.15(c) denote the 1-dimensionl nanostructure of the espun membrane and the poor crystallinity of the rapidly solidified liquid polymer jets in the electrospinning process. However, the composite PVA-BG and PVA-MBG membranes exhibit a broad hump with a few weak crystalline peaks superimposed on this. This shows that the membrane is predominantly amorphous with some minor crystalline inclusions. These weak peaks appearing at 2θ = 11° (100), 19.8° ($10\bar{1}$), 22.9° (200) and 40.6° (unassigned) have been identified as reflections from PVA planes, and those at 2θ = 16.63° (012), 22.48° (013), 33.62° (024) and 46.39° (141) are from sodium calcium silicate ($Na_2Ca_2Si_3O_9$) planes. Since the gelatinous mixture of BG and MBG was blended with PVA and espun for a long period (~3 h) to obtain sufficiently thick composite nanofibrous membranes, there is a possibility for $Na_2Ca_2Si_3O_9$ phase to crystallize in nanocrystalline form. Control of percentage of the gelatinous mixture used in the electrospinning solution and reducing the electrospinning time may help in preventing the crystallization of $Na_2Ca_2Si_3O_9$ phase. However, presence of the bone mineral phase $Na_2Ca_2Si_3O_9$ in the membranes may improve their bioactivity and hence the presence of these precipitates may not be disadvantageous to scaffold application.

5.2.3 Magnetic properties

Isothermal magnetization curve of PVA-MBG composite nanofiber membrane recorded at room temperature for an applied magnetic field of ±15 kOe is depicted in Fig. 5.16. It is evident from the Fig. 5.16 that the samples show unsaturated ferromagnetic behaviour with a narrow magnetic hysteresis loop. Inset designated as (a) in Fig. 5.16 shows that the membrane exhibits moderate coercivity (H_c) of ~20 Oe and low remnant magnetization (M_r) of ~0.01 emu/g, which are typical characteristics of a weak soft ferromagnetic material [RDCU72a]. The magnetization at 15 kOe, ($M_{s(15kOe)}$) was 0.36 emu/g. One has to bear in mind that the magnetization was estimated for the total sample weight since it is not possible to isolate the magnetic content. The integrated loop area, which represents the magnetic loss / cycle, was estimated to be 105 erg/g from the hysteresis loop.

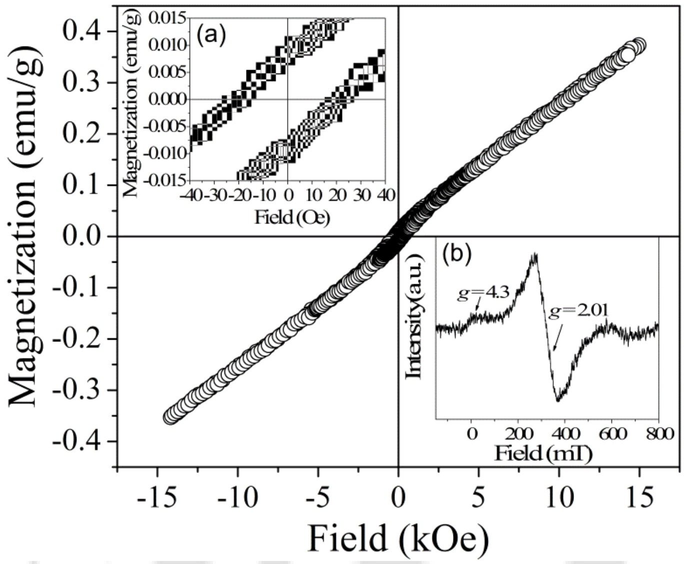

Fig. 5.16: Room temperature *M-H* loop of PVA-MBG. Inset (a) shows an expanded view of data close to the origin. Inset (b) shows room temperature EPR spectrum of PVA-MBG.

EPR absorption (derivative) spectrum of PVA-MBG is shown as inset (b) in Fig. 5.16. Presence of both the absorption lines in PVA-MBG membrane indicates that both Fe^{2+} and Fe^{3+} ions are present in both isolated as well as clustered manner in the membrane. Since the membrane filler is a sol-gel derived product, it is highly porous. Fe^{2+} and Fe^{3+} ions occupy two types of site with different coordinations in the sol-gel matrix. EPR parameters, J and ΔH of $g \approx 4.3$ and $g \approx 2.01$ absorption lines are $J_{g=4.3} = 12 \times 10^6$ and $\Delta H_{g=4.3} = 42 \times 10^{-3}$ T and $J_{g=2.01} = 57.1 \times 10^6$, $\Delta H_{g=2.01} = 97 \times 10^{-3}$ T. Comparison of the EPR parameters obtained for the composite with that of the filler (MBG) discussed in chapter 4 shows that $J_{g=2.01}$ and $\Delta H_{g=2.01}$ values of PVA-MBG are close to the values of $J_{g=2.01} = 49.1 \times 10^6$ and $\Delta H_{g=2.01} = 99 \times 10^{-3}$ T obtained for MBG. This implies that clustering mechanism dominates in electrospun membranes just as in the sol-gel magnetic bioglass. In the case of $g \approx 4.3$ absorption line, $J_{g=4.3}$ and $\Delta H_{g=4.3}$ values of PVA-MBG are lower than those in MBG ($J_{g=4.3} = 34 \times 10^6$ and $\Delta H_{g=4.3} = 55 \times 10^{-3}$ T), which shows that the site deviation of Fe^{3+} is lower in the membrane.

5.2.4 Mechanical properties

Stress-strain curves of nanofibrous scaffolds are presented in Fig. 5.17 and the parameters obtained are summarized in Table 5.3. All the samples showed a similar stress-strain behavior with two discernible stages: an initial stage with a rapid increase in stress up to ~0.1–0.15 % strain, followed by a stage featuring slower increase of stress up to the failure point. Blending with BG improved the tensile property of the PVA membranes. Though electrospun membranes do not have very high mechanical strength, combining PVA with BG remarkably improves the mechanical properties of PVA membrane. Inclusion of BG and MBG resulted in changes to fiber morphology and consequently the membrane structure as already discussed in section 5.2.2. PVA-MBG scaffold exhibited the highest tensile strength (26.0 MPa) followed by PVA-BG (20.9 MPa) and pure PVA (5.5 MPa) scaffolds. Pure PVA scaffolds lacked sufficient inter-fiber bonding and therefore exhibited relatively low mechanical strength. Compared to the yield strength reported for polyurethane/HA membrane [TETT14a] (0.6 MPa) and tensile strength of PCL/45S5 BG (1.33 MPa) [OTAD15a], the yield strength and tensile strength values of PVA-BG and PVA-MBG membranes are significantly higher. Addition of MBG can lead to the formation of inter-fiber bonds in PVA, which could be the reason for its improved mechanical strength [RKSI14a].The elastic modulus of the membranes representing the stiffness of samples was determined from the initial slope of the stress-strain curves (*cf*. Table 5.3). The elastomeric nature of PVA provides necessary elongation to the composite membranes which will improve their prospects as bone graft substitutes. The elongation at break behaved in a similar way as ultimate tensile strength and stiffness values of the membranes. The strain at failure, considered as the elongation rate, was slightly higher for PVA-MBG membrane.

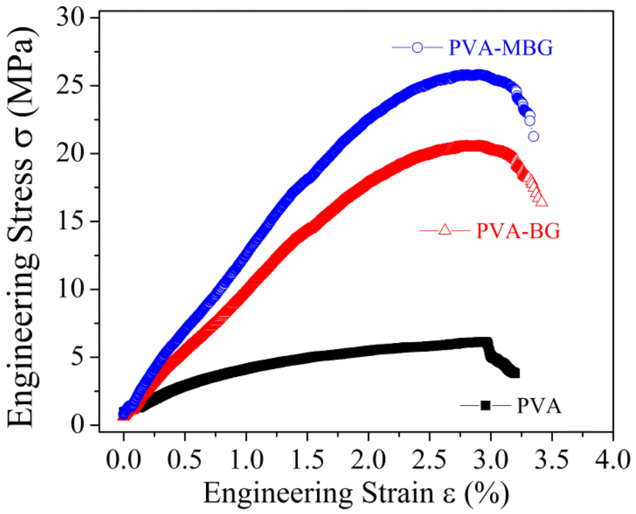

Fig. 5.17: Tensile stress-strain curves corresponding to PVA, PVA-BG and PVA-MBG membranes.

Table 5.3: Ultimate tensile strength, Young's modulus and elongation at break for PVA, PVA-BG and PVA-MBG membranes.

Specimen	Ultimate tensile strength (MPa)	Young's modulus (MPa)	elongation at break (%)
PVA	5.5	16.8	32.0
PVA-BG	20.9	244	34.1
PVA-MBG	26.0	257	33.5

5.2.5 In vitro fluid uptake and degradation behaviour

Swelling experiments were performed on triplicate specimens of the three membranes. A representative fluid uptake behavior is shown in Fig. 5.18. The results reveal that PVA-BG (118 %) and PVA-MBG (121 %) membranes have a slightly lower fluid uptake value as compared to bare PVA membrane (125 %). In early 12 h of soaking time, PVA and PVA-BG membranes did not exhibit significant swelling. This may be due to less amount of fluid diffusion through these membranes at this stage. Relatively rapid fluid uptake by PVA-MBG membrane during this initial period of immersion is due to its higher porosity. It has been shown that the swelling volume of membranes decreases from 450 % (for PVA scaffold) to 300 % (for PVA/chitosan scaffold)

[ALHO12a]. This comparison shows that addition of sol-gel based porous BG and MBG yields better swelling behaviour than chitosan. The reduced swelling volume could be attributed to a more rigid network formed by the inter- and intra-polymer reactions and also to the reduction of hydrophilic groups in PVA-BG blends. This observation is in agreement with previous studies which reported that impurity decreases the swelling rate when blended with PVA and the amount of reduction depends on factors such as weight ratio of the components, pH, temperature, *etc.*[ALHO12a].

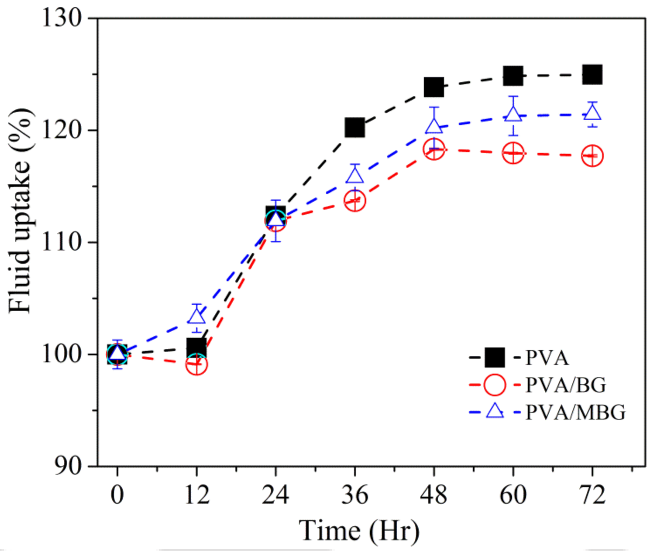

Fig. 5.18: Swelling profile of PVA, PVA-BG and PVA-MBG membranes for 3 days of immersion in SBF.

The degradation of the composites was tested by immersing the membranes for 15 days in SBF (*cf.* Fig. 5.19). It can be observed from Fig. 5.19 that all threes membranes do not exhibit significant degradation during the first 2 days of immersion. After 2 days, bare PVA membrane degraded faster because of hydrophilic nature of PVA. A weight loss of up to 40 % was observed in PVA membranes after 15 days immersion. Slow and controlled degradation with comparatively lower weight loss is observed in the case of the composites membranes. This is in expected lines because the composite membranes containing bioglass form well bonded HA layer on their surface by ion exchange with the medium, which actually increases the weight of membranes. HA formation on the surface of the membranes has been confirmed by monitoring the pH of SBF solution. It may be noted that the weight loss in PVA-MBG membrane (32 %) for 15 days immersion is higher than that of PVA-BG (28 %). This difference shows that there are other factors such as hydrophilicity, fiber diameter, and porosity which also influence the degradation behaviour of the membranes. PVA-MBG membranes have thinner fibers and higher porosity which promote faster dissolution in SBF as compared to PVA-BG membrane.

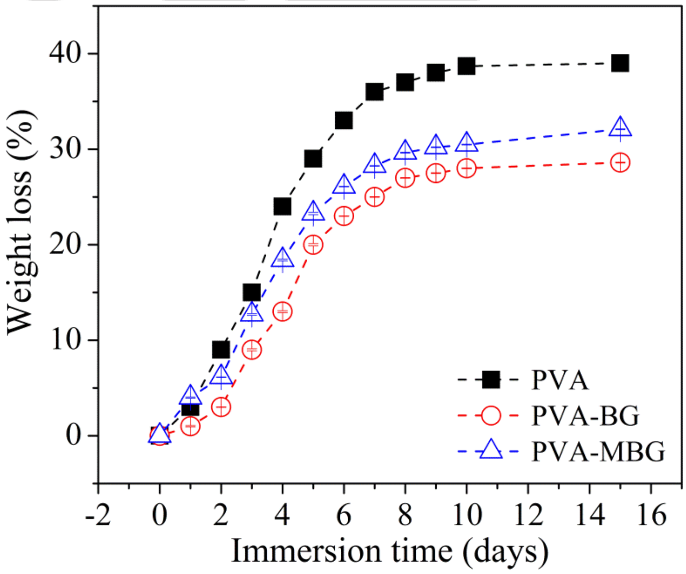

Fig. 5.19: Degradation profile of PVA, PVA-BG and PVA-MBG membranes for 15 days of immersion in SBF.

It has already been discussed in section 1.2.3 that HA formation and growth on the surface of bioactive specimen is governed by a series of pH sensitive chemical reactions [KOKU06a]. pH variation of SBF during specimen immersion test was monitored and the data is presented in Fig. 5.20. pH of SBF containing bare PVA membrane does not show any noticeable variation over the entire immersion period, which shows that there are no exchange of ions between this membrane and SBF and hence it does not show signs of HA layer formation. On the other hand, pH of PVA-BG and PVA-MBG show evidence of strong ion exchanges with pH reaching saturated values of 8.78 after 15 days of immersion. High pH values have been found necessary for new bone formation and the present data highlights the potential of these membranes for bone formation. Fig. 5.20 also displays the pH variations observed in the sol-gel derived BG and MBG that were used to form the composite membranes. It is obvious that both the sol-gel fillers (BG and MBG) show the same response as the composite membranes. A comparison of the pH response of the bare PVA membrane shows that the HA formation ability of the composite membranes are due to the BG and MBG fillers present in them.

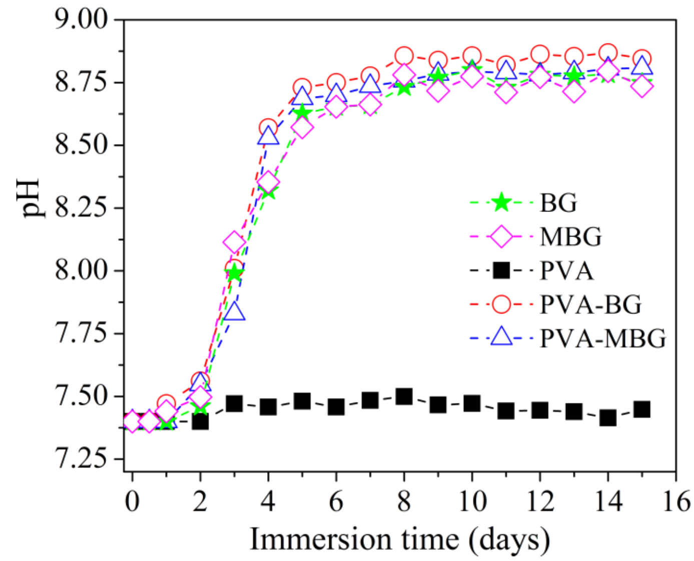

Fig. 5.20: Variation of pH as a function of immersion time of PVA, PVA-BG and PVA-MBG membranes in SBF. Data on sol-gel derived bioglass and magnetic bioglass samples are also shown for comparison.

5.2.6 Cell proliferation and cytocompatibility assessments

Cell proliferation studies were performed on all the three membranes using bone specific MG-63 osteosarcoma cells. Bone derived MG-63 (human osteosarcoma) cells were procured from NCCS, India. Cell proliferation and cytocompatibility assessments were performed as per the procedure given in section 2.2.6.

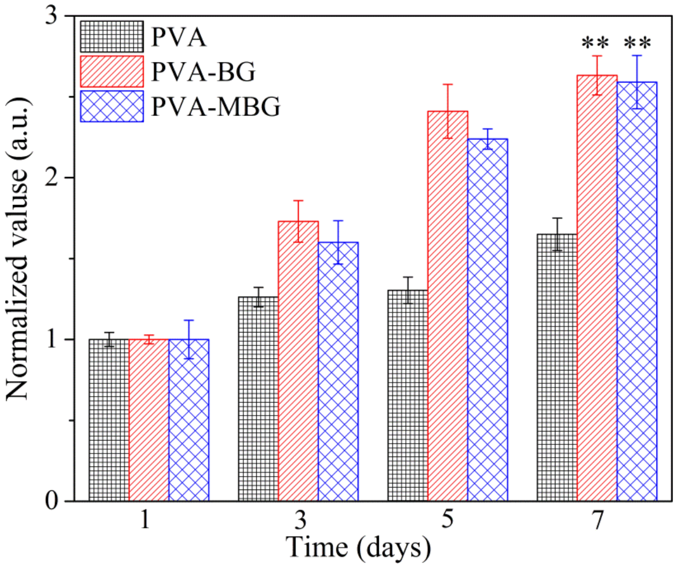

Fig. 5.21: AlamarBlue cell proliferation graph showing MG 63 osteosarcoma cell proliferation on different membranes. Data is presented as the mean value along with standard deviation. (** $p \leq 0.01$).

Fig. 5.21 shows that after 7 days of culture, cell proliferation rate showed the following trend: ~1.65 fold increase on bare PVA membrane, ~2.63 fold increase on PVA-BG membrane and ~2.60 fold increase on PVA-MBG membrane as compared to day 1 ($p \leq 0.01$). The difference in cell proliferation rates can be attributed to the difference in initial cell adhesion on the membranes. Fig. 5.21 shows that till day 7, the relative proliferation of the cell was significantly higher on PVA-BG and PVA-MBG membranes as compared to that on the bare PVA membrane (control) ($p \leq 0.01$). This quantitative result indicates that the membranes incorporated with BG and MBG components are biocompatible and the composite PVA-BG and PVA-MBG membranes are potential bio-scaffold materials for bone regeneration.

Viability and adherence of the cells seeded on all the membrane variants were investigated with fluorescent imaging after 7 days of culture (*cf.* section 2.2.6.2). As evident from fluorescent microscope images shown in Fig. 5.22, a lesser proportion of MG-63 cells adhered to bare PVA (control) membranes. Even after adhesion, they could not proliferate on PVA as well as they could do on PVA-BG and PVA-MBG membranes. Cells attached very firmly and spread (proliferated) very prominently on PVA-BG and PVA-MBG membranes as compared to PVA (control) membrane. Cells maintained their native spindle morphology and distributed evenly throughout the membranes indicating the composite membranes to be cytocompatible. Cells were organized in a cluster which results in better cell signaling and enhanced extracellular matrix (ECM) deposition. Live/Dead images show the same proliferation trend as depicted by AlamarBlue assay study described in the previous section (*cf*. Fig. 5.21). These combined results establish the suitability of these PVA-BG and PVA-MBG composite membranes for bone tissue engineering applications. Results obtained in these studies are also supported by previous reports where PVA in combination with other polymers has shown enhanced cytocompatibility and cell proliferation [BHAT14a, COST12a].

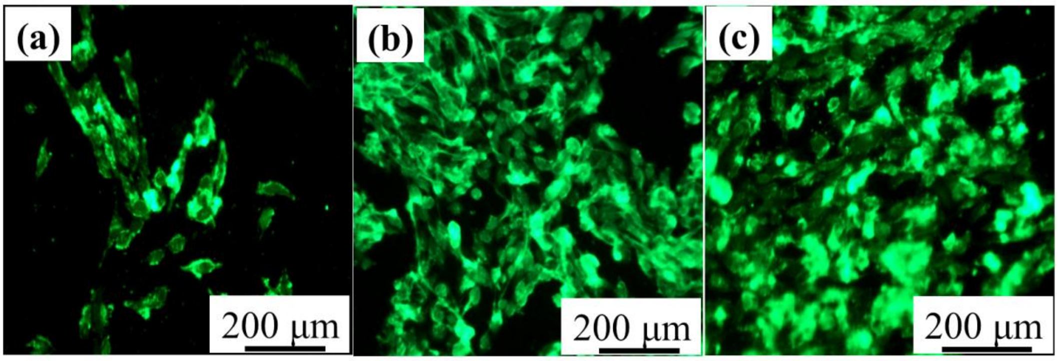

Fig. 5.22: Fluorescent microscope images of MG-63 cell attachment, proliferation and viability on (a) PVA (control), (b) PVA-BG and (c) PVA-MBG membranes.

Alkaline phosphatase (ALP) enzyme activity of cultured cells was assessed by following the protocol detailed in section 2.2.6.4. ALP enzyme is a hallmark quantitative marker for osteogenic differentiation [HENC06a]. ALP enzyme activities on the three different matrices are as follows: ~17 U/L on PVA < ~18.9 U/L on PVA-MBG < ~19.6 U/L on PVA-BG (Fig. 5.23).

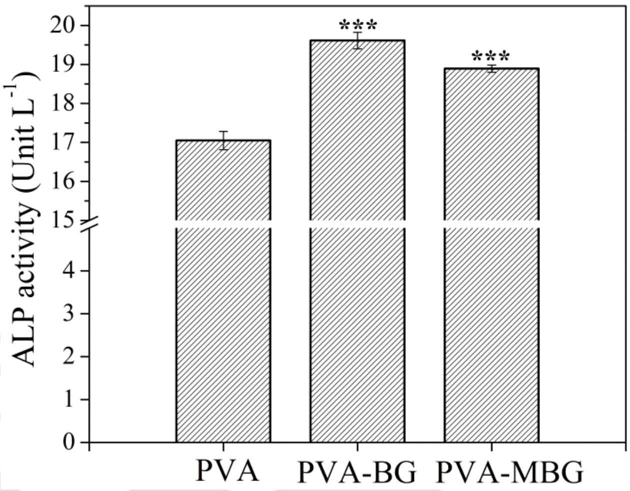

Fig. 5.23: ALP activity of MG-63 cells after 7-day culture on PVA, PVA-BG and PVA-MBG membranes. Data presented are mean with standard deviation (*** $p \leq 0.001$).

These results indicate that PVA-BG and PVA-MBG composite membranes support the differentiation of MG-63 osteoblast cells with significantly enhanced ALP activity as compared to the control PVA membrane ($p \leq 0.001$). Small amounts of bone mineral ($Na_2Ca_2Si_3O_9$) precipitate in PVA-BG and PVA-MBG appear to help in new bone formation. Thus, the composite membranes maintain the differentiated phase of MG-63 like bone cells with ALP activity. BG also has the ability to promote neovascularization which contributes to faster wound healing and successful bone tissue regeneration [MNRA11a]. Fibrous composites provide nucleation site for bone-like mineral deposition by the cells which leads to enhanced ECM production and tensile strength [BHUM11a, NORM94a].

5.3 Summary

- Smooth and homogeneous nanofibrous composite membranes were electrospun from optimized (8% w/v PVA with 20% w/v PVP) polymer solutions.
- PVP substitution in PVA improved the ultimate yield strength and Young's modulus of the membranes. High fluid uptake and slow degradation of these membranes confirmed that these membranes maintain a moist environment which is very important for fast wound healing.
- PVA_{90}:PVP_{10} membranes exhibit optimal antimicrobial barrier, sustained antibiotic release and cell proliferation abilities. These results unambiguously confirm that electrospun PVA-PVP nanofibrous membranes can be efficient and cost-effective interactive wound dressings.
- PVA-BG and PVA-MBG hybrid nanofibrous scaffolds were successfully synthesized by a combination of sol-gel and electrospinning methods.
- Structural and morphological studies revealed homogeneous distribution of BG and MBG in the composite membranes.
- PVA-MBG membranes exhibited spontaneous magnetization. Magnetic content influenced the fiber morphology and diameter and resulted in highly porous microstructure.
- Composite membranes exhibited very high tensile strength as compared to the pure PVA membrane.
- Optimal fluid uptake, bioactivie hydroxyapatite layer formation, slow degradation, cytocompatibility and cellular function combined with good tensile strength project electrospun PVA-BG and PVA-MBG matrices as potential 3-dimensional scaffolds for bone tissue engineering, actuated local drug delivery and magnetic hyperthermia for cancer treatment.

TH-1620_10612107

Chapter 6

Conclusions and scope for future work

6.1. Conclusions

The main goal of this study was to develop bioactive and biodegradable hybrid biomaterials with tailored physical, mechanical and biological properties for biomedical applications such as hyperthermia treatment of cancer, wound dressings and bone tissue engineering, In this course of this tryst, some challenging problems in biomaterial processing and analysis were also tackled. The work done in the last three chapters of this thesis attempts to highlight some common and uncommon features observed in the studies on magnetic bioglass-ceramics, nanoporous bioglass, nanoporous bioglass-ceramic and nanofibrous polymeric composites. The following are the conclusions drawn from these investigations:

- The third chapter focused on the task of characterizing two sets of magnetic bioglass-ceramics with the intention to optimize their properties for use as thermos-seeds in hyperthermia treatment, contrast agent in magnetic resonance imaging and targeted drug delivery. Two strategies to obtain efficient ferrimagnetic bioglass-ceramics were adopted. The first involved attempting to optimize the devitrification characteristics of $41CaO44SiO_24P_2O_58Fe_2O_33Na_2O$ (in mole %) glass by adopting different heat treatment temperatures and time periods. Combined analysis of XRD and magnetization data of the heat treated samples showed that the percentage of magnetite phase had a decisive role on the saturation magnetization of these magnetic bio-glass ceramics. Best heat treatment condition for this system turned out to be 2 h at 1050 °C, which resulted in M_s of 5.15 emu/g due to the contribution~6% magnetite phase present in the sample. The other strategy was to us find a stronger magnetic material. $15(ZnO,Fe_2O_3).50SiO_2.\ 20(CaO,P_2O_5).15Na_2O$ (in mole %) glasses containing Fe/Zn molar ratio of 6.5 was taken so as to promote crystallization of the high-M_s $Zn_{0.4}Fe_{2.6}O_4$ phase. Though it was structurally difficult to differentiate between $ZnFe_2O_4$ and $Zn_{0.4}Fe_{2.6}O_4$ phases, the glass-ceramics certainlly exhibted higher Ms than the other system with same amount of iron oxide. The heat treatment conditions was optimized for this system (2 h at 850 °C) to yield glass-ceramics with M_s of 8.26 emu/g. This shows that the magnetic bioglass-ceramics containing zinc ferrite are better suited for biomedical applicatiion requiring a bioacompatible magnetic material.

- The fourth chapter showed modified sol-gel route to prepare bioglass 45S5 and a magnetic variant of it with 2 wt % Fe_2O_3. This work gave us an opportunity to understand the tailor the sol-gel process to produce fully amorphous 45S5 and magnetic bioglass. These sol-gel variants offer new opportunities for bioglass in biomedical applications due to their superior bioactivity and physical properties.
- The work on PVA-PVP blends presented in chapter 5 opens up the possibility of using electrospinning to develop cost effective interactive wound dressings. Though only polymer blends were prepared and tested for this application, it is not difficult to functionalize these nanofibrous membranes with other beneficial additives to extend the application and functionality of these dressing materials. The composite membranes of PVA-BG and PVA-MBG show that the flexibility and biocompatible nature of PVA can be extended to osteoconductive

TH-1620_10612107

applications by preparing composites with BG and MBG. The combined use of sol-gel technique permits fabrication of composite fibers of PVA containing these osteoconducting and magnetic fillers. The presence of these fillers as blended composites and not as embedded nanoparticles makes them work as monolithic scaffolds for bone regeneration.

6.2 Scope for future work

The current thesis work has provided the groundwork on some new concepts, design, and potential applications of biomaterials based on magnetic glass-ceramics, nanoporous bioglass/glass-ceramics and nanofibrous polymeric composites. Though several new problems of interest were visible, they could not be pursued due to paucity of time. We are confident that these new pathways would be explored by the eager and enthusiastic scientific community soon. The following are some aspects related to this thesis work are worth exploring:

- Having found the recipe to synthesize bioglass 45S5 in sol-gel form, it is natural to prepare its variants by adding other additive to improve the functionality of the bioglass.
- Sol-gel magnetic bioglass synthesized of immense scientific interest. However, to realize its potential as thermo-seed, the amount of magnetic phase in it has to be increased. Since bioglass-ceramics can also serve as thermos-seeds, zinc ferrite containing sol-gel bioglass-ceramics would be practical interest.
- Though SBF based in vitro test have been shown to mimic in vivo results, these new and prospective bioglasses and bioglass-ceramics have to be tested in vivo in animal models to validate their potential for the suggested applications.

- The biodegradation mechanism of the composite scaffolds in SBF and the effects of degradation products during short and long term culture studies still remain to be understood. Since water uptake, biodegradation and HA layer formation occur at different stages of immersion, a careful investigation is required to understand these influence on the scaffolds. Such investigations could throw light on the complex mechanisms involved and help in improving the design and performance of composite scaffolds further.
- This study was based on biodegradable and hydrophilic polymers: The hydrophobicity of polymers has always been a cause of concern to dissolve them in a sol-gel solution. In most cases, it tends to separate from the sol-gel solution, this limiting their application significantly. Although a progress was made to address this issue in the current study, it would also be useful to explore the possibility of incorporating hydrophobic biodegradable polymers that can easily dissolve in a sol-gel solution.

References

[ABOU09a] E. Abou, A. Neel, D.M. Pickup, S.P. Valappil, R.J. Newport, J. C. Knowles., J Mater Chem. **19**, 690 (2009).

[ADAM13a] A. L. Adams, E. R. Essien, R. O Shaibu, A. Oki, New Journal of Glass and Ceramics. **2013**, 11 (2013).

[AINA09a] V. Aina, G. Malavasi, A. Fiorio Pla, L. Munaron, C. Morterra, Acta Biomater. **5**, 1211 (2009).

[AJAY07a] A. K.Gupta, R. R Naregalkar, V. D.Vaidya, M. Gupta, Nanomedicine. **2**, 23 (2007).

[AKSR12a] A.K. Srivastava, R. Pyare, S. P. Singh, Inter. J. Sci. & Eng. **3**, 1 (2012).

[ALEX11a] A. Hoppe, N. S. Güldal, A. R. Boccaccini, Biomater. **32**, 2757 (2011).

[ALHO12a] S. N. Alhosseini, F. Moztarzadeh M. Mozafari, S. Asgari, M. Dodel, A., Kargozar S. Samadikuchaksaraei, N. Jalali, Int. J. Nanomed. **7**, 25 (2012).

[AOKI04a] A. Oki, B. Parveen, S. Hossain, S. Adeniji, H. Donahue, J. Biomed. Mater. Res. A **69**, 216 (2004).

[ARDE97a] I. Ardelean, M. Peteanu, S. Flip, V. Simon and G. Gyorffy, Solid State Commun. **102**, 341 (1997).

[AYTI14a] A. Aytimur, Uslu I. Polym. Plast. Technol. Eng. **53**, 655 (2014).

[BALA07a] A. Balamurugan, G. Balossier, S. Kannan, J. Michel, A. H. S. Rebelo and J. M. F. Ferreira, Acta Biomater. **3**, 255 (2007).

[BALA08a] A. Balamurugan, G. Balossier, D. Laurent-Maquin, S. Pina, A.H.S. Rebelo, J. Faure, J.M.F. Ferreira, Dental Mater. **24**, 1343 (2008).

[BDCU01a] B. D. Cullity, S. R. Stock (2001), “*Elements of X-ray Diffractions*”, 3rd ed., Prentice, Hall.

[BELL02a] M. Bellantone, H.D Williams, L.L. Hench, Antimicrob. Agents Chemother. **46**, 1940 (2002),

[BERT02a B. Hildebrandt, P.Wust, O.Ahlers, A. Dieing, G. Sreenivasa, T. Kerner, R. Felix , H. Riess, Critical Reviews in Oncology/Hematology **43**, 33 (2002).

[BETT15a] S. Bettini, V. Bonfrate, Z. Syrgiannis, A. Sannino, L. Salvatore, M. Madaghiele, L. Valli, G. Giancane, Biomacromolecules **16**, 2599 (2015).

[BHAT14a] P. Bhattacharjee, B. Kundu, D. Naskar, T. K. Maiti, D. Bhattacharya, Kundu S. C., Biopolymers **103**, 271 (2014).

[BHUM11a] S. Bhumiratana, W. L. Grayson, A. Castaneda, D. N. Rockwood, E. S. Gil , D. L. Kaplan, G. Vunjak-Novakovic, Biomater **32**, 2812 (2011).

[BOCC05a] A.R. Boccaccini, J. J Blaker, V. Maquet, R.M. Day, R. Jérôme, Mater. Sci. Eng.C **25**, 23 (2005).

[BREK98a] J.H. Brekke, J.M. Toth. J. Biomed Mater Res **43**, 380 (1998).

[BRET05a] O. Bretcanu, S. Spriano, E. Verne, M. Coisson, P. Tiberto, P. Allia, Acta

Biomater. **1**, 421 (2005).

[BRET06a] O. Bretcanu, E. Verne, M. Coisson, P. Tiberto and P. Allia, J. Mag. Mag. Mater. **300**, 412 (2006).

[BRET06b] O. Bretcanu, S. Spriano, C. B. Vitale and E. Verne, J. Mater. Sci. **41**, 1029 (2006).

[BRET09a] O. Bretcanu, X. Chatzistavrou, K. Paraskevopoulos, R. Conradt, I. Thompson, A. Boccaccini, J. Eur. Ceram. Soc. **29**, 3299 (2009).

[BRUN06a] T. J. Brunner, R.N. Grass, W.J. Stark. Chem. Comm. **13**, 1384 (2006).

[BSMI99a] B. Smith (1999), "*Infrared Spectral Interpretation: A Systematic Approach*", CRC Press.

[BSUN14a] B. Sun, Y.Z. Long, H.D. Zhang, Prog. Polym. Sci. **39**, 862 (2014).

[BUCH02a] R.W. Bucholz. Clin Orthop Relat Res., **395**, 44 (2002).

[BURG00a] K. J. Burg, S. Porter, J.F. Kellam. **21**, 2347 (2000).

[CAPL99a] A.I. Caplan, Goldberg VM. Clin. Orthop. Relat. Res.,12-6 (1999).

[CAST04a] T. Castner Jr., G. S. Newell, W. C. Holtan, C. P. Slichter, J. Chem. Phys. **32**, 668 (2004).

[CATT13a] R. Catteaux, I. G. L., F. Désanglois, F. Chai, J.C. Hornez, S. Hampshire, C. F. Houttemane, Chem. Eng. Res. Des. **91**, 2420 (2013).

[CBRI90a] C. Brinker, G. Scherer (1990), "*Sol-gel science: the physics and chemistry of sol-gel processing*", 1st ed., Academic Press.

[CHEN06a] Q.Z. Chen, I.D. Thompson, A.R. Boccaccini, Biomater **27**, 2414 (2006).

[CHEN10a] Q.Z. Chen, Li, Y., Jin, L.Y., Quinn, J. M. W., Komesaroff, P., Acta Biomater. **6**, 4143 (2010).

[CJSE04a] C.J. Serna, M.P. Morales, Surf. Coll. Sci. **17**, 27 (2004).

[CLAR08a] B. Clarke, Clin J Am Soc Nephrol **3**, 131 (2008).

[CMHU82a] C.M. Hurd, Contemp. Phys. **23**, 469 (1982).

[COST12a] H. S. Costa, Mansur A.A., M. Pereira M.M. and H.S., J. Nanomater. **2012**, 718470 (2012).

[COST97a] A. Costantini, R. Fresa, A. Buri, F. Branda, Biomater. **18**, 453 (1997).

[DANI08a] D.l S Kohane, R. Langer, Pediatric Res. **63**, 487 (2008)

[DARC03a] D. Arcos, D.C. Greenspan, M. Vallet-Regí, J. Biomed. Mater. Res. A. **65**, 344 (2003).

[DAVI07a] D. J. Hak, J Am Acad Orthop Surg **15**, 525 (2007).

[DCCL03a] D. C. Clupper ,L. L. Hench, J. Non. Cryst. Solids. **318**, 43 (2003).

[DONN10a] O'Donnell, M.D. Hill, R.G., Acta Biomater. **6**, 2382 (2010).

[DRUS86a] G.L. Drusano, H.C. Standiford, K. Plaisance Antimicrob. Agents Chemother. **30**, 444 (1986).

[DWMO75a] D.W. Moon, J. M. Aitken, R. K. MacCrone, G. S. Cieloszyk, Phys. Chem. Glasses **16**, 91 (1975).

[EDZA92a] E.D. Zanotto, J. Non. Cryst. Solids, **147** & **148**, 820 (1992).

[EINH99a] T.A. Einhorn, Clin Orthop Relat Res. S59-67 (1999).

[EJLE10a] E.J. Lee, S.H. Teng, T.S. Jang, P. Wang, S.W. Yook, H.E. Kim, Acta Biomater **6**, 3557 (2010).

[ENNI12a] W.J. Ennis, Adv. wound care**.** **1**, 184 (2012).

[EROL13a] M. Erol-Taygun, K. Zheng, A.R. Boccaccini, Inter. J. Appl. Glass Sci. **4**, 136 (2013)

[ESSA14a] M. Es-saheb, A. Elzatahry, Inter. J. Polymer Sci. 2014;2014

[ESSI13a] E. R. Essien, L. A. Adams, R. O. Shaibu ,A. Oki, Biomed Sci Eng. **6**, 258 (2013).

[ESWA64a] E. S. Watson, M. J. O'Neil, J. Justin and N. Brener, Anal. Chem. **36**, 1233 (1964).

[ETIN07a] E. Duguet , S. Vasseur , S. Mornet , J.M. Devoisselle, Nanomedicine **1**, 157 (2007).

[FONE59a] S. Foner, Rev. Sci. Inst. **30**, 548 (1959).

[FOOL13a] A. Fooladi, A., Hosseini, H. M., Hafezi, F., Hosseinnejad, F., Nourani, M. R., J. Biomed. Mater. Res. A **101**, 1582 (2013).

[FRAC11a] A. Fraczyk, Tech. Sciences **14**, 93 (2011).

[GENT10a] E. Gentleman, Y.C. Fredholm, G.Jell, N. Lotfibakhshaiesh, M. D. O'Donnell, R.G. Hill, M.M. Stevens, Biomater **31**, 3949 (2010).

[GENU14a] F. Genuzio, A. Sala, T. Schmidt, D. Menzel, H-J. Freund, J. Phys. Chem. C **118** 29068 (2014).

[GKWI52a] G. K. Williamson, W. Hall, Acta Mater. **1**, 22 (1953).

[GORR09a] M.F. Gorriti, J.M. López, A.R. Boccaccini, C. Audisio, A.A. Gorustovich, Adv. Eng. Mater. **11**, B67 (2009).

[GORT50a] E. Gorter, Nature **165**, 798 (1950)

[GORU10a] A.A. Gorustovich, J.A. Roether, A.R. Boccaccini, Tissue Eng. Part B Rev. **16**, 199 (2010).

[HAIMI09a] S. Haimi, G. Gorianc, L. Moimas, B. Lindroos, Huhtala, H.; Räty, S.; Kuokkanen, H.; Sándor, G.K.; Schmid, C.; Miettinen, S.; Suuronen, R., Acta Biomater. **5**, 3122 (2009).

.[HAMI13a] P. Hamidreza, J. A. Nychka, J. Am. Ceram. Soc. **96**, 1643 (2013).

[HARR02a] L.G. Harris, S.J. Foster, R.G. Richards, Review. Eur. Cells Mater. **4**, 39 (2002).

[HENC05a] L.L. Hench, J. R. Jones (2005), "*Biomaterials artificial organs and tissue engineering*", Woodhead Publishing.

[HENC06a] L.L. Hench, The story of Bioglass®, J Mater Sci: Mater Med **17**, 967 (2006).

[HENC13a] L.L. Hench, New J Glass Ceram. **3**, 67 (2013).

[HENC72a] L.L. Hench, A. E. Clark.,H. F. Schaake, Int. J. Non-Cryst. Sol., **837**, 8 (1972).

[HENC82a] L.L.Hench, E.C. Ethridge. In: Biomaterials: An Interfacial Approach, Academic Press, New York (1982).

[HENC82b] L.L. Hench, and A. E. Clark,(1982) "*Biocompatibility of Orthopaedic Implants*", CRC Press, Florida.

[HENC91a] L.L. Hench, J. Am. Ceram. Soc. **74**, 1487 (1991).

[HENC98a] L.L. Hench, T. Kokubo (1998), "*Handbook of Biomaterial properties*", Chapman & Hall, London.

[HENC98b] L.L. Hench, J. Am. Ceram. Soc. **81**, 1705 (1998).

[HOLA85a] W. Holand, W. Vogel, K. Naumann and J. Gummel, J. Biomed. Mater. Res. **19**, 303 (1985).

[HSIC07a] C.S. Hsi, H.Z. Cheng, H.J. Hsu, Y.S. Chen, M.C. Wang, J. Eur. Ceram. Soc. **27**, 3171 (2007).

[HUAN03a] Z.M. Huang, Y.Z. Zhang, M. Kotaki Compos. Sci. Technol. **63**, 2223 (2003).

[HUMJ12a] J. Hum, A.R. Boccaccini, J Mater Sci Mater Med. **23**, 2317 (2012).

[HUTM00a] Hutmacher D.W. Biomater. **21**, 2529 (2000).

[IAVE15a] I. A. Vedernikova, Rev. J. of Chem. **5**, 256 (2015).

[IKED86a] T. Ikeda, H. Hirayama, H. Yamaguchi, M. Watanabe, Antimicrob. Agents Chemother. **30**, 132 (1986).

[ITOK93a] M. Itokazu, T. Matsunaga, Arthroscopy: The Journal of Arthroscopic & Related Surgery **9**, 103 (1993).

[JAYA10a] R. Jayakumar Menon D., Manzoor K., Nair S.V., Tamura H., Carbohyd Polym. **82**, 227 (2010).

[ACJA13a] A.C. Jayalekshmi, S.P. Victor, C.P. Sharma, Colloids Surf B Biointerfaces **101**, 196 (2013).

[JEON07a] J.S. Jeong, J.S. Moon, S.Y. Jeon, Thin Solid Films. **515**, 5136 (2007).

[JEYA94a] B. Jeyadevan, K. Tohji, K. Nakatsuka, J. Appl. Phys. **76,** 6325 (1994).

[JMAS12a] J. Massera, S. Fagerlund, L. Hupa, Mikko Hupa, J. Am. Ceram. Soc. **95**, 607 (2012)

[JONA03a] J. C. Knowles, J. Mat. Chem. **13**, 2395 (2003).

[JULI13a] J.R. Jones, Acta Biomater., **9**, 4457 (2013).

[JUNG11a] S.B. Jung, D.E. Day, T. Day, W. Stoecker, P. Taylor, Wound Repair Regen **19**, 30 (2011).

[KAMO14a] Kamoun E. A., Chen X., Mohy Eldin M.S., Arab. J. Chem. **8**, 1 (2014).

[KANE04a] H. Kaneko, T. Kodama, N. Gokon, Y. Tamaura, K. Lovegrove and A. Luzzi, Sol Energy **76**, 317 (2004).

[KAWA04a] M. Kawashita, Y. Iwahashi, T. Kokubo, T. Yao, S. Hamada, T. Shinjo, J. Ceram. Soc. Jpn., **112**, 373 (2004).

[KAWA05a] M. Kawashita, M. Tanaka, T. Kokubo, Y. Inoue, T. Yao, S. Hamada, T. Shinjo, Biomater. **26**,2231 (2005).

[KAWA08a] M. Kawashita, S. Domi, Y. Saito, M. Aoki, Y. Ebisawa, T. Kokubo, T. Saito, M. Takano, N. Araki and M. Hiraoka, J. Mater. Sci., Mater. Med. **19** ,1897 (2008).

[KEAS98a] D.H. Keast, H. Orsted, Ostomy. Wound. Manage. **44**, 30 (1998;).

[KIMH06a] H.W. Kim, H.H. Lee, J.C. Knowles, J Biomed Mater Res A. **79**, 643 (2006).

[KIMH06a] H.W. Kim, Kim H.E., J. C. Knowles, Adv. Funct. Mater. **16** , 1529 (2006).

[KING06a] H. King Lam, Biocompatibility of degradable materials, Ph.D. thesis.

[KOKU06a] T. Kokubo, T. Hiroaki, Biomater. **27**, 2907 (2006).

[KOKU91a] T. Kokubo, Biomater., **12**, 155 (1991).

[KOMA08a] T. Komatsu, N. Soga, J. Chem. Phys. **72**, 1781 (2008).

[KUHN98a] J. Y Rho J. Y, Kuhn-Spearing L, Zioupos P., Med Eng Phys **20**, 92 (1998).

[LACO89a] M. Lacovacci, E.C. da Silva, H. Vargas, E.A. Pinheiro, F. Galembeck, L.C.M. Miranda, J. Appl. Phys. **65**, 5150 (1989).

[LAKH13a] N.J. Lakhkar, I.H. Lee, H.W. Kim, V. Salih, I.B. Wall, J.C. Knowles, Adv. Drug Deliv. Rev. **65** , 405 (2013).

[LAKS32a] L. S. Naira, Cato T. Laurencina, Prog. in Pol.r Sci. **32**, 762 (2007).

[LAUR02a] Laurencin C.T., Lu H.H., Khan Y. (2002), "*Methods of Tissue Engineering", California*, Academic Press.

[LEND11a] A. Lendlein, Sisson A. (2011), "*Handbook of biodegradable Polymer: Synthesis, Characterization and Applications*", (Wiley-VCH Verlag & Co Germany).

[LENZ02a] F. S. Lenza, L. W. Vasconcelos, Mat. Res. **5**, 497 (2002).

[LIMW13a] Li M., Y. Wang, Q. Liu, Qi. Li, Ya. Cheng, Yu. Zheng, T. Xi, S. Wei, J. Mater. Chem. B **1**, 475 (2013).

[LING12a] Li Lingli, G. Li, J. Jiang, X. Liu, L. Luo, K. Nan, J Mater Sci Mater Med **23**, 547 (2012).

[LIUX09a] X. Liu, W. Huang, H. Fu, A. Yao, D. Wang, H. Pan, W. Lu, J. Mater. Sci. Mater. Med. **20**, 365 (2009).

[LUCA11a] A. L.Girot, J. Non. Cryst. Solids **357**, 3322 (2011).

[LUTZ10a] L.C. Gerhardt, A. R. Boccaccini, Mater. **3**, 3867 (2010).

[MAND09a] B.B. Mandal, S.C Kundu., Biomater. **30**, 2956 (2009).

[MAND09b] B.B. Mandal, S.C Kundu., Acta Biomater., **5**, 2579 (2009).

[MAND12a] B.B. Mandal, Grinberg A., Gil E.S., Panilaitis B., Kaplan D.L., Proc. National Academy of Sciences, **109**, 7699 (2012).

[MART06a] M. Cerruti, Nita Sahai, Rev. Mineral. Geochem. **64**, 283 (2006).

[MICH07a] Michel Vert, Prog. Pol. Sci. **32**, 755 (2007).

[MILE11a] C. A. Milea, C. Bogatu, Bull. Transilv. Univ. Brasov Eng. Sci. **4**, 59 (2011).

[MNOF90a] M. Nofz, R. Stosser, F.G. Wihsmann, Phys. Chem. Glasses **31**, 57 (1990).

[MNRA11a] M. N. Rahaman, D. E. Day, B. S. Bal, Q. Fu, S. B. Jung, L. F. Bonewald, A. P. Tomsia, Acta Biomater., **7**, 2355 (2011).

[MURU15a] S. Murugesan S., N.M. Sundaram, Inter J Nanomed, **10**, 99 (2015).

[MZHU12a] M. Zhu, J. Shi, Q. He, L. Zhang, F. Chen, Chen, Y., J. Mater. Sci., **47**, 2256 (2012).

[NAIR06a] L. S. Nair, C. T. Laurencin, Adv. Biochem. Eng. Biotechnol **102**, 47 (2006).

[NAND10a] A. Nandakumar, H. Fernandes, J. de Boer, L. Moroni, P. Habibovic, C.A. van Blitterswijk, Macromol Biosci **10**, 1365 (2010).

[BHAR10a] N. Bhardwaj, S.C Kundu., Biotechnol. Adv. **28**, 325 (2010).

[NEZA12a] N. Nezafati, F. Moztarzadeh, S. Hesaraki, Biotechnol Bioprocess Eng, **17**, 746 (2012).

[NIEH09a] H. Nie, M-L. Ho, C-K. Wang, C-H Wang, Fu Y-C., Biomater., **30**, 892 (2009).

[NOHS12a] S. Noh, W. Na, J. Jang, J. Lee, E. Lee, S. Moon, Y. Lim, J. Shin and Jinwoo Cheon, Nano Lett. **12**, 3716 (2012).

[NORM94a] M. E. Norman, H. M. Elgendy, E. C. Shors, S.F. el-Amin, C.T. Laurencin, Clin. Mater, **17**, 85 (1994).

[NRAJE13a] N. Rajeswari, S.Selvasekarapandian, S. Karthikeyan, Ionics. **19**, 1105 (2013).

[OHAN91a] O. H. Andersson, K. H. Karlsson, J. Non. Cryst. Solids **129**, 145 (1991).

[OHTS91a] C. Ohtsuki, H Kushitani, T Kokubo, S Kotani, Yamamuro T., J Biomed Mater Res. **25**, 1363 (1991).

[OHTS92a] C. Ohtsuki, T. Kokubo, T. Yamamuro, J. Non-Cryst. Solids,**143**, 84 (1992).

[OHUR04a] K. Ohura, M. Ikenaga, T. Nakamura, T. Yamamuro, Y. Ebisawa, T. Kokubo, Y. Kotoura, M. Oka, J. Appl. Biomater., **2**, 153 (2004).

[OSCA12a] O. Peitl, E.D. Zanotto, F. C. Serbena, L. L. Hench, An Introduction to Bioceramics 2nd Edition, 2012

[OTAD15a] M. Otadia, D. Mohebbi-Kalhori, Procedia Mater. Sci. **11**, 196 (2015).

[PADI05a] S. Padill, J.Román, A.Carenas, M.Vallet-Regí, Biomater **26**, 475 (2005).

[PALM08a] L. C. Palmer, C. J. Newcomb, S.R. Kaltz, E.D. Spoerke, S.I. Stupp, Chem. Rev., **108**, 4754 (2008).

[PEHK00a] K. Peh, T. Khan, H. Ch'ng, J. Pharm. Pharm. Sci. **3**, 303 (2000).

[PERE10a] M.S. Peresin, Y. Habibi, A. Vesterinen, Nanocrystals. **11**, 2471 (2010).

[POUR14a] S. Pourhashem, A. Afshar, Ceram. Int. **40**, 993 (2014).

[PRAB09a] M. Prabhakaran,J. Venugopal, S. Ramakrishna, Acta Biomater **5**, 2884 (2009).

[QIUH15a] Q. Yang, M. Gong, S.Cai, T. Zhang, J. T. Douglas, V. Chikan, N.l M. Davies, P. Lee, I.Y. Choi, S.Ren, M. L. Forrest. Ther Deliv. doi:10.4155/tde.15.68, (2015).

[QUIN09a] F. Quintero, J. Pou, R. Comesaña, LusquiñosAz, F., Riveiro, A., Mann, A. B., Hill, G. H., Wu Z. Y., and Jones, J. R, Adv. Funct. Mater, **19**, 3084 (2009).

[RAHP13a] S. Rahpeyma, M. H. Fathi, K. R. Ebrhimi, A. Doustmohannadi,. J. New Mater., **3**, 93 (2013).

[RAMA05a] S. Ramakrishna, K. Fujihara, W.E Teo, (2005) *An Introduction to Electrospinning and Nanofibers*,World Scientific Pub. Singapore.

[RAMI02a] A. Rámila, F. Balas, M. Vallet-Regí, Chem. Mater. **14**, 542 (2002).

[RAO95a] A.S. Rao, R.R. Reddy, T.V.R. Rao, J.L. Rao, Solid State Commun. **96**, 701 (1995).

[RAWL92a] R. D. Rawlings, J Mater Sci Letters **11**, 1340 (1992).

[RDCU72a] R. D. Cullity, *Introduction to Magnetic Materials*. (Addison-Wesley, 1972).

[REZW06a] K. Rezwan, Q. Z. Chen, J. J. Blaker, A.R. Boccaccini. Biomater **27**, 3413 (2006).

[RKSI08a] R. K. Singh, G. P. Kothiyal, A. Srinivasan, J. Non-Cryst. Solids **354**, 3166 (2008).

[RKSI08b] R. K. Singh, G. P. Kothiyal, A. Srinivasan, Solid State Commun. **146**, 25 (2008).

[RKSI08c] R. K. Singh, G.P. Kothiyal, A. Srinivasan, J. Magn. Magn. Mater **320**, 1352 (2008).

[RKSI09a] R. K. Singh, *Investigations on selected bioactive glasses and glass ceramics containing iron oxide*, Ph.D. thesis, Indian Institute of Technology Guwahati, India (2009).

[RKSI10a] R. K. Singh, A. Srinivasan, Mater. Sci. Eng. C. **30**, 1100 (2010).

[RKSI11a] R. K. Singh, A. Srinivasan, Magn. Magn. Mater., **323**, 330 (2011).

[RKSI14a] R. K. Singh, K.D. Patel, J-H. Lee, E-J. Lee, J-H Kim, T-H Kim, H.W. Kim, PLoS One. **9**, 1 (2014).

[ROMA13a] A. Román, A. Pére, J-E. Won, J.C. Knowles, H.W. Kim, Advanced Drug Delivery Reviews **65**, 471 (2013).

[RWJO89a] R. W. Jones, (1989) *Fundamental Principles of Sol-Gel Technology*, (The Institute of Metals, London).

[SALG04a] Salgado AJ, Coutinho OP, Reis RL. Macromol. Biosci. **4**, 743 (2004).

[SEAL01a] B.L Seala, T.C Oterob, A Panitcha, Materials Science and Engineering: R: Reports, **34**, 147 (2001).

[SEEM08a] S. Agarwal, J.H. Wendorff, A. Greiner. Polymer. **49**, 5603 (2008).

[SERE15a] M. Serena, V. Greco, F. Baldassarre, D. Vergara, M. Maffia, S. Leporatti, Macromol. Biosci. **15**, 1365 (2015).

[SHAH15a] S. Sharifi, H.Seyednejad, S. Laurent, F. Atyabi, A.A. Saei, M. Mahmoudi, Contrast Media Mol Imaging, **10**, 329 (2015)

[SHEL97a] J. E. Shelby, (1997) Introduction to Glass Science and Technology, (The Royal Society of Chemistry, Cambridge, UK).

[SING99a] K. Singh, D. Bahadur, J. Mater. Sci., Mater. Med. **10**, 481 (1999).

[SIQU11a] R. L. Siqueira, O. Peitl, E. D Zanotto, Mater. Sci. Eng. C **31**, 983 (2011).

[SIQU13a] R. L. Siqueira, E. D. Zanotto, J. Mater. Sci. Mater. Med. **24**, 365 (2013).

[SKYO02a] S. K. Young, Overview of Sol-Gel Science and Technology, Army research laboratory, 2002.

[SOGO05a] Y. Sogo, A. Ito, K. Fukasawa, T. Sakurai, N. Ichinose, R.Z. LeGeros, Key Eng. Mater. **284**, 31 (2005).

[SRIN12a] S. Srinivasan, R. Jayasree, K.P. Chennazhi, S.V. Nair, R. Jayakumar, Carbohyd Polym **87**, 274 (2012).

[STLI59a] S.T. Lin, Phys. Rev. **116**, 1447 (1959).

[SUCH06a] L. Suchanek, L. Wojciech, Riman, E. Richard, Advances in Science and

TH-1620_10612107

Technology, **45**, 184 (2006).

[SUJA12a] S. Sarabahi, Indian J Plast Surg. **45**, 379 (2012).

[SUNT13a] S. Mahalingam, M. Edirisinghe, Macromol. Rapid Commun. **34**, 1134 (2013).

[TEJA09a] A. S. Teja, P-Y. Koh, Prog. Cryst. Growth Charact. Mater. **55**, 22 (2009).

[TETT14a] G. Tetteh, A.S. Khan, R.M. Smith, G.C. Reillyn, I.U. Rehman, J Mech Behav Biomed Mater, **39**, 95 (2014).

[THEI08a] W. W. Thein-Han, Y. Kitiyanant, R.D.K. Misra. Mater Sci Tech **24**, 1062 (2008).

[THEI09a] W.W. Thein-Han, R.D.K. Misra. Acta Biomater **5**, 1182 (2009)

[UMAS14a] U. M. Subramanian, S.V. Kumar, N. Nagiah, Int. J. Polym. Mater. **63**, 476 (2014).

[VITA08a] C. Vitale-Brovarone, M. Miola, C. Balagna, E. Verné, Chem. Eng. J., **137**, 129 (2006)

[WEB_PURE] https://www.purdue.edu/ehps/rem/rs/sem.html

[WEB_RTIN] http://www.rtinstruments.com/products/new-instruments/hitachi-high-tech- sciences-sta7200-simultaneous-thermal-analyzer/

[WEB_SCIE] http://sciencehelp.blog.com/2013/01/21/electron-microscope

[WEB_SEER] http://training.seer.cancer.gov/ anatomy/skeletal/tissue.html

[WILL86a] D.F. Williams (1986), *Proc. Consensus Conference of the European Society for Biomaterials*, Elsevier, New York.

[WOOL03a] A.D. Woolf, B. Pfleger, Bull. World Health Organization 8**1**, 646 (2003).

[WUMW13a] Wu M., Wang Q., Liu X., Liu H., Carbon **51**, 335 (2013).

[WEB_INGa] http://www.ing.unitn.it/~luttero/laboratoriomateriali/RietveldRefinement

[XMLI10a] X.M. Liu, J. Shaw, J. Z. Jiang, J. Bloemendal, P. Hesse, R. Tim, X. G. Mao, Sci China Earth Sci. **53**, 1153 (2010).

[YANG01a] S. Yang, K.F. Leong, Z. Du, C.K. Chua, Tissue Eng. **7**, 679 (2001).

[YANG12a] X. Yang, L. Zhang, X. Chen, X. Sun, Yang, G., Guo, X., Yang, H., Gao, C. and Gou, Z., J. Non-Crystalline Solids **358**, 1171 (2012).

[YEBI90a] Y. Ebisawa T. Kokubo, J. Mater. Sci -Mater. Med. **1**, 239 (1990).

[YEBI92a] Y. Ebisawa, T. Kokubo, J. Mater. Sci -Mater. Med. **41**, 225 (1992).

[YEBI97a] Y. Ebisawa, F. Miyaji, T. Kokubo, K. Ohura, T. Nakamura, Biomater., **18**, 1277 (1997).

[YOLA15a] Y.Piñeiro, Z. Vargas, José Rivas, Manuel Arturo López-Quintela., Eur. J. Inorg. Chem. **10,** 4495 (2015).

[ZAMA11a] H.U. Zaman, J.M.M Islam, M. A. Khan, J. Mech. Behav. Biomed. Mater. **4**, 1369 (2011).

[SIQI15a] S. Siqi, K.B. Zhang, S.K. Taktak, VanOosten, Macromol. Rapid Commun. **36**, 1322 (2015).

Publications/communications originating from the thesis work:

In journals:

1. **Nisha Shankhwar**, R. K. Singh, G. P. Kothiyal, A. Perumal and A. Srinivasan, "Evolution of magnetic properties of CaO-P_2O_5-$Na_2OFe_2O_3$-SiO_2 glass upon heat treatment", *IEEE Trans. Magn.* **50**, 4003504 (2013), doi:10.1109/TMAG.2013.2278570.
2. **Nisha Shankhwar**, G. P. Kothiyal and A. Srinivasan, "Understanding the magnetic behaviour of heat treated CaO-P_2O_5-$Na_2OFe_2O_3$-SiO_2 bioactive glass using electron paramagnetic resonance studies", *Physica B* **448**, 132 (2014), doi:10.1016/j.physb.2014.03.070.
3. **Nisha Shankhwar**, Manishekhar Kumar, Biman B. Mandal, P. S. Robi and A. Srinivasan, "Electrospun polyvinyl alcohol-polyvinyl pyrrolidone nanofibrous membranes for interactive wound dressing application", *J. Biomater. Sci. Polym. Ed.* **27**, 247 (2015), doi.org/10.1080/09205063.2015.1120474.
4. **Nisha Shankhwar**, G. P. Kothiyal and A. Srinivasan, "Influence of phosphate precursor on the structure, crystallization behaviour and bioactivity of sol-gel derived 45S5 bioglass", *RSC Adv.*, **5**, 100762 (2015), doi.10.1039/C5RA19184J.
5. **Nisha Shankhwar** and A. Srinivasan, "Evaluation of sol–gel based magnetic 45S5 bioglass and bioglass-ceramics containing iron oxide", *Mater. Sci. Eng. C.* **62**, 190 (2016), doi:10.1016/j.msec.2016.01.054.
6. **Nisha Shankhwar**, Rajendra K. Singh and A. Srinivasan, "Evolution of magnetic and bone mineral phases in heat treated bioactive glass containing zinc and iron oxides", *Applied Glass Sci., 1–12 (2016)* doi:10.1111/ijag.1219.
7. **Nisha Shankhwar**, Manishekhar Kumar, Biman B. Mandal and A. Srinivasan, "Novel polyvinyl alcohol-bioglass 45S5 based composite nanofibrous membranes as bone scaffolds", *Intern. J. Polymeric. Mater. Polymeric. Biomater.* *(communicated)*.

In conferences/symposia:

1. **Nisha Shankhwar**, G.P. Kothiyal and A. Srinivasan, "Synthesis and characterization of gel-derived bioactive ceramic-polymer nanocomposites", *Proc. Cond. Mater. Days* (2012), Ranchi.

2. **Nisha Shankhwar**, G. P. Kothiyal, A. Srinivasan, "Sol-gel derived porous bioactive nanocomposites: Synthesis and *in vitro* bioactivity", *AIP Proc.* **1536** (2013) 209.
3. **Nisha Shankhwar**, R. Das, G. P. Kothiyal and A. Srinivasan, "Synthesis and characterization of electrospun bioactive polymer-hydroxyapapite composite fibers", *Proc. Intl. Conf. Mater. Sci.* (2013) Agartala.
4. **Nisha Shankhwar** and A. Srinivasan, "Electrospun poly (vinyl pyrrolidone)-polyvinyl alcohol nanofibers for biomedical applications", *Proc. First Symp. Adv. Sustainable Polymers* (2014) *Guwahati*.
5. **Nisha Shankhwar**, R. K. Singh and A. Srinivasan, "Preparation and characterization of silicate bioglass-ceramics containing zinc-ferrite", *Proc. Intl. Conf. Emer. Mater. Charact. & Appl.* (2014) *Kolkata*.
6. **Nisha Shankhwar** and A. Srinivasan, "Sol-gel derived magnetic bioglass and bioglass ceramic for hyperthermia application", *Proc. Intl. Conf. Asian Union Magn. Soc.* (2014) *Haikou*.
7. **Product demonstration** in *Make-in-India week* organized by Ministry of commerce & industry, India held in Mumbai during 13 Feb '16 to 18 Feb '16.

Book chapter:

Nisha Shankhwar, K. Sharma, G.P. Kothiyal and A. Srinivasan, "Bioactive glass & glass ceramics containing iron oxide: Preparation and properties"; *Trends in Biomaterials*, *Publishers: PanStanford Publishing Ltd., March 1, 2016;* **ISBN: 9789814613989**

Edited by - G. P. Kothiyal & A. Srinivasan

Publications outside of the thesis work:

1. Pawan Kumar, **Nisha Shankhwar**, A. Srinivasan and Manoranjan Kar, Oxygen Octahedra Distortion induced Structural and Magnetic Phase Transitions in $Bi_{1-x}Ca_xFe_{1-x}Mn_xO_3$ Ceramics, *J. Appl. Phys.* **117**, (2015), doi.org/10.1063/1.4921433.

2. Kibrom Alebel Gebru, **Nisha Shankhwar**, A. Srinivasan, C. Das, "Effect of electro-spinning duration on morphology of electrospun polyvinyl alcohol nanofiber membranes", *RSC Adv*, (*communicated*).

~*~*~*~*~*~*~*~*~*~*~*~*~